

Master of Science Thesis

PIV and force measurements on the flapping-wing MAV DeFly II

An aerodynamic and aeroelastic investigation
into vortex development

M.A. Groen

20 December 2010



PIV and force measurements on the flapping-wing MAV DeFly II

An aerodynamic and aeroelastic investigation
into vortex development

Master of Science Thesis

For obtaining the degree of Master of Science in Aerospace Engineering
at Delft University of Technology

M.A. Groen

December 20, 2010



Delft University of Technology

Copyright © Aerospace Engineering, Delft University of Technology
All rights reserved.

DELFT UNIVERSITY OF TECHNOLOGY
DEPARTMENT OF AERODYNAMICS

The undersigned hereby certify that they have read and recommend to the Faculty of Aerospace Engineering for acceptance the thesis entitled **“PIV and force measurements on the flapping-wing MAV DelFly II : An aerodynamic and aeroelastic investigation into vortex development”** by **M.A. Groen** in fulfillment of the requirements for the degree of **Master of Science**.

Dated: December 20, 2010

Examination Committee:

Prof. dr. ir. H. Bijl

Dr. ir. B.W. van Oudheusden

Dr. ir. J.F.L. Goosen

Ir. B.D.W. Remes

Preface

This report will mark the end of a six year period studying at the Aerospace Engineering faculty at Delft University of Technology. Looking back, these years have (sometimes literally) flown by. So this is the appropriate place to thank some people.

First I would like thank Bas van Oudheusden and Hester Bijl from the aerodynamics department and Bart Remes en Rick Ruijsink from the MAVlab for giving me the opportunity to graduate at this unconventional, but very interesting subject. With their support and supervision, I managed to make this thesis a success.

A special thanks goes out to Bart Bruggeman, my colleague during the research on DelFly. Together we built the set-up and he provided the wings that are subject of my thesis. Thank you for helping me repair those, sometimes frustratingly, tiny and fragile DelFly models.

I would like to thank the staff at the aerodynamics department, Prof. Scarano, Ferry, Joost en Roeland, for sharing their knowledge on PIV and their support during the experiments. Also a word of thanks for Eric, Frits, Nico and Peter, for their help with setting up the PIV system and giving technical support. And my fellow graduate students in the 'kelder' for making this graduation year, an enjoyable time.

I am grateful for my family and friends, both in Delft and in Hazerswoude for their support. Roy for our competitive friendship these six years and for reviewing this report. Finally a huge thanks to my parents for making this all possible.

Mark Groen
Delft, December 2010

Abstract

Recent years have seen an increasing interest in Micro Air Vehicles (MAVs). MAVs are small (micro sized) aircraft and find their application in a multitude of commercial, industrial and military purposes. To perform their missions MAVs should be small sized, have good manoeuvrability, be well controllable and have a broad flight envelope. When flying in small confinements, the ability to fly at low airspeed and to have good manoeuvrability is critical. One type of MAVs, the flapping-wing MAV, particularly has attractive characteristics for flight in confined spaces.

DelFly is a biplane flapping-wing MAV designed and built at Delft University of Technology. DelFly is able to hover and has an onboard camera for observation and vision-based control. For the DelFly project a top-down approach is followed, where from the study of a relative large model experience and theoretical insights can be gained, that can assist to create smaller, functional versions of the DelFly. The ultimate aim of the DelFly project is to improve the design to a very small full autonomous aircraft.

For the current experimental investigation, force and flow field measurements were performed on a hovering DelFly II, since this model has a broad flight envelope and proven flight performance. The flow field is studied using particle image velocimetry. Due to the flexible wings there is a strong fluid structure interaction, therefore also the in-flight wing deformation is determined. The aerodynamic mechanism generating forces on the DelFly are related to those found in insect flight. Since leading edge vortices (LEVs) in insect flight are identified as the most important unsteady aerodynamic mechanism enhancing lift generation for insects, the development of these for the DelFly are very interesting. The vortex development is studied for various wings, at various flapping frequencies and at various spanwise positions.

For the DelFly wing a conical LEV is developed, starting at out-board spanwise positions, approximately halfway during the translation. This LEV grows larger and is shed along the chord and at this time a new LEV starts to grow at the leading edge. This second LEV is dissipated at the end of the out-stroke during wing rotation, but at the end of the in-stroke this LEV moves above the wings and interacts with the counter-rotating LEV from the mirror wing. Inside the vortex tube a spanwise velocity component out-board is present. The shedding of the initial vortex and start of a second LEV is not completely consistent with LEV development for insect flight (which typically operate at a lower Reynolds number).

The vortex size and strength varies at different frequencies. The LEV strength (circulation) is decreased for higher flapping frequencies (while the trailing edge vortex (TEV) strength increases for higher flapping frequencies). An increase in LEV circulation at equal flapping frequency could also be seen for a high aspect ratio wing (33% increased AR), which has the

same stiffener orientation, but a reduced wing chord. This, therefore, is probably an effect of the decreased Reynolds number.

Another important aerodynamic mechanism increasing thrust generation for the DelFly, is the *clap-and-peel* mechanism, identified in previous research^[1]. From the recorded in-flight wing deformation it could be seen that during the start of the out-stroke the flexible biplane wings peel apart at the leading edge, while they clap together at the trailing edge. The peeling of the wings creates a down flow as well as a spanwise flow in-board and the clap of the wings creates a downward momentum jet. The down flow suppresses the LEV, while the generation of a TEV is postponed as long as the clap of the trailing edges is not completed.

A more power efficient wing, resulting from a wing geometry study performed by Bruggeman^[2], is compared with the original DelFly II wing. From the in-flight wing deformation it could be seen, that the more out-board placed stiffeners give the improved wing more rigidity at these positions during wing rotation. The flow field measurements show the original wing to have a larger LEV during the out-stroke. The improved wing shows a stronger down flow, decreasing LEV size, which might be due to the more rigid wing rotation. While the research of Bruggeman showed the improved wing to have the same thrust production as the original wing, the presented research showed a decrease in thrust, which could be due to various causes, like small variations in wing mounting, foil tension and/or deterioration of the driving mechanism. The cause of the consistently lower power consumption over the whole flap cycle remains unclear, however.

Table of Contents

Preface	v
Abstract	vii
Nomenclature	xiii
1 Introduction	1
1.1 Motivation.....	2
1.2 Thesis outline.....	3
2 Flapping wing aerodynamics	5
2.1 Introduction to flapping flight.....	5
2.1.1 Wing kinematics	6
2.1.2 Aerodynamic mechanisms	6
2.2 The Leading Edge Vortex.....	6
2.3 Rotational forces and the Kramer effect	8
2.4 Wing-wake interaction.....	9
2.5 Clap-and-fling.....	10
2.6 Wing flexibility effects in flapping flight	12
3 The flapping MAV DelFly	13
3.1 DelFly design.....	14
3.1.1 Similarity parameters	15
3.2 Flight kinematics	16
3.3 Research and development	17
3.3.1 Aerodynamics and aeroelasticity	17
3.3.2 Performance improvements	19

4 Particle Image Velocimetry	23
4.1 Basic principles.....	23
4.2 Stereoscopic PIV	26
5 Experimental set-up	29
5.1 Introduction to the experimental set-up	29
5.2 The experimental campaigns	31
5.3 Force measurements and DelFly control	34
5.4 PIV instrumentation.....	35
5.4.1 Seeding generator.....	35
5.4.2 Laser.....	35
5.4.3 Cameras	35
5.4.4 PTU.....	36
5.4.5 Software	36
5.5 PIV settings.....	36
5.5.1 Camera and laser settings.....	36
5.5.2 Image post processing.....	38
6 Results	41
6.1 Introduction.....	41
6.2 In-flight wing shape	42
6.3 Force measurements on the hovering DelFly	44
6.3.1 Average force generation	44
6.3.2 Force generation during one flap cycle.....	46
6.4 PIV measurements on the hovering DelFly	49
6.4.1 Flow field during one flap cycle	49
6.4.2 Flow field for clap-and-peel.....	52
6.4.3 Flow field for different wings	53
6.4.4 Effect of flapping frequency	56
6.4.5 Flow field for varying spanwise location.....	58
6.4.6 Spanwise flow	60
7 Conclusions and recommendations	63
7.1 Conclusions.....	63
7.1.1 Leading edge vortex development	63

7.1.2	Clap-and-peel mechanism.....	64
7.1.3	Wing comparison.....	64
7.2	Recommendations.....	65
Bibliography		67
A DelFly II specifications		71
B Vorticity and swirling strength calculations		73
B.1	Circulation of a vortex.....	75
C Swirling strength measurements		77
C.1	Improved wing at 9 Hz at $0.71R$	78
C.2	Improved wing at 11 Hz at $0.71R$	79
C.3	Improved wing at 11 Hz at $0.86R$	80
C.4	Improved wing at 13 Hz at $0.43R$	81
C.5	Improved wing at 13 Hz at $0.57R$	82
C.6	Improved wing at 13 Hz at $0.71R$	83
C.7	Improved wing at 13 Hz at $0.86R$	84
C.8	Original wing at 11 Hz at $0.86R$	85
C.9	High aspect ratio wing at 11 Hz at $0.71R$	86
C.10	High aspect ratio wing at 13 Hz at $0.71R$	87

Nomenclature

Latin symbol	Description	Units
<i>A</i>	wing stroke amplitude	m
<i>AR</i>	aspect ratio	-
<i>b</i>	span	m
<i>c</i>	chord	m
<i>d</i>	particle diameter, displacement	m, m
<i>dt</i>	pulse separation	s
<i>f</i>	flapping frequency	Hz
<i>f_#</i>	aperture number	-
<i>F</i>	force	N
<i>g</i>	gravitational acceleration	m s ⁻²
<i>J</i>	advance ratio	-
<i>m</i>	mass	g
<i>M</i>	magnification	-
<i>R</i>	semi wing span	m
<i>Re</i>	Reynolds number	-
<i>Ro</i>	Rossby number	-
<i>S</i>	semi wing area	m ²
<i>St</i>	Strouhal number	-
<i>t</i>	time	s
<i>T</i>	flapping period	s
<i>u, v, w</i>	velocity component in x,y,z-direction respectively	m s ⁻¹
<i>V</i>	velocity	m s ⁻¹
Greek symbol	Description	Units
<i>Γ</i>	circulation	m ² s ⁻¹
<i>θ</i>	camera angle	deg
<i>λ</i>	wave length, eigenvalue of the velocity gradient	m, s ⁻¹
<i>λ_{ci}</i>	swirling strength	s ⁻¹
<i>ν</i>	kinematic viscosity	m ² s ⁻¹
<i>ξ</i>	vorticity	s ⁻¹
<i>σ</i>	standard deviation (in force, velocity)	N, m s ⁻¹
<i>τ</i>	dimensionless time	-
<i>φ</i>	wing stroke angle	deg
<i>ψ</i>	dihedral	deg
<i>Ω</i>	angular velocity of a flapping wing	rad s ⁻¹

Subscript	Description
c	complex
diff	diffraction
eff	effective
i	imaginary
p	of particle
r	real
v	in vertical direction
x	in x-direction
y	in y-direction
z	in z-direction (spanwise direction)
∞	freestream condition

Abbreviations

CCD	Charge Coupled Device
DUT	Delft University of Technology
FFT	Fast Fourier Transform
IMAV	International Micro Air Vehicle conference and flight competition
LEV	Leading Edge Vortex
MAV	Micro Air Vehicle
PID	Proportional-Integral-Derivative
PIV	Particle Image Velocimetry
PTU	Programmable Timing Unit
TEV	Trailing Edge Vortex

Chapter 1

Introduction

Recent years have seen an increasing interest in Micro Air Vehicles (MAVs). MAVs are small (micro sized) aircraft and find their application in a multitude of commercial, industrial and military purposes, like observation and search and rescue missions. To perform these missions MAVs should be small sized, have good manoeuvrability, be well controllable and have a broad flight envelope. When flying in small confinements, like for example, a building struck by an earthquake in search of survivors, the ability to fly at low airspeed and to have good manoeuvrability is critical.

MAVs come in various types, like conventional fixed wing aircraft and rotary aircraft. A third type of MAV has attractive characteristics for flight in confined spaces; the flapping-wing MAV. Flapping-wing MAVs (ornithopters) may have the ability to hover like rotary aircraft, while they lack the high speed rotating blades that may be dangerous and are easily damaged. Flapping-wing MAVs, therefore, are an interesting research subject. These MAVs are different from conventional fixed wing aircraft as they use their flapping wings both for a means of propulsion (thrust) as for a means to sustain flight (lift). This poses high requirements on their wing design. Since flapping-wing MAVs are quite novel, much of the exact aerodynamics related to flapping wings and most efficient wing geometry is relatively still unknown. Nature, however, already provides excellent examples of small flapping-wing flyers: insects. Insects evolved their flapping wings in the course of millions of years, so it is logical to draw inspiration from them when developing flapping-wing MAVs.

In 2005 a student team at Delft University of Technology designed and built an MAV inspired by dragonflies. This resulted in a biplane flapping-wing MAV, called DelFly. DelFly is able to hover and has an onboard camera for observation and vision-based control. Since the start of the DelFly project, it has been successful at various competitions and evolved into a better model called DelFly II, see figure 1.1. DelFly II is already capable of some autonomous flight and the goal is to keep improving the design to a very small fully autonomous aircraft. The latest model, the DelFly micro, weighs only 3 grams and has a wing span of just 100 mm.

The success of the DelFly project has triggered investigations into the various aspects of this flapping-wing MAV. Among these, also research into the aerodynamic and aeroelastic behaviour of the DelFly wings is conducted, where the presented work is considered to be part of.



Figure 1.1. The flapping MAV DelFly II © Jaap Oldenkamp

1.1 Motivation

The study of the aerodynamics is an important part of the research on the DelFly. Contrary to fixed wing aircraft the DelFly's flapping wing design leads to various unsteady aerodynamic phenomena and due to the flexible Mylar foil wings there is a strong fluid structure interaction. A better understanding of these effects can help to understand and further improve the DelFly design. In the recent past, aerodynamic research has been performed by De Clercq^[1] into lift generation during the flap cycle of the DelFly II. This has been done by using an experimental technique called *Particle Image Velocimetry* (PIV). During this research a high speed camera captured images of particles seeded in the air around the DelFly illuminated by a laser. The images were used to study the instantaneous velocity field which could be related to the lift force at that moment, as obtained by simultaneous force measurements. The existence of vortices developing during the flapping cycle was demonstrated and the DelFly specific *clap-and-peel* mechanism was shown to be effective in enhancing lift for the DelFly II. Although providing valuable first insights in the flow around the DelFly wing during flapping, the PIV research also encountered some problems with light reflections and poor repeatability due to the fragility of the model. The construction of a new DelFly model and modification of the experimental PIV set-up could help solve these problems. The opportunity to improve the model construction and the experimental aerodynamic analysis supported the need for continued research on this subject.

The new study on the aerodynamics and aeroelasticity, presented in this report, focuses on vortex development. The goal of this new research will be:

Gain a better understanding of the aerodynamic mechanisms generating forces on a hovering flapping-wing MAV. With the purpose to further improve it.

For the research, again PIV is used as experimental technique to perform the flow field measurements. A new experimental set-up is constructed, which again considers a full-scale DelFly II model in hovering condition (vertical). The set-up contains two perpendicular placed force sensors, which makes it possible to perform lift and drag measurements. The set-up also enables power measurements and allows the DelFly model to be controlled from a computer. Since leading edge vortices in insect flight are identified as the most important unsteady aerodynamic mechanism enhancing lift generation for insects, the development of these vortices

for the DelFly are very interesting. The vortex development is studied for various wings, at various flapping frequencies and at various spanwise positions.

Parallel and closely related to the presented research, is the research carried out by Bart Bruggeman^[2]. During the research of Bruggeman a more robust and more efficient driving mechanism was developed. Also a wing geometry study has been carried out. Thrust and power measurements were performed on the same experimental force-measuring set-up as used in the presented research. An optimization study resulted in a new, more efficient wing. In the current aerodynamic study both the original DelFly II wing and the improved wing were investigated.

1.2 Thesis outline

The report has the following structure. In chapter 2 a number of fundamental aspects of flapping wing aerodynamics are discussed. Since the flapping flight of DelFly can be related to that of insects, this chapter discusses some of the aerodynamic and aeroelastic mechanisms related to insect flight. The third chapter presents the research subject: the DelFly II. In this chapter the DelFly's design and flight kinematics are described and also some of the previous research performed on the DelFly is summarized. The fourth chapter gives a brief explanation of the basic working principle of the (stereoscopic) PIV method used for the flow measurements. In chapter five the experimental set-up is described. The specific application of PIV to this research is described and also the set-up of the force and power measurements is described. The sixth chapter discusses the results of the force measurements and the flow field investigations. The concluding chapter summarizes the findings of chapter 6 and gives recommendations for further research on the DelFly.

Chapter 2

Flapping wing aerodynamics

The lift generation from the flapping wings of DelFly is based on the same aerodynamic principles as that of flapping wing insects. Insect flight has been studied for many years, but it is only since the last decades the basic aerodynamics behind it has been understood. This chapter discusses some of these studies and some of the different aerodynamic mechanisms that have been identified in these studies.

2.1 Introduction to flapping flight

The aerodynamics of flapping flight differs greatly from that of fixed wings. According to fixed wing theory, insects cannot even produce enough lift to sustain flight^[3]. Although insect flight has been studied for a long time, the small size and high stroke frequency of insect flight made it a difficult subject to investigate^[4]. Only since the availability of high speed cameras the flight kinematics and flow behaviour started to be understood. A thorough investigation of the kinematics of free flying insects that relied on high speed film was done by Ellington (1984)^[5]. Later the research of Ellington *et al.* (1996)^[3], using smoke visualization on a tethered hawkmoth and a mechanical model, revealed interesting phenomena like a leading edge vortex enhancing lift.

Recently, the need for small autonomous flyers for aerial reconnaissance has increased interest in MAVs of all sorts^[6]. As these vehicles typically operate under conditions similar to that of (large) insects, this has promoted flapping flight research even further. Various aspects of flapping flight have been investigated on robotic wing models, as described in the work of Ellington (1999)^[6], Birch *et al.* (2004)^[7], Singh *et al.* (2005)^[8] and many others. Reviews on the various aspects of flapping flight were made by Sane (2003)^[4] and Lehmann (2004 and 2008)^{[9][10]}.

The advent of PIV as a new experimental flow diagnostic technique provided the opportunity to quantify the entire instantaneous flow field around a flapping wing. At the same time, the increase in computational power made it possible to perform more accurate numerical simulations of flapping flight. These powerful and complementary approaches for flow analysis allow to study the details of flapping flight. Recent research using PIV done by Ansari *et al.* (2009)^[11], have shown the aerodynamics of a rotating wing to correspond to CFD results of Wilkins and Knowles (2007)^[12].

2.1.1 Wing kinematics

Insects use a reciprocating wing motion for flight^[13]. This motion may be decomposed in three motions: sweeping (fore and aft movement), heaving (up and down movement) and pitching (changing incidence angle). In figure 2.1 a schematic representation of the wing motion is shown. A complete flap cycle consists of twice a translation (a down-stroke and an up-stroke) and twice a rotation (termed pronation at the end of the down-stroke and supination at the end of the up-stroke). During the translation the wing shows a sweeping and heaving motion and almost no pitching. While at the end of a half-stroke during stroke reversal (rotation) the wing pitches rapidly. The exact wing kinematics varies among different insects and for different flight manoeuvres. Insects may change their stroke angle, angle of attack and wing rotation^[14].

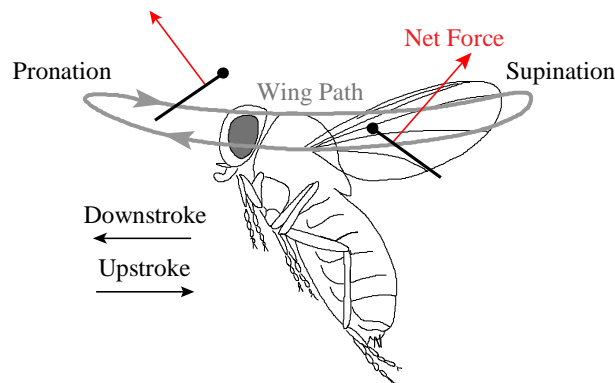


Figure 2.1. Insect wing motion. The black lines represent the position of the wing cross-section, with the leading edge marked with a solid circle. Adapted from Singh *et al.*^[8]

2.1.2 Aerodynamic mechanisms

The work of Dickinson *et al.* (1999)^[15] identifies three mechanisms enhancing the aerodynamic performance of insects: delayed stall (known as the leading edge vortex effect), rotational forces and wake capture. A fourth mechanism, already described previously by Weis-Fogh in 1973^[16], is the clap-and-fling mechanism. This wing-wing interaction is found on some insects during dorsal wing rotation. In the remainder of this chapter these four mechanisms of flapping flight are described. In paragraph 2.2 the occurrence of a leading edge vortex due to the delayed stall effect during the translational motion of flapping flight is described. In paragraph 2.3 the rotational forces enhancing lift during wing rotation are discussed. In paragraph 2.4 wing-wake interaction, or wake capture, is described. The clap-and-fling mechanism during dorsal stroke reversal is described in paragraph 2.5. Finally some effects of wing flexibility in flapping flight are discussed in paragraph 2.6.

2.2 The Leading Edge Vortex

In insect flight most lift is produced during the translational motion of the wing^[9]. During the translation there is a gradual build-up of lift around the airfoil. The same happens for fixed wing aircraft when starting to move forward. According to the Kutta-Zhoukowskii theorem which relates lift to circulation, with increasing lift also the circulation grows^[17]. Kelvin's law states that the total amount of angular momentum in the entire flow field remains constant. In consequence, the bound circulation around the airfoil is balanced by a starting vortex of equal strength, see figure 2.2.



Figure 2.2. An impulsive started airfoil sheds a starting vortex

In insect flight there is an additional mechanism to enhance the lift. Due to a thin airfoil, the flow can separate directly from the leading edge for high angle of attacks. Instead of stalling completely, the stall is delayed during the flapping motion and the flow reattaches further down the airfoil, to form a *leading edge vortex* (LEV). This extra vorticity adds to the bound circulation of the airfoil to enhance the lift^[9]. In contrast to blunt airfoils where the flow stays attached on the upper side of the airfoil and forms a suction peak on the nose, the LEV forms a suction force on the upper surface that increases both lift and drag^[4], see figure 2.3.

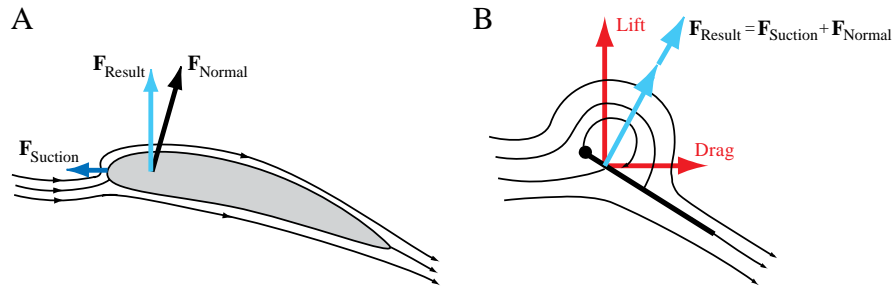


Figure 2.3. Leading edge suction. The sharp diversion of flow around a blunt airfoil (A) results in a suction force that tilts the normal force towards the leading edge. While the leading edge vortex on a thin airfoil (B) gives an extra suction force parallel to the normal force giving rise to extra lift and drag. Adapted from Sane^[4]

The LEV is already well known to enhance the lift on delta wing aircraft. A spanwise flow at these aircraft due to a favourable pressure gradient along the leading edge is one of the reasons why a stable LEV is present^[18]. Insect flight, however deals with much lower Reynolds numbers. At Reynolds numbers of order 10^3 extensive research has been done to investigate the LEV in the flight of the hawkmoth, *Manduca Sexta*^{[19][20]}. It was found that the LEV started from a condition of dynamic stall and formed a conical leading edge spiral vortex analogous to delta wing aircraft. An explanation for the stability of the LEV is that a spiralling axial flow within the vortex core transports energy into the tip vortex. Later research by Birch *et al.*^[7] on a robotic wing showed the LEV flow structure and spanwise flow to depend on Reynolds number. Where a spanwise flow at $Re = 1400$ was present, but at $Re = 120$ it was not observed. The LEV on various insects may therefore appear as (or be composed of) several various flow structures. Figure 2.4A shows the LEV conical structure as described for the hawkmoth, while figure 2.4B shows an LEV structure found for a butterfly where the LEV spans across the body and a spanwise flow in the LEV core is absent^[21].

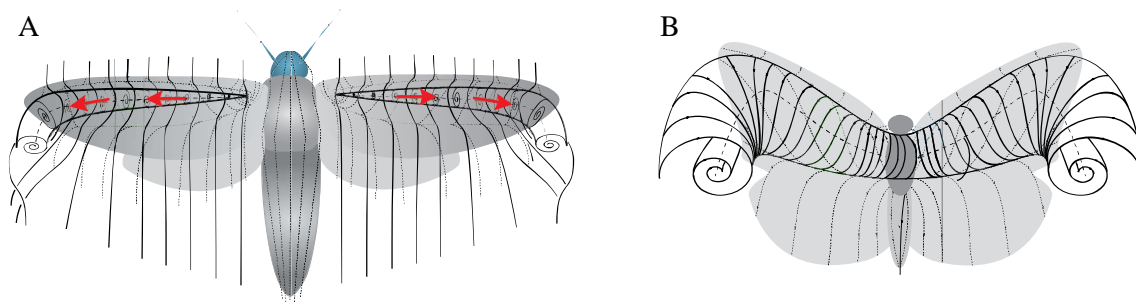


Figure 2.4. Two LEV structures. (A) Structure described by Ellington and Birch for a hawkmoth, where the LEV is a conical spiral with spanwise flow in the vortex core. (B) Structure found by Srygley and Thomas for a butterfly, where a single LEV is extending across the thorax and no significant spanwise flow is present. Adapted from Bomphrey *et al.* ^[21]

2.3 Rotational forces and the Kramer effect

The previous paragraph described that most of the lift during insect flight is generated during the translation. Direct measurements on a tethered flying fruit fly, *Drosophila melanogaster*, however, have shown that peak forces are produced during wing rotation ^[9]. This might mean that insects also use wing rotation as a lift enhancing mechanism. Force measurements on a dynamically scaled robotic wing based on a fruit fly by Dickinson *et al.* ^[15] show these force peaks to depend on the timing of the rotation. When the wing starts and finishes the rotation before it reverses direction, termed advanced rotation, a high lift peak can be seen during rotation. But when the wing starts the rotation after stroke reversal, so when already starting the next stroke, which is termed delayed rotation, it results in a negative lift peak. Insects show rather symmetrical rotation, which also results in force peaks during rotation, see figure 2.5.

An explanation for the rotational forces may lie in the dynamic location of the rotational axis. During advanced rotation the rotational axis appears to be at the leading edge. This will add positive rotational circulation to the translational circulation which results in a lift peak at the end of each stroke. For delayed rotation, the rotational axis lies at the trailing edge. This, on its turn, will add a negative rotational circulation to the translational circulation and result in a negative lift peak ^[22].

Another rotational phenomenon is the Kramer effect called after M. Kramer who first described it in 1932 ^[4]. This effect is the ability of a rotating airfoil to experience higher lift coefficients than the maximum steady lift coefficient ^[9]. A steadily increasing angle of attack with a positive rotational spin gives an increase in maximum lift coefficient and vice versa. Interesting to note is that while in this and some other literature such as Lehmann (2004) ^[9] a distinction is made between the two mechanisms above, some other literature merge them together, termed either rotational forces (Sane and Dickinson, 2002 ^[22]) or Kramer effect (Sane, 2003 ^[4]).

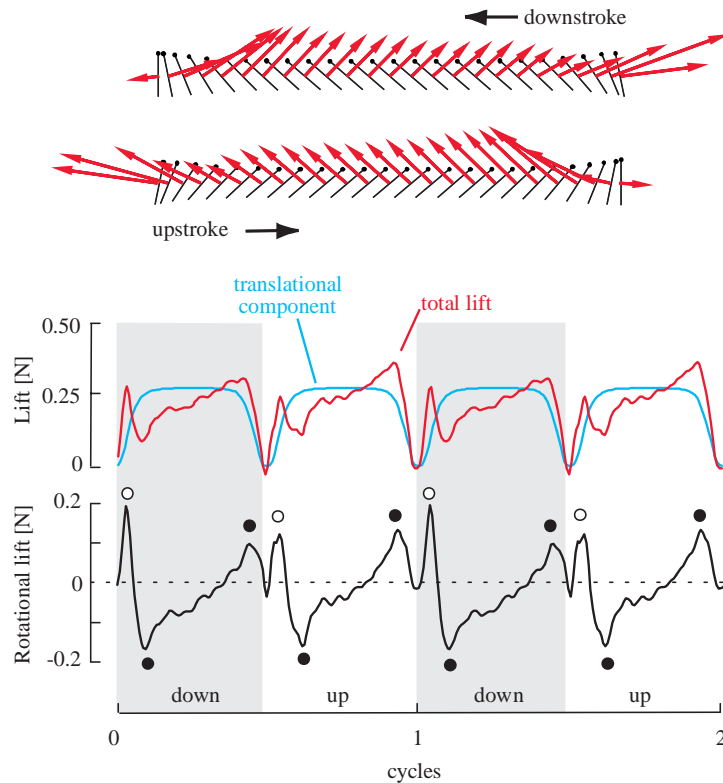


Figure 2.5. Lift force measured on a dynamically scaled robotic wing based on a fruit fly ($Re = 136$). Measured lift (red) shows force peaks during rotation compared with an estimated translation force (blue) for symmetrical rotation (above). The rotational lift (below) is the difference between the measured and predicted force. Peaks attributed to rotational circulation are indicated with black dots, peaks attributed to wake capture are indicated with white dots. Adapted from Dickinson *et al.* ^[15]

2.4 Wing-wake interaction

Due to the nature of flapping flight a wing encounters its own wake. This is the case especially during hovering, since without free-stream velocity, vortices are shed in the wake more slowly and remain in the vicinity of the wings. The interaction of the wing with its own wake might have a positive effect on the lift generation. This mechanism, termed wake capture or wing-wake interaction, has been studied on a robotic fruit fly by Dickinson *et al.* ^[15]. During stroke reversal vorticity on the leading and trailing edge is shed. These vortices are thought to create an inter-vortex jet that the wing encounters after stroke reversal and enhance lift generation, as can be seen in figure 2.6.

The direction of this extra lift force again depends on the wing position. The lift force contribution will be positive when the wake is captured when the wing is already rotated (advanced rotation), while it is negative for delayed rotation. The wing wake interaction was found to be different from the rotational forces described in the previous section, since this force is also present when the wing was stopped at the end of translation ^[15]. Forces attributed to the wake capture mechanism are also depicted in figure 2.5.

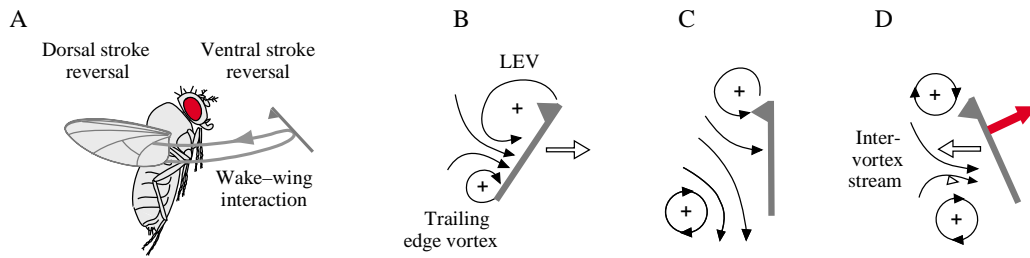


Figure 2.6. Wing-wake interaction. LEV and TEV during translation (B) are shed during rotation (C) and create an inter vortex stream at the start of the back stroke enhancing lift (D). Adapted from Lehmann^[10]

2.5 Clap-and-fling

Another mechanism that is considered to enhance lift is the clap-and-fling mechanism. This mechanism has first been described by Weis-Fogh in 1973^[16] and has since then been found on various insects that maximize their wing stroke by allowing physical contact between their wings at the end of the up-stroke^[9]. This mechanism may also be found in biplane robotic aircraft such as DeFly. Here the clap-and-fling is present between the upper and lower wings during the end of the in-stroke and beginning of the out-stroke.

A schematic representation of the clap-and-fling is shown in figure 2.7. At the end of the up-stroke (B) the leading edges of the wings touch each other before they pronate. The wings rotate around their leading edges until the wings are parallel (C), where air is expelled down from the closing gap to form a momentum jet enhancing lift. When the gap between the wings is closed the circulation of both wings cancel each other out. This ensures that the trailing edge vorticity is greatly attenuated or even absent. Since the trailing edge vorticity shed as a stopping vortex, slows down the build-up of circulation during the next stroke, called the Wagner effect, lift is built up more rapidly^[4].

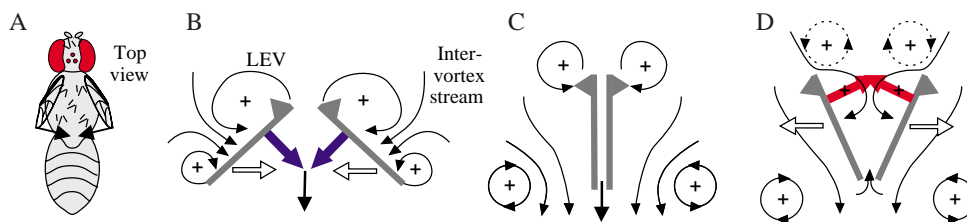


Figure 2.7. Schematic representation of the clap-and-fling mechanism. At the end of the up-stroke (B) the wings clap together (C) and fling apart (D). Adapted from Lehmann^[10]

During the second part of the motion the wings pronate around their trailing edges and the leading edges fling apart (D). This creates a low pressure region between the wings, which causes air to be sucked in and which is thought to give an initial impulse to the start of the build-up of new circulation, generating a stronger LEV. This circulation is opposite on both wings, so Kelvin's law is satisfied and in this phase there is no need for a starting vortex^[4].

The relative benefit of clap-and-fling depends on the wing kinematics^[10]. Insects flapping with a smaller stroke angle have relatively more advantage from clap-and-fling. Research of Lehmann and Pick^[14] on a robotic wing based on a fruit fly with a fixed stroke angle (160°) and

geometric angle of attack (50°) show the aerodynamic benefit of clap-and-fling also to vary for different heaving patterns. The increase in vertical force changes from 1.4% to 17.4% for varying heaving patterns. Figure 2.8 shows the vertical force for the depicted pear-shaped heaving pattern. For this pattern the increase in vertical force is 5.8%. It can be seen that the largest force increase is due to a peak during the fling phase.

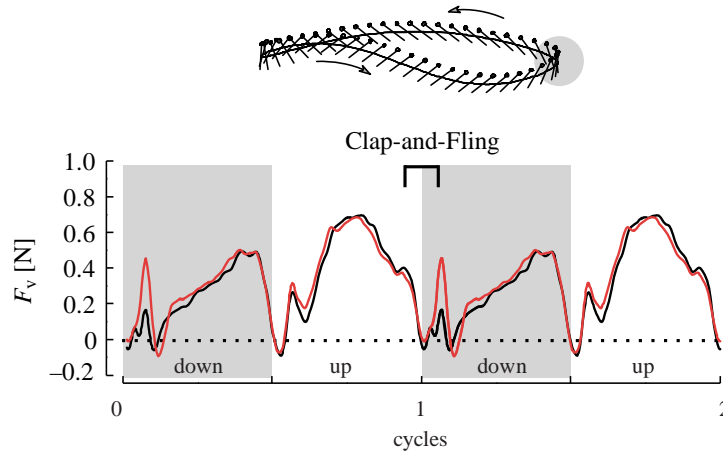


Figure 2.8. Vertical force measured on a robotic fruit fly wing showing clap-and-fling (red) compared with the same wing without clap-and-fling (black). In the heaving pattern (above) the grey region shows the location where the clap-and-fling takes place. Adapted from Lehmann and Pick^[14]

Research by Lehmann *et al.*^[23], using force and PIV measurements shows that the effect of clap-and-fling is not limited to the dorsal stroke reversal, but alters the whole spatio-temporal structure of the wake during the whole flap cycle. From the PIV analysis (see figure 2.9) a reduced downflow during the clap phase was observed due to the presence of an image wing (A), which is thought to attenuate the vertical force. During the fling a strong fluid influx was observed, interacting with the vortices from the up-stroke (C) and new LEVs during the down-stroke (D), enhancing the vertical force. Also an upward flow is present at the trailing edge during the end of the fling (D) where fluid is being sucked into the opening gap.

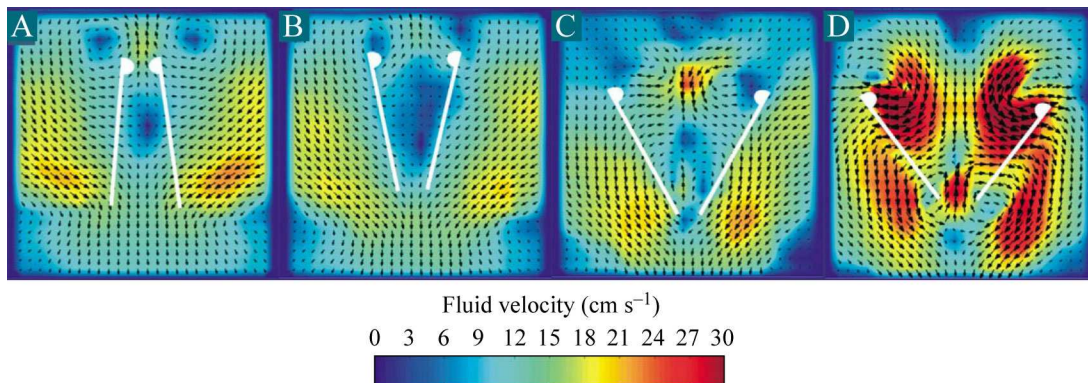


Figure 2.9. Flow field images from the PIV analysis during the clap-and-fling on a robotic fruit fly wing ($Re = 134$). Adapted from Lehmann *et al.*^[23]

2.6 Wing flexibility effects in flapping flight

In the description of the fling, as presented in the previous paragraph, the wings rotate around their trailing edge. Investigations on the fruit fly in tethered flight and on several other insects have shown the wings to rotate around their leading edge^[10]. Flexibility of the wings allows the wings to peel apart under influence of a strong fluid-structure interaction. This kinematic pattern has been termed clap-and-peel. During the peel, the elastic wings physically touch, closing the gap between the wings and preventing fluid from being sucked upward. In this sense it could be said that the actual clap, where the trailing edges clap together, is postponed such that the clap and the peel take place simultaneously. A numerical comparison of clap-and-peel with clap-and-fling at low Reynolds numbers ($Re < 64$) shows that the flexibility of the wings may reduce drag and improve lift^[24].

The wing deformation in insects and flapping-wing MAVs is usually a passive phenomenon, meaning that it is not actively controlled, but the result of the inertial, elastic and aerodynamic forces acting on the wings. Observations of the wing kinematics of the hawkmoth at 15% air density by Combes and Daniel^[25] revealed that the wing deformation is due mainly to elastic-inertial forces, where aerodynamic forces only play a minor role as a means of dampening mechanism. High speed camera images of the DelFly in vacuum, on the other hand, revealed that aerodynamic forces are important for the DelFly wing deformation (see paragraph 3.3). Since the DelFly has relatively large and thin Mylar foil wings, in-flight wing deformation is severe. Besides the clap-and-peel mechanism, wing flexibility is thought to also affect force production in other manners. Tests on the original DelFly revealed that increased spanwise flexibility, which makes a heaving motion possible, has positive effects on DelFly flight performance. Recent measurements performed by Heathcote *et al.*^[26] confirm the positive effect of spanwise flexibility.

The effect of chordwise flexibility has also been investigated. Numerical research^{[27][28]} has shown chordwise flexibility to also have a positive effect on force production. Investigations into the flow structure revealed a more attached LEV for a flexible wing, which could explain the larger force production. Experimental research on real hawkmoth wings by Mountcastle and Daniel^[29] show that fresh (more elastic) wings cause stronger downward fluid flows, and hence are more beneficial to lift than dry (more stiff) wings. A detailed data base of wings with varying wing elasticity was generated by Zhao *et al.*^[30] The experiments were performed on a robotic wing at $Re = 2000$, where it was shown that aerodynamic forces could be controlled by altering the flexibility of the trailing edge. Here it was found that a wing at moderate angle of attack with a more rigid trailing edge generated larger vortices and therefore increased aerodynamic forces. In the context of the present investigation, the effect of wing flexibility on DelFly has been investigated by changing the wing stiffeners location and orientation, as can be read in chapter 3.

Chapter 3

The flapping MAV DeIFly

DeIFly is a bio-inspired ornithopter designed and built at Delft University of Technology (DUT). The DeIFly project started as a student design project in 2005. The first version of DeIFly, a vision based flapping MAV, won the price for the most exotic design during the EMAV '05 competition in the summer of 2005^[31]. Since that moment, the interest and research into flapping MAVs has increased at DUT. For the DeIFly project a top-down approach is followed, where from the study of a relative large model experience and theoretical insights can be gained, that can assist to create smaller, functional versions of the DeIFly^[32]. New research led to an improved version of DeIFly, called the DeIFly II, see figure 3.1. For DeIFly II the wing span had decreased from 330 mm to 280 mm and the weight had been reduced from 22 g to 17 g. Furthermore the V-tail had been abandoned in favour of a more conventional cross-tail. This meant the DeIFly II was more stable and better controllable.



Figure 3.1. The flapping MAV DeIFly II in flight © Jaap Oldenkamp

In 2008, a further down scaled version of DeIFly was developed, DeIFly Micro. This version has 100 mm span and weighs only 3 g, while it still carries an onboard camera. This small flapping MAV is capable of forward flight, but it is not yet capable to hover. DeIFly II, on the other hand, is able to hover and is more stable. DeIFly II has been the subject of much of the previous research, making it a proven and well-tested configuration. This is the reason why also the subject of the current study is chosen to be the DeIFly II, in this report further referenced as simply DeIFly.

This chapter will describe the DelFly II design and construction and discusses some of the previous research performed on DelFly. In paragraph 3.1 the design of DelFly is described; its dimensions, the wing configuration, the driving mechanism and materials used for construction. In paragraph 3.2 the DelFly flight kinematics are described, while paragraph 3.3 summarizes some elements of the previous research performed to investigate the aerodynamic behaviour of the DelFly.

3.1 DelFly design

The DelFly has a biplane flapping wing design. The main fuselage is a light carbon tube and the front part is a sandwich construction from 2.5 mm balsa wood and carbon cloth^[32]. The crankshaft mechanism operating the wings is driven by a brushless motor for low resistance. Another advantage of this type of motor is that it allows more accurate measurements to the motor, while measurements to a brushed motor would prevent accurate measurements due to heating and fast ageing of this type of motor^[31]. The motor drives pushrods up and down via a gearbox with gear ratio 1:20. The pushrods are connected to hinges, in which the wing leading edges are mounted, see figure 3.2.

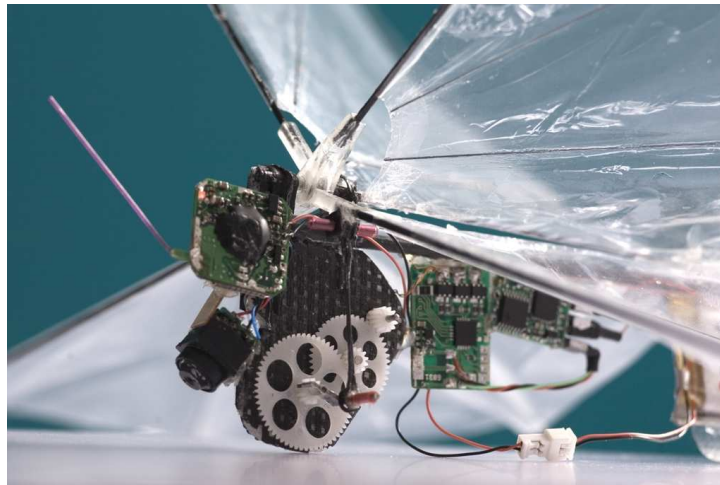


Figure 3.2. Photo of the DelFly showing the driving mechanism, with a camera mounted on the front © Jaap Oldenkamp

The wing and tail surface is made out of 5 micron thick Mylar foil. The wings have D-shaped carbon rods (0.7 x 1.4 mm) as leading edges and the wing foil is reinforced by carbon stiffeners ($\varnothing 0.28$ mm)^[31]. The wings are placed under a small positive dihedral angle, ψ , of 12 degrees and have a maximum flap angle, ϕ , of 44 degrees. Past research^[33] has shown that the most power efficient operation occurs at a maximum flap angle of approximately 30 degrees, however in its present configuration the DelFly has a maximum flap angle of 44 degrees to maximize the payload lifting capability. The layout and dimensions of the DelFly wing are given in figure 3.3. DelFly has a semi span R of 140 mm and a semi wing area S of 112 cm². More complete specifications are given in appendix A.

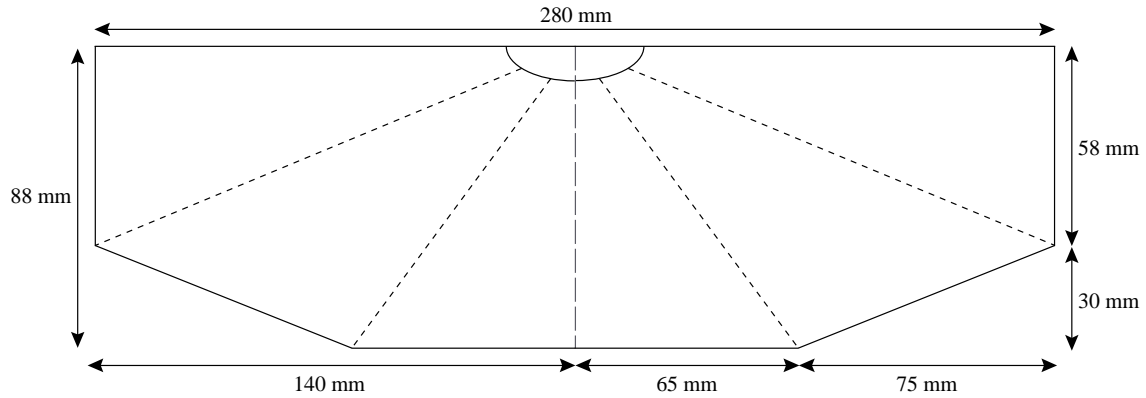


Figure 3.3. DelFly wing layout, showing dimensions and stiffeners (dashed)

3.1.1 Similarity parameters

Dimensionless parameters characterising the flight kinematics and aerodynamics of the DelFly, allow for a meaningful comparison to be made to other MAVs or to insects. This report uses the same conventions as used by Ellington^[6]. As dimensionless measure for the flight speed, the flight velocity is divided by the mean wing tip velocity. By analogy to propeller theory this is called the advance ratio J :

$$J = \frac{V_{\infty}}{\bar{V}_t} \quad (3.1)$$

For the DelFly, J varies from 3.0 during maximum forward velocity to 0 for hovering, see paragraph 3.2.

Unsteady aerodynamic mechanisms in flapping flight are also affected by viscous forces, expressed by the scaling of the Reynolds number^[6]. The Reynolds number, Re , is the ratio of inertial forces to viscous forces in a fluid. The Reynolds number is defined here based on the mean chord length and the mean wing tip velocity:

$$Re = \frac{\bar{c}\bar{V}_t}{\nu} \quad (3.2)$$

The Reynolds number range at which the DelFly operates varies from approximately 38,000 during maximum forward flight to 15,000 during hovering flight.

Other similarity parameters of importance for flapping flight are the Strouhal number, St , and Rossby number, Ro . The latter relates the inertial forces to Coriolis forces and is defined as^[34]:

$$Ro = \frac{\bar{V}_t^2}{\Omega^2 R \bar{c}} \quad (3.3)$$

Where Ω is the mean angular velocity. The Strouhal number is non-dimensional frequency, based on wing flapping amplitude A and mean tip velocity V_t :

$$St = \frac{f A}{\bar{V}_t} \quad (3.4)$$

The value of the Strouhal number is known to have an important influence on the structure of the vortex wake produced by flapping flight and, hence, on thrust generation^[35]. Many animals, among birds, insects and bats, cruise at a narrow range of Strouhal number, between 0.2 and 0.4^[36]. A minimum Strouhal number for thrust production has been identified as approximately 0.06^[35]. DelFly flies at Strouhal numbers in the range of approximately 0.16 for maximum flight velocity to 0.49 for hovering flight, see appendix A.

3.2 Flight kinematics

The DelFly has a broad flight envelope, capable of 7 m/s forward flight, hovering and even up to 1 m/s backward flight^[32]. The range in terms of advance ratio is 3.0 to 0, which is large compared to insect flight. The maximum advance ratio for larger insect like the bumble bee and the hawkmoth, is typically in the order of 1.0^[6].

In forward flight the relative velocity on the wing is determined by the flight velocity (V_{flight}), the flap velocity (V_{flap} , determined by the flapping frequency) and the downwash velocity (V_{down})^[11]. The flight velocity is related to the orientation of the DelFly, at large forward velocity the DelFly is positioned almost horizontally and the flap plane is close to vertical. The thrust, by definition oriented along the fuselage, is primarily used to overcome drag, while much of the lift (to overcome body weight) is generated by the flight velocity, similar to conventional fixed wings, see figure 3.4. The flapping frequency is approximately 11 Hz for level flight^[2].

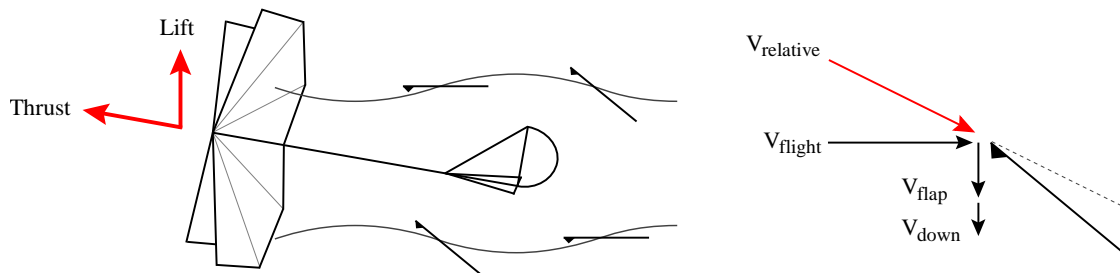


Figure 3.4. Side view of DelFly in level flight, with an indication of the wing chord orientation during the flapping motion, where the bottom of the leading edge is indicated with a triangle. Also indicated is the orientation of the force and velocity vectors, with arbitrary vector size

For hovering flight the DelFly is oriented vertically and the flap plane is horizontal, see figure 3.5. The relative velocity is now only determined by the flap velocity and downwash. The thrust vector is also tilted in vertical direction and is now the provider of the lift force. The wing motion is symmetrical and aerodynamic forces on the wings in the horizontal plane cancel each other out. The flapping frequency needs to be increased for sustained hovering flight and is approximately 13 Hz.

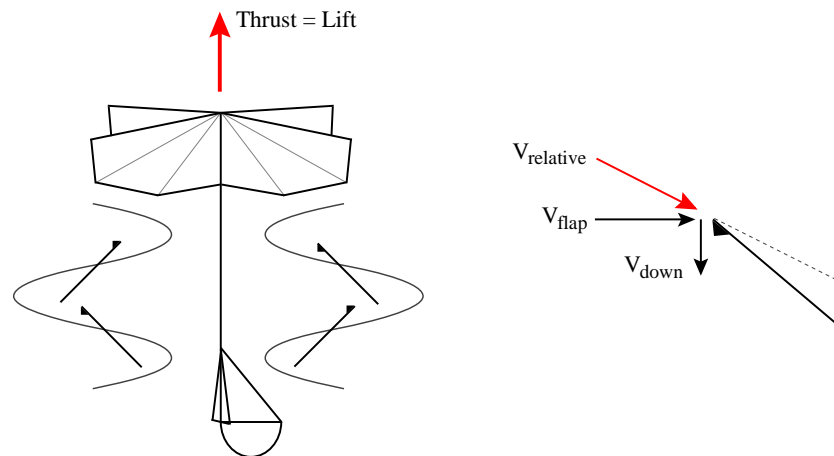


Figure 3.5. Side view of DelFly in hovering flight, with an indication of the wing chord orientation during the flapping motion, where the bottom of the leading edge is indicated with a triangle. Also indicated is the orientation of the force and velocity vectors, with arbitrary vector size

3.3 Research and development

From the start in 2005 the DelFly project has been subject of research to improve it on various fields of interest. From the development of DelFly II in 2006, this version of the DelFly has been the main research platform. This research has led to various structural improvements, as well as improvements in the area of aerodynamics and control and stability. Because of its stable flight, DelFly is especially suited for experiments with autonomous flight. Recently, at the IMAV 2010, full autonomous vision-based flight has been demonstrated ^[37]. In this paragraph some of the relevant research on DelFly is discussed.

3.3.1 Aerodynamics and aeroelasticity

During each wing beat of the DelFly, its wings are subjected to severe passive wing deformation. Research into the wing deformation under normal and under vacuum conditions performed independently by Bradshaw in 2008 ^[33] and by Groen and Bruggeman in 2010 has shown that both aerodynamic forces as well as elastic-inertial forces are important. Figure 3.6 shows high speed images of the wing deformation in air and in vacuum. Under vacuum conditions the wing surface behaves more rigid in chordwise direction and during wing rotation the elastic inertial forces cause the trailing edge to overshoot the motion of the leading edge due to the lack of aerodynamic dampening. When air is present, the aerodynamic forces cause the wing to heave and show chordwise deformation. A detailed description of the in flight wing shape is found in paragraph 6.2.

The wing deformation due to aerodynamic forces is especial apparent during wing rotation. The flexible structure of the wing gives rise to the clap-and-peel mechanism during the wing rotation preceding the out-stroke, see paragraph 2.6. Aerodynamic research performed by De Clercq in 2009 ^[1] using PIV focussed on the clap-and-peel mechanism. The research has shown that the most important augmentation in lift generation is due to the peel motion during the out-stroke. This gives a more gradual build-up of the circulation, which is thought to prevent an unstable LEV from shedding. The PIV analysis revealed a conical vortex structure above the leading edges during the out-stroke. At the moment the leading edges clap together an upward fluid

motion was observed. During the clap of the trailing edges, a momentum jet augmenting the lift was present at some positions along the span. The downward expelled fluid was thought to roll up in two vortices. During the rotation preceding the in-stroke an LEV was thought to form and together with the shedding of a starting vortex enhance the thrust during the in-stroke. This LEV was, however, not visible due to optical blockage by the wing itself.

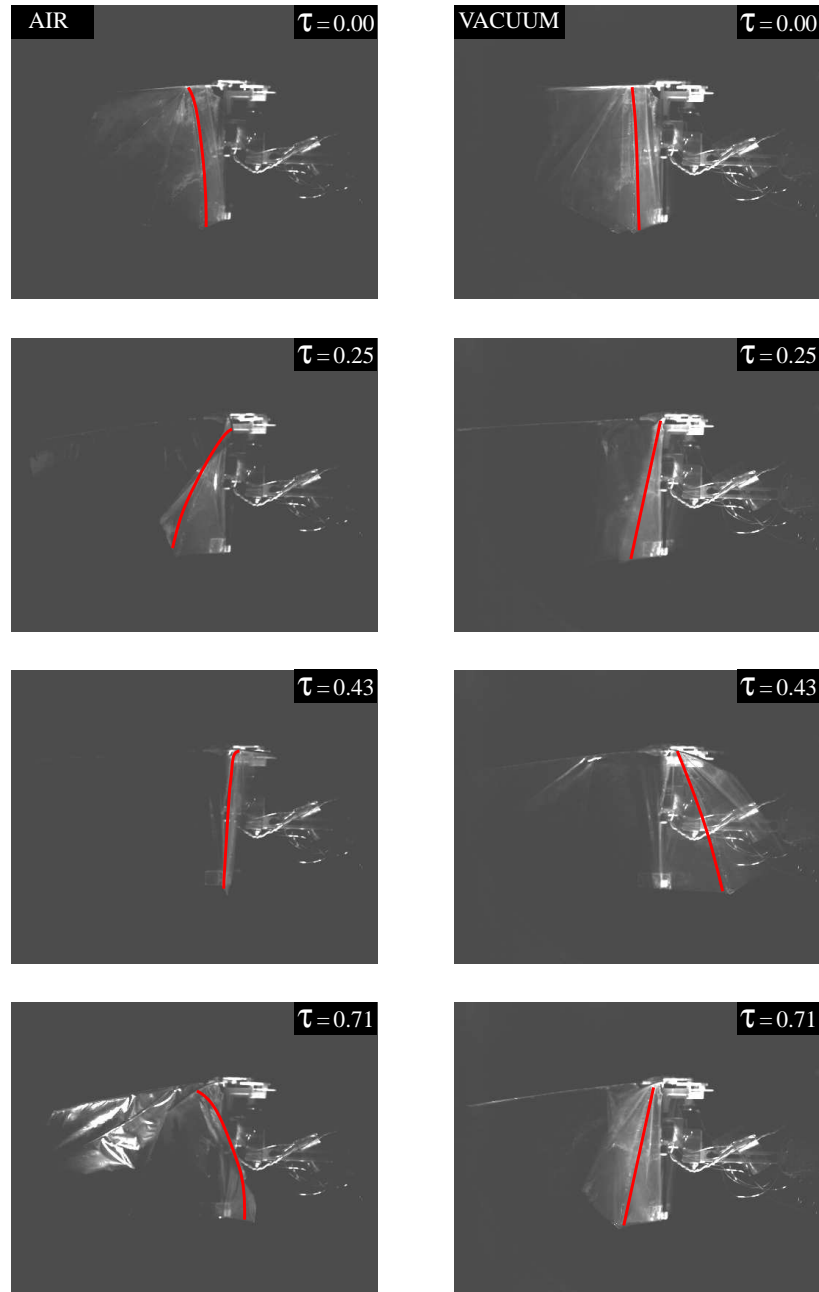


Figure 3.6. High speed images of the DelFly flapping at 12 Hz in air and in vacuum at various percentages of the flap cycle. In red a cross-section of the wing chord is sketched at approximately 50% wing span. The phase in the flap cycle is indicated with τ . At $\tau = 0$ the leading edges touch, with $0 < \tau < 0.5$ being the out-stroke and $0.5 < \tau < 1$ the in-stroke

3.3.2 Performance improvements

Parallel with the research presented in this report, a structural research into performance improvement was performed by Bart Bruggeman^[2]. During the research of Bruggeman a new driving mechanism was developed and a wing geometry study was performed in order to optimize wing performance.

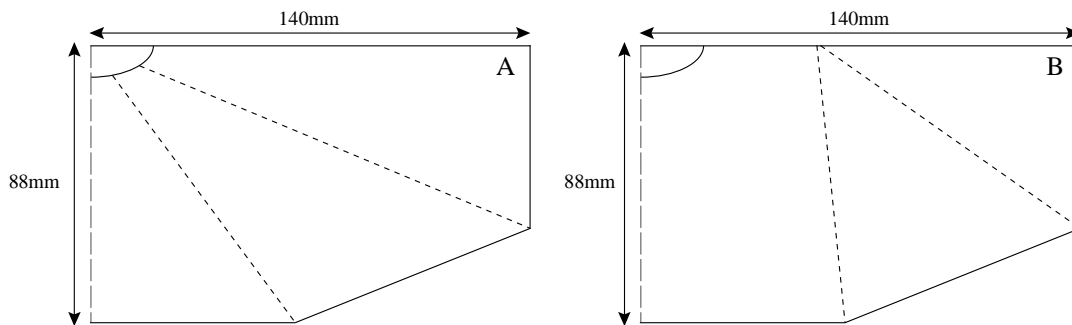


Figure 3.7. Stiffener location and orientation of the original wing (A) is changed for the improved wing (B), while the wing surface area and layout is kept unchanged

For the wing geometry study a systematic approach was followed, where the location and orientation of the stiffeners was varied, while other parameters such as wing area and wing shape were kept constant. Force and power consumption were measured on the same experimental set-up as described in chapter 5. As measure of performance the ratio of thrust over power consumption was used. The improved wing resulting from the wing geometry study (see figure 3.7) showed a 5% improvement in thrust-to-power ratio with respect to the original DelFly wing. The difference between the original and improved wing is especially found in the more favourable power consumption. The thrust generation of both wings is approximately equal (at the same flapping frequency) but the improved wing has a 5% reduction in power consumption.

The influence of stiffener thickness was also investigated. Increasing the stiffener thickness resulted in a higher thrust generation, but a lower thrust-to-power ratio. Also fixing the stiffeners to the leading edge led to a higher thrust, but lower thrust-to-power ratio, which is therefore thought to be an effect of the increased stiffness. Changing the area distribution to a more bat-like appearance had a positive effect on the thrust-to-power ratio, but the wing did not reach the thrust level needed for sustaining hovering flight.

During the research of Bruggeman also a new driving mechanism was developed. The new driving mechanism is made from polycarbonate, and manufactured using injection molding, see figure 3.8. This mechanical made driving mechanism is much more robust, better reproducible, 35% lighter and is made with smaller tolerances, than the original handmade mechanism. Since the motor and gears operate in the same plane as the hinges, the new driving mechanism is also more efficient. Important to note is that the research described in the remaining chapters of this report was performed with the original driving mechanism, since the new driving mechanism was not available at that time.

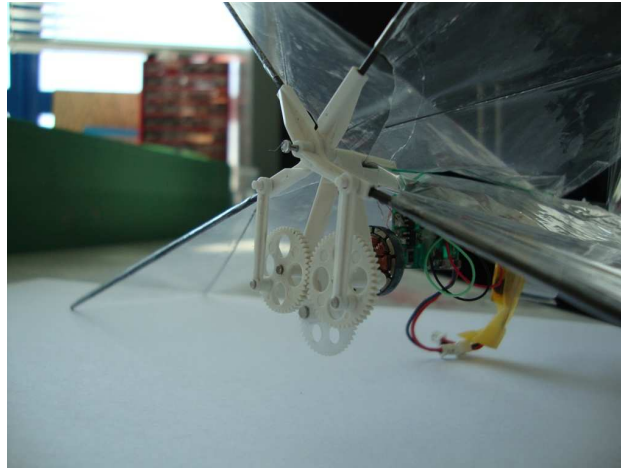


Figure 3.8. Photo of the DelFly showing the improved driving mechanism

The improvements in power consumption from the research of Bruggeman are summarised in figure 3.9 (for these measurements the thrust generation is approximately equal at the same flapping frequency). For the DelFly model operating at a flapping frequency of 13 Hz (hovering conditions), the improved mechanism resulted in a 20% power reduction and the improved wing for a 5% power reduction. In total an improvement of 25% in the thrust-to-power ratio was obtained.

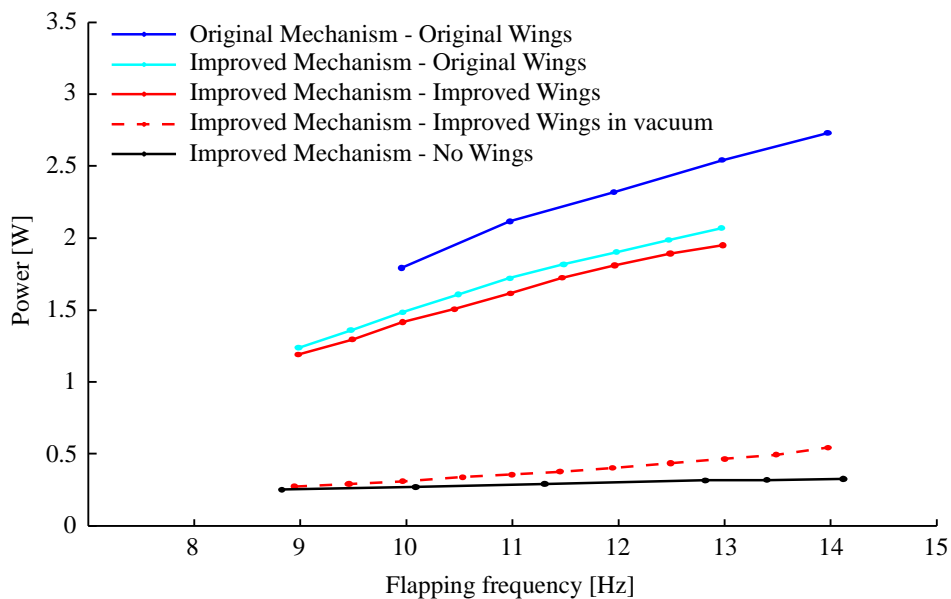


Figure 3.9. Average power consumption, showing the improvements from the new wings and new driving mechanism

The measurements performed in vacuum conditions by Groen and Bruggeman made it possible to estimate which percentage of the power consumption is due to mechanical losses and elastic-inertial effects. These results are also shown in figure 3.9. For the improved wing mounted on the improved mechanism flapping at 13 Hz, the power required to overcome the elastic-inertial forces is 8% of the total power consumption in air. The power required to drive the motor, gears and hinges accounts for 16% of the total power consumption in air.

The aerodynamic power, defined as the total power consumption in air minus the power consumption in vacuum^[33], is approximately constant for both the improved and original wing along the operational frequency range and is $77\% \pm 2\%$ of the total power consumption in air. These results, for a DelFly operating at a stroke angle of 44 degrees, show a higher contribution of the aerodynamic component than in the results of Bradshaw *et al.*^[33]. The research of Bradshaw *et al.* showed the aerodynamic power to be approximately 50% for a stroke angle of 36 degrees and 20% for a stroke angle of 24 degrees. The results of the new experiments confirm this trend, that the relative contribution of the aerodynamic sources to the total power consumption increases with the stroke angle.

Chapter 4

Particle Image Velocimetry

Particle Image Velocimetry (PIV) is a measurement technique that has been successful since it has been introduced about twenty years ago. PIV is a non-intrusive measurement technique that provides instantaneous information on the entire velocity field within the domain of observation^[38]. Due to the non-intrusive nature and ability to show the whole flow field, unsteady aerodynamic features such as separation and vortices can be studied, which makes PIV well suited for the investigation of flapping flight. In chapter 2 already some research has been described in which PIV was applied to flapping flight. Also during previous aerodynamic research on the DelFly carried out by De Clercq^[1], the flow around the flapping wings was studied with PIV. The research described in this report again uses PIV as main experimental measurement technique to further investigate the flow field during the hovering flight of the DelFly.

This chapter will briefly explain the basic operating principles of PIV in paragraph 4.1. In paragraph 4.2 the three-component PIV method, stereoscopic PIV, which has been used in the current research on the DelFly, is described. For a more complete review of PIV one is referred to Raffel *et al.*^[38]. The actual implementation of the PIV method in the present experiments is given in chapter 5.

4.1 Basic principles

PIV is based on the imaging of tracer particles that have been seeded into the flow, see figure 4.1. The particles need to be small enough to be considered non-intrusive to the flow and are considered to follow the flow without slip. The particles are illuminated by a light sheet, typically from a laser source, since they provide a high energy light source. The laser gives two light pulses during each of which the light scattered by the particles is captured in two separate images by a digital camera. The digital recordings are divided in small subareas called ‘interrogation areas’^[38]. The displacement of the particles between the two images is determined with statistical methods (cross-correlation), where it is assumed that the particles within the interrogation area have moved homogeneously. The local velocity vector in the imaging plane is then calculated by taking into account the time separation between the two illuminations and the magnification at imaging.

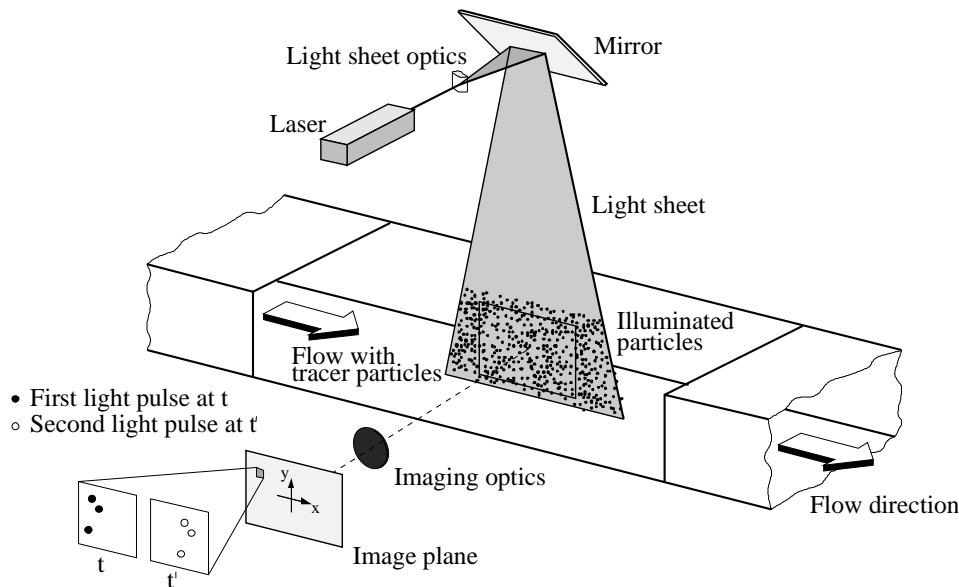


Figure 4.1. Experimental arrangement for PIV in a wind tunnel. Adapted from Raffel *et al.* [38]

PIV offers a non-intrusive velocity measurement. In contrast to measurement techniques that use probes in the flow field, like pressure tubes or hot wires, PIV uses optical techniques. This prevents the local flow field to be disturbed by the measurement itself. Another advantage of PIV is that it provides information on the whole instantaneous flow field. Because of the large spatial resolution, large structures in the flow can be detected, even in unsteady flows. Other measurement techniques (by means of probes like hot wire anemometry or optical techniques like Laser Doppler Velocimetry) determine the velocity in a single point. They, however, do so with an often (much) higher temporal resolution. The temporal resolution (frame rate of the images) of PIV measurements is restricted by the specifications of the technical equipment, notably the laser repetition rate and the camera sensor read-out speed.

PIV determines the particle velocity instead of the actual flow velocity. The fluid velocity measurement is therefore indirect, where it is assumed that the particles follow the flow without slip. The particles should therefore be small and light enough (ideally the particles should have the same density as the fluid) in order to have a small response time to variations in the fluid velocity. Response times of a $1\ \mu\text{m}$ particle in a strong decelerating air flow (step response) are in the order of $10\ \mu\text{s}$ [38] and should therefore especially be considered when dealing with high speed air flows and shockwaves.

Oposing the size requirement the particles should also possess good light scattering behaviour. The determination of the particle displacement from the PIV images is related to the contrast of the particles with respect to the background. Typical tracer particles used in air flows are fluid particles such as water based droplets or oil droplets and solid particles such as titanium dioxide (TiO_2). TiO_2 particles possess good scattering behaviour, but are also hazardous when inhaled, so should only be used in a closed-loop air flow. The light scattering also depends on observation angle. Figure 4.2 shows the polar distribution of the scattered light intensity for an oil particle in air for light with wave length of $532\ \text{nm}$ [38].

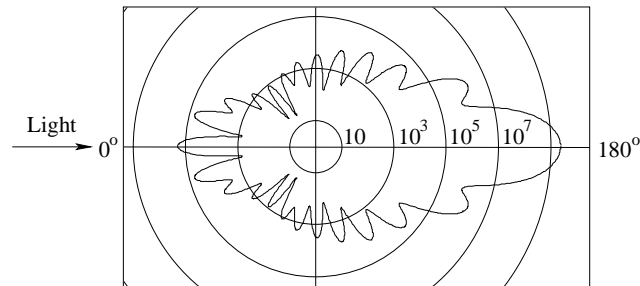


Figure 4.2. Light scattering by a 1 μm oil particle in air. Adapted from Raffel *et al.* ^[38]

Care and experience are required in the realization of a good PIV experiment, which involves a number of choices on the construction of the set-up and on the values of some typical PIV experimental parameters. The illumination and viewing geometry may impose restrictions, such that some parts of the flow field information can be lost due to reflections or blockage of the light sheet. When setting up a PIV experiment, the alignment of the laser sheet in the focal plane of the camera is important, as well as the geometrical calibration of the laser sheet optics and the imaging equipment.

The imaging system is characterized by the focal length of the imaging optics (lens), the aperture number $f_{\#}$ (given by the focal length divided by the aperture diameter) and the magnification M of the measurement plane on the image plane (field of view) ^[39]. The aperture number is important in determining the image size of particles (for a calculation of the aperture number and particle image size for the present research, see paragraph 5.5). Since the particles are geometrically small, the image size is largely determined by the diffraction effect. A higher aperture number leads to a larger particle image size. To permit a good determination of the velocity, it is important that the image size of a particle on the chip of the digital camera is larger than one pixel. When smaller, the particle displacement and hence the velocity can only be determined in discrete steps. This effect is called ‘peak locking’. A good image size for the particles is approximately 2 pixels, in that case sub-pixel accuracy can be obtained.

The laser pulse time should be short enough to avoid streaking and the time between the two pulses should be long enough to distinguish low velocities and short enough to prevent the out of plane velocity component to move the particles out of the light sheet, which deteriorates the correlation between the two images. The most common illumination device used for PIV experiments is the solid-state frequency-doubled Nd:YAG, that emits laser light with a wavelength of 532 nm ^[39]. It produces pulse energy ranging between 10 mJ and 1 J. With a very short pulse duration (between 5 and 15 ns) this instrument is suited to illuminate flows without any limit on the flow speed. The repetition rate of Nd:YAG systems ranges between 10 and 50 Hz. This low repetition rate poses a limitation in performing time-resolved experiments. As an alternative, also high speed PIV systems are available, which use a Nd:YLF laser. Nd:YLF lasers are capable of emitting pulses of energy between 10 and 30 mJ at a repetition rate of 1 to 5 kHz. When there is no need for a high repetition rate, the Nd:YAG provides better illumination of the particles. Because of the better illumination, the camera diaphragm can be smaller which means a higher aperture number and less chance of peak locking. To capture the images at a framing rate that matches the laser illumination rate, also different camera technologies are available: relatively slow, but high-quality CCD-cameras and the much faster CMOS cameras.

4.2 Stereoscopic PIV

A drawback of the ‘classical’ (i.e. planar) PIV method is the fact that it is only capable of recording the projection of the velocity vector into the plane of the light sheet^[38]. Information about the out-of-plane velocity component is lost, while the measured in-plane velocity components are affected by a perspective error. When two cameras are used in a stereoscopic set-up the perspective projection can be used to extract the out-of-plane velocity component, see figure 4.3.

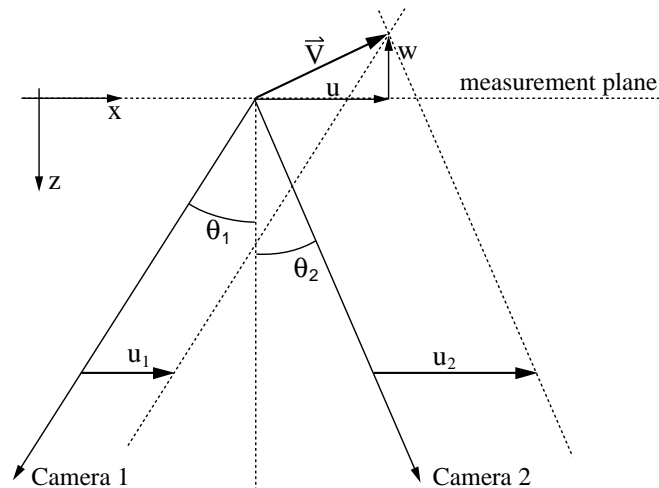


Figure 4.3. Stereo viewing in the XZ-plane. Adapted from Raffel *et al.*^[38]

The oblique camera angle results in a misalignment between the focal plane and the measurement plane. To correct this, the camera lens is mounted in a device that can tilt it from the image plane such that the focal plane and measurement plane are aligned (the Scheimpflug condition). The perspective distortion of the recorded images is corrected with the use of a calibration plate with a dotted pattern, see figure 4.4.

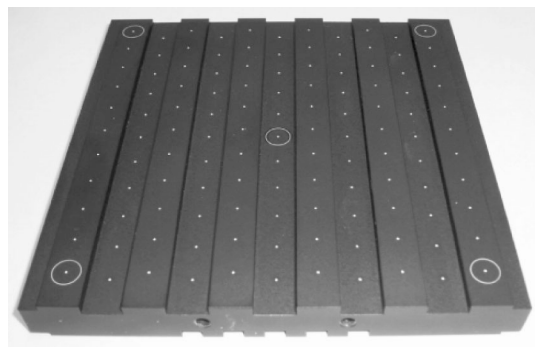


Figure 4.4. Two-level calibration plate. From Raffel *et al.*^[38]

The calibration plate is placed in the measurement plane and images are taken of the calibration plate. The pattern on the calibration plate can be used to relate the image dimensions to the actual geometric dimensions. An algorithm can be made that maps the pattern on the recorded image, to an aligned raster of dots on a reconstructed image, see figure 4.5. Once the mapping algorithm is determined it can be applied to reconstruct all recorded images.

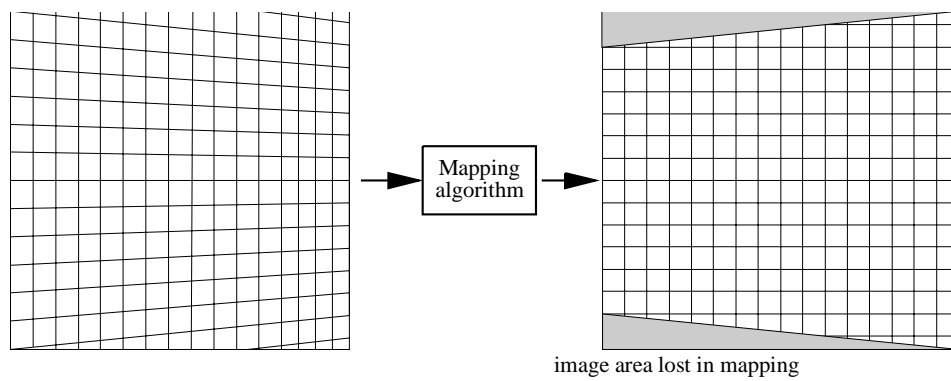


Figure 4.5. The mapping algorithm maps the recorded image (left) into a corrected image (right). Adapted from Raffel *et al.*^[38]

A small misalignment between the calibration plate and the measurement plane may still lead to calibration errors. To compensate for these remaining errors, a further calibration step can be applied. This method referred to as ‘self-calibration’, uses cross-correlation of images taken at the same moment by both stereoscopic placed cameras to further warp the corrected images such that the images of both cameras are exactly aligned.

Chapter 5

Experimental set-up

In chapter 2 the aerodynamic mechanisms of flapping flight are described. Much is still unknown about how these mechanisms work in providing lift for the DelFly and how the aerodynamic performance of the DelFly may be improved. In chapter 3 a new wing has been described which provides the DelFly with an improved thrust-to-power ratio. To gain a better understanding of the aerodynamic mechanisms during the flapping flight of DelFly II in general, as well as to compare the original DelFly II wing with the improved wing an experimental investigation has been conducted. During these measurements stereoscopic PIV is used to study the flow field structure. Simultaneously the upward force generated by the DelFly is measured as well as the power consumption.

In paragraph 5.1 the experimental set-up with the camera orientation is described and in paragraph 5.2 the two experimental campaigns with their test matrices are described. Paragraph 5.3 discusses the force measurement and DelFly control by means of a micro controller board. The PIV equipment used during the experiments is described in paragraph 5.4 and the settings used for this equipment can be found in paragraph 5.5.

5.1 Introduction to the experimental set-up

Experience gained by previous research carried out on the DelFly II by De Clercq in 2009^[1] was exploited in setting up the new experiments. In the research of De Clercq the flow field of a hovering DelFly was studied while at the same time forces were measured. The choice was made for the hovering flight regime, since all thrust generated by flapping is needed to stay airborne. From this perspective hovering flight is the most demanding flight mode within the flight envelope. Also in comparison to forward flight, unsteady flow features like vortices are expected to be more dominant within the flow. The flow field was studied using high speed PIV measurements. The upward force (thrust) was measured using strain gauge based load cells. A micro controller board was used for the control of the DelFly, the processing of the force measurements and the triggering of the PIV system. The focus of the research has been on the clap-and-peel mechanism. With this reason the laser sheet was oriented such that it was perpendicular to the symmetry plane between the upper and lower wing, see figure 5.1. The PIV measurements were performed with a high speed system, making a time resolved series of 500 images at a frequency of 1000 Hz. The measurements were performed at four spanwise locations (25%, 50%, 75% and 100% of the span) and for three different fields of view. As an

alternative also phase-locked measurements were performed at a span of 75%, where the flow field was averaged over 150 images.

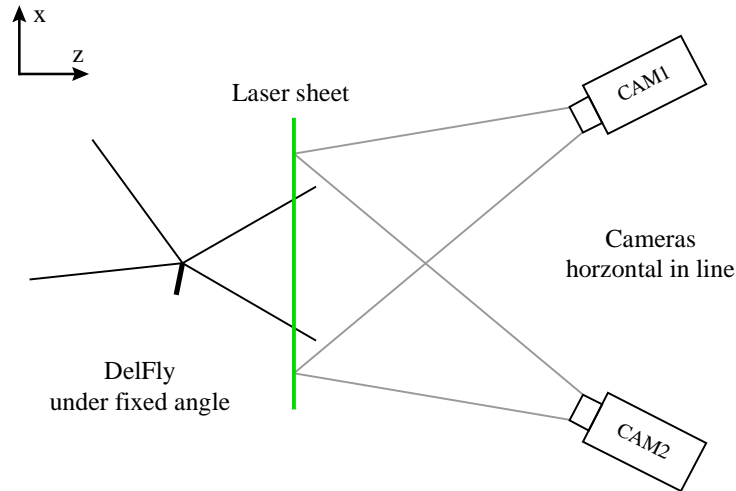


Figure 5.1. Top view of the experimental set-up as used by De Clercq^[1] with the cameras placed horizontal, where the illumination by the laser is from below, hence perpendicular to the figure plane

Also the current research considers the hovering flight set-up, since the previous research has left enough room for improvement and a lot of flow features remained unclear. A large problem encountered during the previous research was the laser light directly reflecting from the wing surface to the cameras. This meant that a large portion of the flow field remained unknown. A further drawback of this viewing approach, was that the laser sheet orientation remained fixed with respect to the DelFly body. This implied that for different wing positions the relative spanwise position of the measurement plane varied. Therefore, in the present investigation a phase-locked visualization approach was adapted, where the laser sheet is oriented perpendicular to the wing surface and the cameras are placed parallel to the leading edge, see figure 5.2. With this viewing approach direct reflections are significantly minimized and also measurements can be done on a constant span.

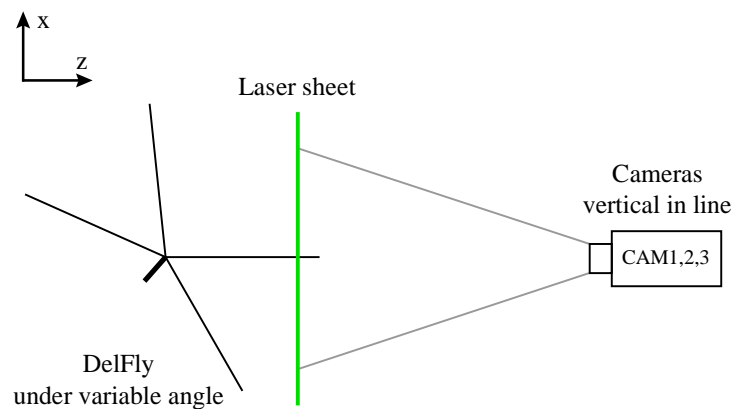


Figure 5.2. Top view of the experimental set-up with the cameras placed vertical, where the illumination by the laser is from below, hence perpendicular to the figure plane

Results from the previous research showed the flow field around the biplane wing configuration to be symmetrical. This implied that for the current research, the PIV measurements could be limited to the flow field around only one of the wings. The DelFly model is rotated in discrete steps of ten degrees, such that the upper wing leading edge remains perpendicular to the laser sheet. The current research studies vortex development and wing shape. With this set-up the leading edge vortex development is visible without any optical blockage from the wing itself.

Since reflections were a large problem during the previous research the phase-locked measurements yielded better results than the time resolved measurements. Phase-locked images can be post processed better and for the flow field an average can be taken to partially cancel the effect of spurious velocity vectors caused by reflections. So for the current research the choice is made to perform the measurements only in a phase-locked manner. Another advantage of phase-locked measurements is that it does not longer require the high speed PIV system. The low speed PIV system uses a laser with a higher energy level per pulse. This gives better illuminated images, so particle visibility increases and peak-locking (see paragraph 4.1) reduces.

5.2 The experimental campaigns

For the present research a new experimental set-up was built. This set-up is designed such that a full-scale DelFly can be fixed to the construction and with relative ease can be exchanged with another model. The set-up has two perpendicularly placed force sensors to measure forces both in the thrust and normal direction, making the set-up also suited for forward flight measurements. For the hovering set-up it is sufficient to only consider the force in thrust direction. The in-flight orientation for a hovering DelFly is vertical; hence the model is also placed vertically in the set-up. For hovering flight, the upward force is equal to the thrust generated by flapping, which is also the lift that is produced.

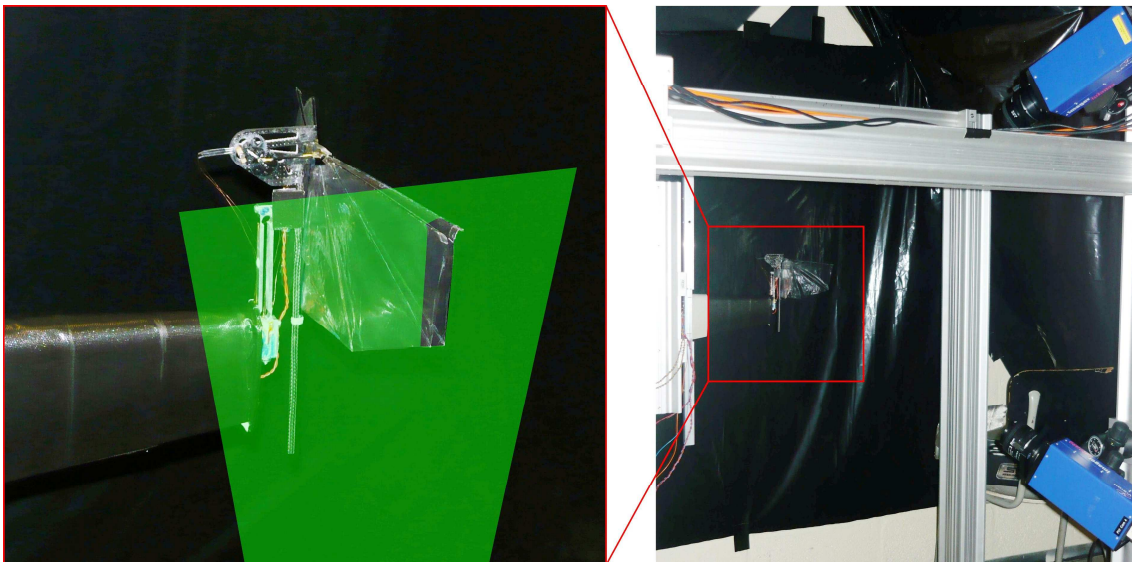


Figure 5.3. The experimental set-up with highlighted the tailless DelFly II model showing the orientation of the laser plane (third camera not visible)

The experiments are conducted in two campaigns. In the first campaign a tailless DelFly II model with the original DelFly II wing is mounted on the set-up. The set-up is placed in an enclosed space which can be filled with seeding. The laser illuminates the model from below

and the region of interest is imaged by three cameras, see figure 5.3. A third camera is added to the stereoscopic PIV system to have some redundancy to cope with areas where reflections obscure the particles. Using the three camera set-up, three 2-dimensional flow fields can be calculated, with the velocity components in the measurement plane. Using a stereoscopic PIV configuration between different camera pairs, in addition three flow fields can be calculated with an out-of-plane velocity component.

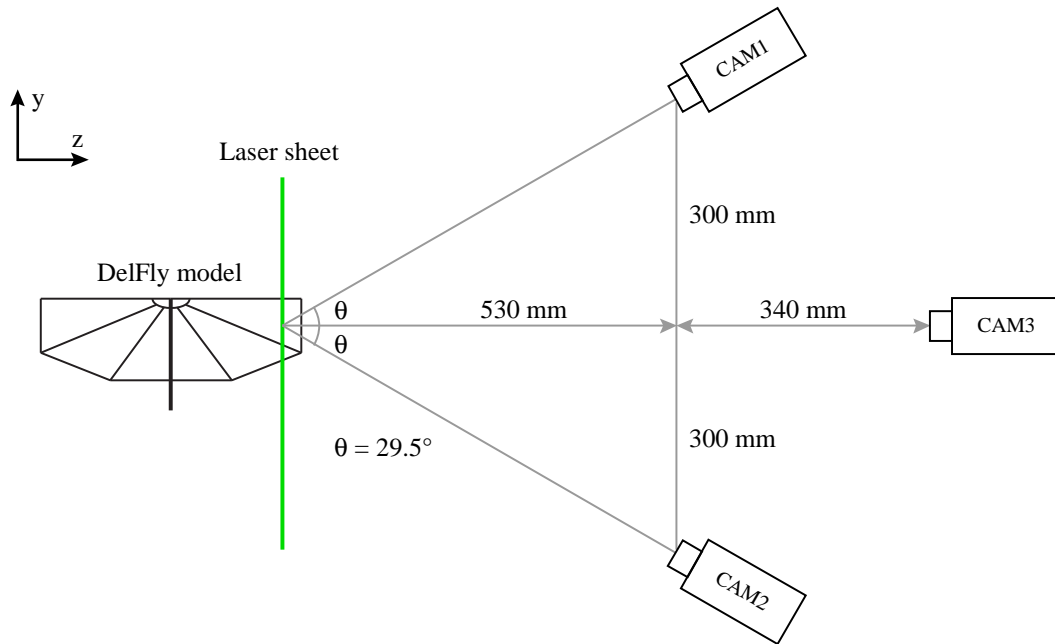


Figure 5.4. Front view of the camera set-up during first experimental campaign, where the illumination by the laser is from below, hence from the bottom of the figure

The angles between the cameras are 29.5 degree, see figure 5.4. According to research of Lawson^[40] on an approximately similar PIV set-up, the ideal angle between cameras for stereoscopic PIV lies between 40 and 60 degrees. So using stereoscopic PIV between camera 1 and camera 2 will satisfy this criterion, while using camera 3 in the stereoscopic PIV will result in an increase in the root-mean-square-error for the out-of-plane velocity component to 5% for small particle displacements, which for the current research is still acceptable since no exact quantification of the out-of-plane velocity component is sought.

During this first campaign 50 phase-locked images are taken at each phase. The flap cycle is sampled at intervals of 4% of the complete flap cycle. The flapping frequency is initially chosen to be 13 Hz, which corresponds to the flapping frequency of a hovering DelFly. However during the measurements the model could no longer support this frequency due to wear. Most of the measurements are therefore performed at a reduced frequency of 11 Hz. The measurements are performed at five spanwise positions between 60 mm measured from the root of the wing and the wing tip, which is at 140 mm from the root of the wing. Measurements done closer to the root suffered from large reflections, since a larger area of the wing is illuminated by the laser. The influence of frequency and span is investigated at a limited number of positions during flap cycle. The complete test matrix can be found in table 5.1.

Table 5.1. Test matrix for the first experimental campaign

Wing	Flapping frequency	Spanwise distance from root	Number of measurements
Original wing	13 Hz	100 mm	10
Original wing	11 Hz	140 mm	15
Original wing	11 Hz	120 mm	26
Original wing	11 Hz	100 mm	26
Original wing	11 Hz	80 mm	2
Original wing	11 Hz	60 mm	1
Original wing	9 Hz	100 mm	14

For the second experimental campaign again a tailless DelFly II model is used, this time equipped with the improved DelFly II wing, which has been described in paragraph 3.3. To further investigate the effect of the Reynolds number, also a series of measurements was conducted on a high aspect ratio wing, which has a smaller chord length. Measurements are conducted in the same way as done in the first campaign. Additional measurements are performed with the DelFly model placed with the leading edge down to have unobstructed illumination of the flow around the leading edge. Study of flow field and force production showed this to have no effect, since inertial accelerations during flapping are of higher order than the gravitational acceleration. A preliminary study of the results from the first campaign showed that the middle camera yields little extra information, so this camera was omitted in the second campaign. The angle θ has been reduced to 19.7 degrees such that it just meets the minimum criterion^[40], see figure 5.5. With this set-up two 2-dimensional flow fields and, using both cameras in a stereoscopic configuration, all three velocity components in the measurement plane can be determined. At every phase again 50 phase-locked images are taken. The flapping frequency is varied from 9 Hz to 13 Hz and the spanwise position of the measurement plane is again varied from 60 mm to 140 mm, as can be seen in the test matrix in table 5.2. Based on the analysis of the preliminary results from the first campaign, the number of phase-locked positions during the flap cycle has been increased. During the translational phase of the flap cycle measurements are now performed at intervals of 2% of the flap cycle.

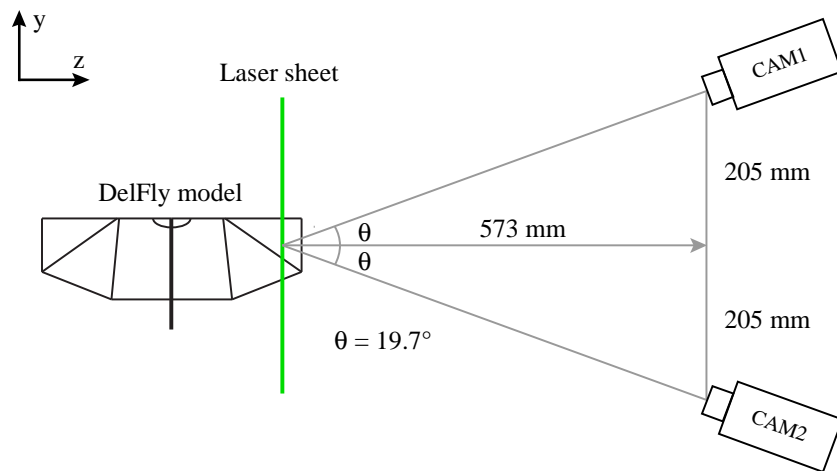


Figure 5.5. Front view of the camera set-up during second experimental campaign, where the illumination by the laser is from below, hence from the bottom of the figure

Table 5.2. Test matrix for the second experimental campaign

Wing	Flapping frequency	Spanwise distance from root	Number of measurements
Improved wing	13 Hz	140 mm	37
Improved wing	13 Hz	120 mm	37
Improved wing	13 Hz	100 mm	37
Improved wing	13 Hz	80 mm	8
Improved wing	13 Hz	60 mm	8
Improved wing	11 Hz	120 mm	37
Improved wing	11 Hz	100 mm	37
Improved wing	9 Hz	100 mm	37
High AR wing	13 Hz	140 mm	8
High AR wing	13 Hz	120 mm	8
High AR wing	13 Hz	100 mm	37
High AR wing	13 Hz	80 mm	8
High AR wing	13 Hz	60 mm	8
High AR wing	11 Hz	100 mm	37

5.3 Force measurements and DelFly control

For the force measurements and DelFly control, a custom made micro controller board has been used. The micro controller board is used to guarantee a high and constant sampling frequency and is connected to a PC with a serial connection. The controller board has a PID-controller which operates the DelFly motor controller and controls the wing flapping frequency. The flapping frequency is measured by counting the motor pulses. Every motor revolution requires three motor pulses and given a gear ratio of 1:20 a total of 60 pulses per flap cycle are recorded. The DelFly model is also equipped with a Hall sensor which gives a pulse once every flap cycle to compensate for drift. These measurements are also used by the controller board to generate a triggering pulse for the PIV system. For the phase-locked measurement, triggering needs to be done every time the wing is at the same position in the flap cycle. Since wing flapping frequency varies by 10% during each flap cycle, the motor pulses are used to provide an accurate measurement of the wing position. The maximum measurement frequency of the PIV system is approximately 4 Hz, so the PIV system is triggered once every four flap cycles to be able to do measurements at a flapping frequency up to 16 Hz.

Zemic load cells are used to measure the forces on the DelFly model. The sensors are of the type Q70x5x9-H with a capacity of 200 gf (=1.96 N) and use strain gauges as sensing element. The sensors are connected to a PICAS amplifier system from Peekel Instruments. This high accuracy measurement system amplifies the measurement signal by approximately a factor of 2000. The PICAS analog output provides the controller board with a -5 V to 5 V signal for a measured range of -0.981 N to 0.981 N. The controller board has a 10 bit A/D-converter which brings the measurement resolution to 1.92 mN. The same controller board also measures the DelFly motor supply voltage and current provided by a separate power supply. This makes it possible to determine the power consumption of the DelFly. All measurements are carried out with a sampling frequency of 1860 Hz. Measurements are recorded in log-files and send to a PC for data analysis.

To obtain a reliable description of the phase-averaged flow, the measurements were performed over a time period of 10 seconds. Since the experiments are carried out at flapping frequencies ranging from 9 Hz to 13 Hz, the data acquisition period includes 90 to 130 flap cycles. The data collected over this period has been averaged per flap phase, to find the statistical mean. To determine the statistical uncertainty of this mean value, the standard deviation or root-mean-square belonging to the average value is calculated using the following equation:

$$\sigma = \sqrt{\frac{1}{n-1} \sum_{i=1}^n (x_i - \bar{x})^2} \quad (5.1)$$

Where \bar{x} is the mean value over n data points. The standard deviation is a measure for the variety of the data. Investigations of the thrust data have shown this data to be distributed normally. This implies 68% of the data points have a value within once the standard deviation from the mean value and 95% have a value within twice the standard deviation from the mean value. The results from the force measurements are discussed in paragraph 6.3.

5.4 PIV instrumentation

During the PIV experiments specific instrumentation is used. A seeding generator is used to distribute the tracer particles in the air. A laser is used to illuminate the particles. Cameras are used to take the images, which are processed by dedicated software. In this paragraph the equipment used for the PIV experiments is described.

5.4.1 Seeding generator

The particles used for the PIV experiment are generated by a SAFEX fog generator. The fog generator produces a non-toxic water based fog from a fluid named SAFEX normal power mix. The fog droplets have a mean diameter of 1 μm .

5.4.2 Laser

The laser used as light source for the experiments is the Quantel Twins CFR-400. The laser system is a double pulsed Nd:YAG laser. The laser produces infrared light at a wavelength of 1064 nm. A harmonic generator halves the wavelength to 532 nm, which is green light in the visible spectrum. The maximum power is 200 mJ per pulse and the pulse duration is 7 ns. The maximum repetition rate of the two pulses is 30 Hz, however the camera data transfer limits the overall data acquisition rate to 4 Hz.

5.4.3 Cameras

For the first experimental campaign three cameras have been used. The top and bottom cameras in the experimental set-up, described in paragraph 5.2, are LaVision Imager Intense CCD cameras. The middle camera is a PCO SensiCam QE CCD camera. For the second experimental campaign the middle camera has been omitted.

The LaVision Imager Intense is a high dynamic 12bit cooled CCD camera with a progressive scan sensor. The CCD chip has a resolution of 1376 x 1040 pixels with a pixel size of 6.45 μm x 6.45 μm , the total size of the CCD chip is 8.9 mm x 6.7 mm. The camera has a double shutter feature, with an interframe time of minimal 500ns to enable PIV measurements. The image rate is 10 frames per second, so when operated in double shutter mode the measurement frequency is

limited to 5 Hz. Both the top and bottom camera are equipped with a lens with a focal length of 35 mm and a daylight filter. The cameras are connected to PCI-Boards mounted in a PC via a serial interface. For one camera a double-coaxial cable is used and for the other camera a fiber optic cable.

The PCO SensiCam QE is a similar 12 bit cooled CCD camera. The CCD chip has a resolution of 1280 x 1024 pixels with a pixel size of 6.7 μm x 6.7 μm , the total size of the CCD chip is 8.6 mm x 6.9 mm. This camera has also a double shutter feature. The image rate is 8 frames per second. The maximum data acquisition rate is automatically limited by the software based on the maximum image rate of all cameras, so for both experimental campaigns the measurement frequency is limited to approximately 4 Hz. The camera is equipped with a lens with a focal length of 50 mm and a daylight filter. The camera is connected to a PCI-Board via a fiber optic cable.

5.4.4 PTU

The simultaneous triggering of the laser and cameras is controlled by the Programmable Timing Unit (PTU) Version 9 of LaVision. The PTU is mounted in a PC and connected to the PCI boards of the cameras and the triggering cable of the laser. The PTU receives an external trigger from the DelFly controller board and, taking into account the various time delays, sends a triggering signal to the laser and cameras. The PTU is controlled by the software DaVis 7.2 of LaVision.

5.4.5 Software

All aspects of particle illumination, image recording and image post processing were performed with the software DaVis 7.2 of LaVision. The program makes it possible to control various settings like laser power and the separation time between two subsequent images. The post processing function uses correlation to calculate the velocity field from the stereo PIV images. Velocity field data is exported to MATLAB (The MathWorks, inc.) for creating velocity plots and further post processing.

5.5 PIV settings

In this paragraph the camera settings and laser settings are described, as well as the image post processing.

5.5.1 Camera and laser settings

The research focus is on the study of vortex development and wing deformation. So the field of view should include the full cord length of the wing and some extra space to see the vortices at the trailing and leading edge. Taking into account the fact that the largest wing chord is 88 mm, the field of view for the experiments is set to 110 mm x 145 mm. The cameras are positioned such that the highest resolution is in vertical direction, so along the chord.

The particle image size should be about 2 pixels to avoid peak-locking, the tendency to round off the measured velocity in discrete steps, see paragraph 4.1. Since the particles are geometrically small, the effective image size is largely determined by the diffraction effect. The effective particle image size, d_{eff} , is determined by:

$$d_{eff} = \sqrt{M \cdot d_p^2 + d_{diff}^2} \quad (5.2)$$

Where d_p is the mean particle diameter of 1 μm , d_{diff} the particle image size due to the diffraction effect and M the magnification, defined as the image size divided by the object size. Based on a vertical resolution of 1376 pixels with a pixel size of 6.45 μm , the magnification is:

$$M = \frac{1376 \cdot 6.45 \cdot 10^{-6} \text{ m}}{145 \cdot 10^{-3} \text{ m}} = 0.061 \quad (5.3)$$

Using equation 5.2, the necessary d_{diff} for an effective particle size of 12.9 μm (2 pixels) is calculated to be 12.9 μm . The equation for diffraction size^[39] is:

$$d_{diff} = 2.44 \cdot \lambda \cdot f_{\#} \cdot (1 + M) \quad (5.4)$$

Where λ is the wavelength of the laser and $f_{\#}$, the camera aperture number. From equation 5.4 it can be seen that the particle image size can be controlled by setting the camera aperture number. The necessary aperture number, defined as the ratio between focal length and aperture diameter, for an effective image size of 2 pixels can be calculated using equation 5.4 to be 9.4.

During the experiments the $f_{\#}$ of 9.4 has been used as an indicative value for the camera setting. The actual aperture setting is a compromise between good particle visibility and low wing reflection intensity. The experimental set-up has cameras looking at the wing from above, from the side and from below, while the laser illuminates from below. Light scatters from the particles primarily in forward direction, secondary in backward direction and even less in sideward direction, see figure 4.2. The particle visibility can be increased by opening the camera diaphragm or by increasing the laser output power. Increasing the laser output power to high levels, however, could also damage the cameras when hit by direct reflections from the wing. The final camera settings used for the experiments can be found in table 5.3.

Table 5.3. PIV settings

	camera 1	camera 2	camera 3	
Camera settings	CCD resolution (pixels)	1376 x 1040	1376 x 1040	1280 x 1024
	pixel size	6.45 μm	6.45 μm	6.7 μm
	field of view	145 x 110 mm^2	145 x 110 mm^2	145 x 110 mm^2
	magnification, M	0.061	0.061	0.057
	lens focal length	35 mm	35 mm	50 mm
	aperture number, $f_{\#}$	11	8	5.6
Laser settings	pulse duration		7 ns	
	pulse separation, dt		250 μs	
	wave length, λ		532 nm	
	laser sheet thickness		2.5 mm \pm 0.5 mm	
Post processing	interrogation window		32 x 32 pixels	
	overlap		50%	
	number of images		50	

To have good correlation during the post processing of the images it is important that the majority of the particles are in the same interrogation window at both images. This can be done by setting the time separation between two exposures not too large. On the other hand, the time separation should be set large enough to obtain a large enough dynamic range in the displacement in order to be able to capture slowly moving fluid features. For the maximum separation time the in-plane particle displacement is advised to be no more than $\frac{1}{4}$ of the interrogation window^[39]. Furthermore, the out-of-plane particle displacement should be less than $\frac{1}{4}$ of the laser sheet thickness. The laser sheet thickness, used for the experiments, is 2.5 mm. Using previous research and preliminary results as a reference the maximum in-plane velocity is 5.0 m/s and the maximum out-of-plane velocity is 2.5 m/s. The separation time is set to be 250 μ s. For these velocities and time separation, the maximum particle displacement becomes:

$$\text{In-plane: } d_{\max, \text{in-plane}} = V_{\max, \text{in-plane}} \cdot dt \cdot M = 5.0 \cdot 250 \cdot 10^{-6} \cdot 0.061 = 11.8 \text{ pixels}$$

$$\text{Out-of-plane: } d_{\max, \text{out-of-plane}} = V_{\max, \text{out-of-plane}} \cdot dt = 2.5 \cdot 250 \cdot 10^{-6} = 0.625 \text{ mm}$$

With this setting, the maximum out-of-plane displacement meets the displacement criterion, since it is $\frac{1}{4}$ of the laser sheet thickness. The interrogation window used to have a good correlation for the in-plane displacement is described in the section 5.5.2.

5.5.2 Image post processing

For every measurement 50 image pairs are taken per camera. These raw images are first pre-processed before correlation. To remove the static background the minimum intensity image of the whole measurement set is subtracted from every image individually. This removes the part of the image present in all images. Furthermore the images are normalized by dividing them by the average intensity image to remove the reflections from the wing. A comparison between a raw image and pre-processed image, in figure 5.6, shows that the most prominent reflections have been removed, while particle visibility has been improved.

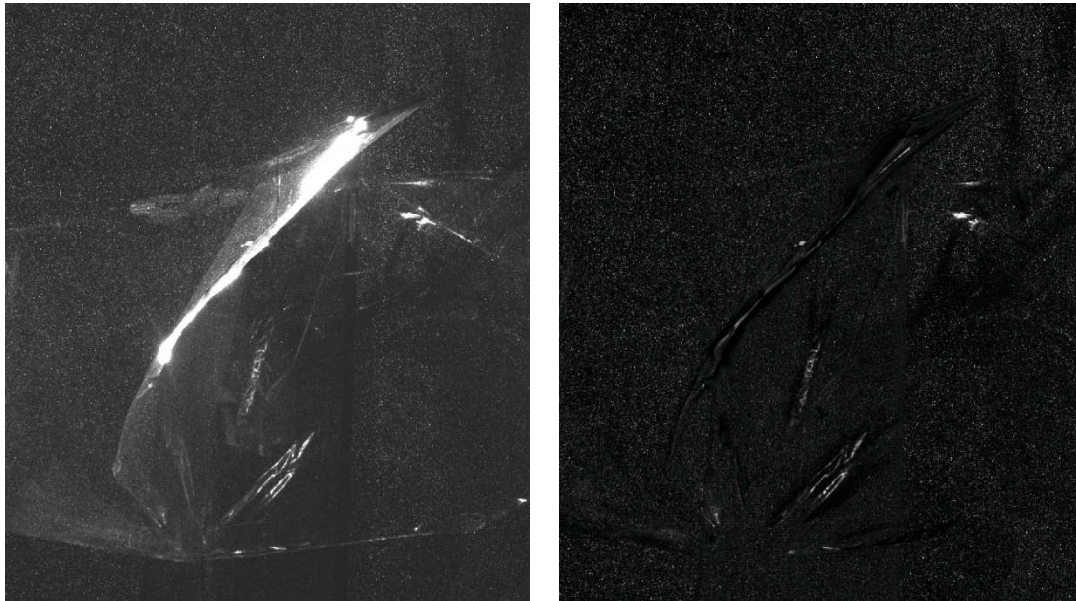


Figure 5.6. Result from image pre-processing by extracting minimum intensity and normalization: Raw image (left), Pre-processed image (right)

In order to compensate for the camera viewing angle with respect to the measurement plane the camera images have been calibrated with the use of a calibration plate and by using self-calibration, see paragraph 4.2. For the self-calibration images have been taken without the DelFly model installed, so only tracer particles are shown. Images from two cameras, taken at the same moment are correlated. This allows the software to use window shift and window deformation to exactly align the images of both cameras, which is necessary for successful stereoscopic PIV. When using the experimental set-up with three cameras, the stereoscopic calibration has to be performed for each of the three possible camera pairs.

The pre-processed and corrected images are subsequently correlated to extract the velocity field. The images are correlated using a multi-pass function. The interrogation window for the first pass is 128 x 128 pixels with an overlap of 50%. The velocity vector found in this pass is used as a reference for the next pass. The integration window size is reduced from 128 x 128 pixels to 64 x 64 pixels to 32 x 32 pixels in the subsequent passes. A median filter is used to remove spurious vectors.

The instantaneous velocity field found for every image pair is a combination of a cyclic flow component and additional random unsteady flow features. Cyclic flow indicates that unsteady flow features, like moving vortices, are present at the same location for each phase-locked measurement. To extract the cyclic flow, the average velocity field of each set of phase-locked measurements is calculated. When more instantaneous velocity fields are included in the calculation for the average velocity field, the measurement error reduces. As the ambition was to investigate the vortex development for many varying parameters (such as phase angle, spanwise position, flapping frequency etc.), the quantity of the number of measurements was considered more important than the error reduction for each measurement. Visual inspection of the flow field revealed that including more than 25 instantaneous velocity fields for the calculation of an average velocity field resulted in little improvement. To have some redundancy, the final velocity field used for the results in the next chapter is formed from an average of 50 instantaneous velocity fields.

The statistical uncertainty is determined by the calculation of the standard deviation, again calculated by equation 5.1. Investigations of the results show the standard deviation to be approximately 0.1 m/s (10% of the average velocity) on most locations within the flow field. The standard deviation on locations where the flow shows vortices is significantly larger, up to 2 m/s, which is of the same order as the vortex velocities. This shows that the flow at vortex locations varies due to random fluctuations and due to the fact that the vortices, although present during each phase-lock measurement, still vary slightly in shape, in size and in exact location.

Chapter 6

Results

In chapter 5 the experimental campaigns conducted on the flapping MAV, DelFly II, have been described. The experiments were performed on three different wing sets, in two subsequent measurement campaigns. In this chapter the results of the experiments will be discussed.

In the first introductory paragraph the geometry of the three different wings is described. To get an impression of the DelFly wing motion, the PIV experiments are also used to visualize the in-flight wing deformation. In paragraph 6.2 the wing deformation for both the original wing and the improved wing is shown. Force measurements were carried out simultaneously with the PIV measurements. The results from the force measurements are discussed in paragraph 6.3. Finally in paragraph 6.4 the results from the PIV measurements are discussed. The instantaneous flow field during hovering is shown at various phases of the flap cycle, where the focus is especially on vortex generation and development.

6.1 Introduction

The experiments on the DelFly set-up were performed in two campaigns. In the first campaign experiments were carried out on the original DelFly wing and in the second campaign the improved DelFly wing and a high aspect ratio version of the improved DelFly wing were used. The layout of the three wings is shown in figure 6.1.

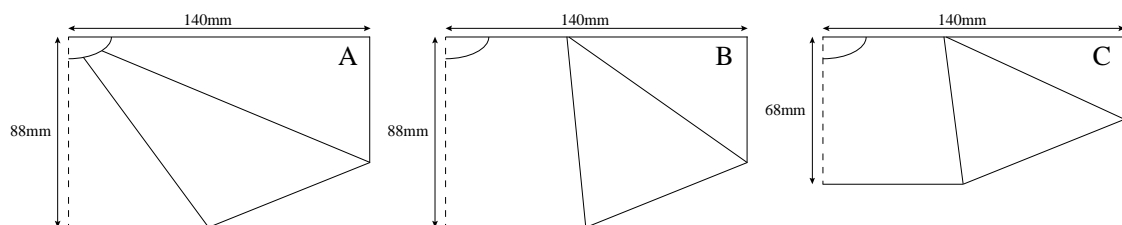


Figure 6.1. The wing layout for: the original DelFly wing (A), the improved DelFly wing (B) and the high aspect ratio wing (C)

The improved wing has the same wing shape and dimensions as the original DelFly II wing, with both having a mean chord length of 80 mm and a semi wing area of 112 cm². The

difference between the original and improved wing is in the location and orientation of the two carbon stiffeners. For the improved wing the stiffeners are placed more out-board and come together at the leading edge. The high aspect ratio wing has a similar stiffener orientation as the improved wing, but a 20 mm shorter chord length over the whole span, which gives it a mean chord length of 60 mm. The aspect ratio is increased with 33% from 3.5 for the improved wing to 4.7 for the high aspect ratio wing and the semi wing area is decreased with 25% to 84 cm².

The PIV measurements were performed in a plane perpendicular to the leading edge at five locations along the span. In terms of the semi span, R , these are, measured from the wing root, at 60 mm ($0.43R$), at 80 mm ($0.57R$), at 100 mm ($0.71R$), at 120 mm ($0.86R$) and at the wing tip at 140 mm (R), see figure 6.2. Furthermore, measurements were performed at three flapping frequencies; 9 Hz, 11 Hz and 13 Hz. The measurements were performed during the complete flap cycle, where the phase is indicated with the dimensionless time $\tau = t/T$, where T is the period of the flap cycle.

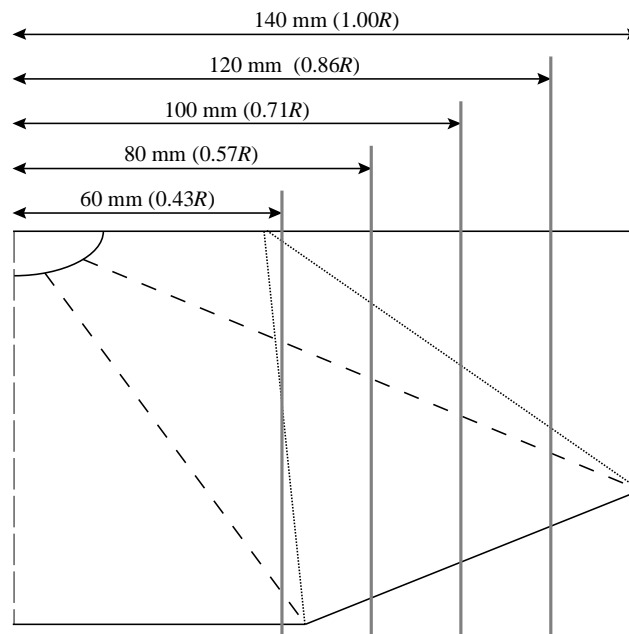


Figure 6.2. The spanwise cross-sections of the measurement plane with the DelFly wing. Dashed lines represent the stiffeners in the original configuration and dotted lines the stiffeners in the improved configuration

6.2 In-flight wing shape

The wings described in the previous paragraph are made from Mylar foil with carbon stiffeners and a D-shaped carbon rod for the leading edge. The in-flight wing shape is determined by aerodynamic, elastic and inertial forces. The aerodynamic forces are in turn influenced by the wing shape, leading to a complex fluid-structure interaction. Determination of the in-flight wing shape is important to help explain aerodynamic effects. They can also be used as input for numerical flow simulations of flapping flight or as a benchmark for future full fluid-structure interaction simulations.

The in-flight wing shape is extracted from the images taken with the PIV cameras. Using the PIV set-up at low laser intensity without seeding, a cross-section of the wing is illuminated. In figure 6.3 the wing shape of the original DelFly wing at various moments during the flap cycle is shown as function of the non-dimensional time, τ . The cross-sections are taken at spanwise location, $b = 0.71R$ and at a wing flapping frequency of 11 Hz. The cross-sections in figure 6.3 show the foil folded over the D-shaped leading edge carbon rod. The orientation of the carbon rod gives rigidity in the stroke direction but allows the leading edge to bend up and down (in chordwise direction) more easily. This enables the wing to show a heaving motion during flapping, shown by the leading edge path in figure 6.3. Experience from tests with various leading edges has shown this to have a positive effect on the thrust generation.

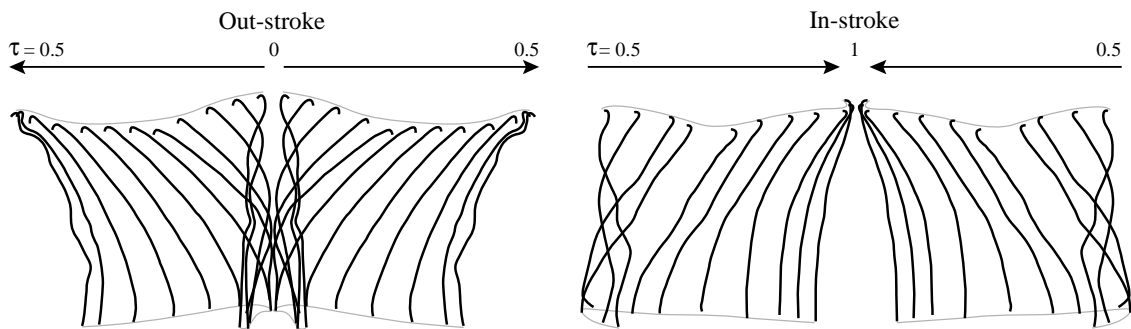


Figure 6.3. Cross-sections of the original wing during a flap cycle at a flapping frequency of 11 Hz at a spanwise location of $0.71R$. Loaded with an average thrust of 0.15 N

Another feature shown in figure 6.3 is the clap-and-peel, as described in paragraphs 2.5 and 2.6. During the out-stroke, from $\tau = 0$ to $\tau = 0.30$, while the leading edges move apart, the upper and lower wing surfaces peel apart and at the trailing edge the wing foil claps together. Since the leading edges are the part of the wing being driven by the flapping mechanism, the wing motion can be seen as a forced displacement of the leading edge where the rest of the wing is being dragged behind, like a flag being waved, hence, illustrating the large impact of the wing flexibility.

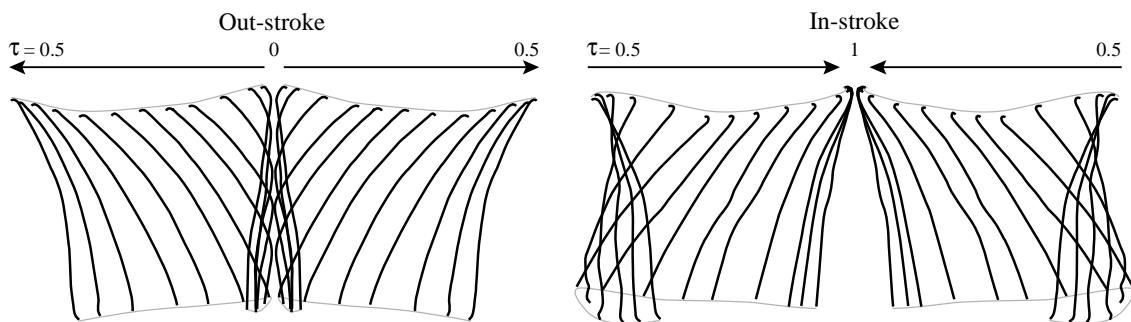


Figure 6.4. Cross-sections of the improved wing during a flap cycle at a flapping frequency of 11 Hz at a spanwise location of $0.71R$. Loaded with an average thrust of 0.14 N

While comparing the in-flight wing shape of the original wing with that of the improved wing, see figure 6.4, it can be seen that the original DelFly wing is more flexible during the rotation ($\tau = 0.5$ to 0.6) than the improved wing. The stiffeners on the improved wing are placed more out-board compared to the stiffeners on the original wing. This gives the improved wing more rigidity at locations near the wing tips. The more flexible behaviour of the wing during rotation could also be due to a difference in foil tension, caused by differences in the mounting of the wings to the DelFly body. The wing shape of both wings during the translation (both in-stroke as out-stroke) is comparable.

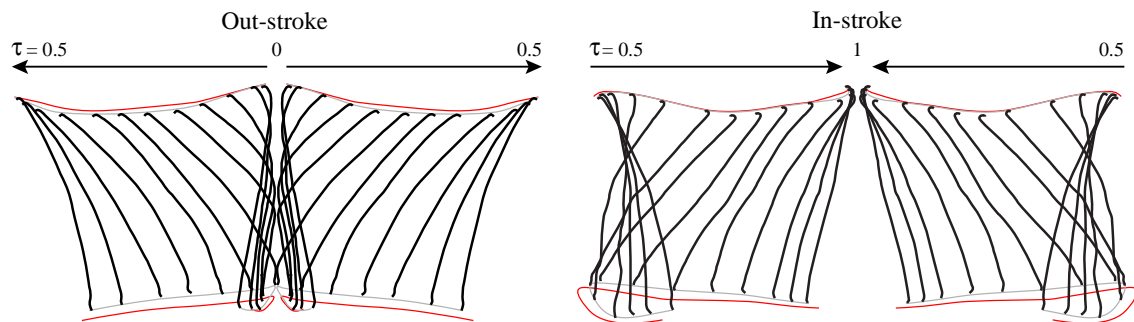


Figure 6.5. Cross-sections of the improved wing during a flap cycle at a flapping frequency of 13 Hz at a spanwise location of $0.71R$. Loaded with an average thrust of 0.17 N. The red lines represent the leading edge and trailing edge paths for a flapping frequency of 11 Hz

Investigations of the wing shape of the improved wing at a flapping frequency of 13 Hz show increased wing deformation, see figure 6.5. At higher flapping frequency the wing shows an increased heaving motion and increased ‘flagging’. This results in a smaller geometric angle of attack and increased chambering during translation, where is noticed that the trailing edge path has moved up for the higher flapping frequency.

6.3 Force measurements on the hovering DelFly

During the PIV measurements, simultaneous force measurements were performed. Using perpendicular placed force sensors the force in thrust direction and in normal direction were measured. For the hovering set-up the thrust is defined as the upward force along the DelFly body and the normal force is the force perpendicular to the body in the symmetry plane of the DelFly. During the measurements a micro controller was used to keep the flapping frequency constant. For the force measurements a period of 10 seconds is considered from the moment a steady state has been reached for the flapping frequency. The measurements are carried out at a sampling frequency of 1860 Hz, which provides the opportunity to examine the average force as well as the force variation over a flap cycle. A detailed description of the experimental set-up, which was also used during the research of Bruggeman^[2], can be found in chapter 5.

6.3.1 Average force generation

For hovering flight it is expected that the resulting force is directed along the DelFly body, i.e. in thrust direction, due to the symmetric placement of the flapping wings. Measurements of the force in normal direction show that the average force at a flapping frequency of 11Hz is just 1.2 mN. This means the force in normal direction is less than 1% of the average force in thrust

direction, which is typically 0.1-0.2 N (see figure 6.6). Together with the result that the standard deviation of the measurement in normal direction is 3.1 mN, which is of the same order of the measurement resolution (1.95 mN), the force in normal direction is assumed essentially zero. For the remainder of the chapter therefore only the thrust will be considered.

Flapping flight produces periodically varying forces. For the DelFly to stay airborne during hovering the net thrust should be large enough to counter its weight, which is approximately 0.17 N for an average model. To determine the net thrust production, the average thrust per flap cycle is calculated. In general it can be said that the average thrust production per cycle is very constant for a constant flapping frequency. The standard deviation is of the order of 1.5 mN, while the standard deviation for the average flapping frequency is of the order of 0.04 Hz.

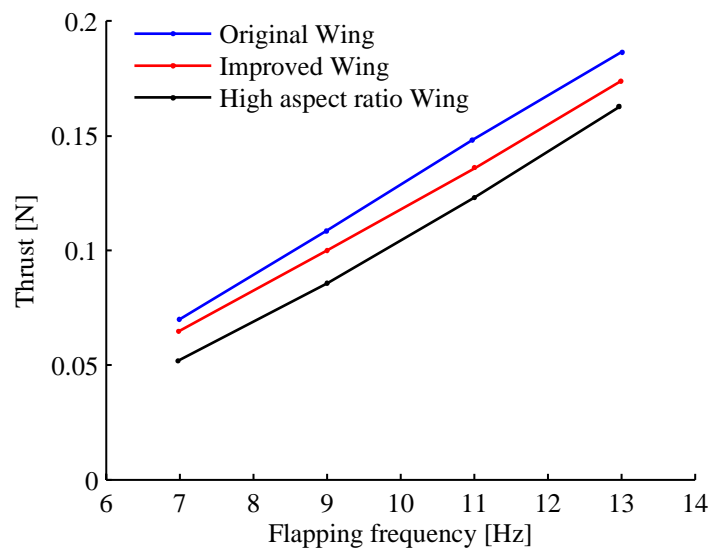


Figure 6.6. Average thrust per flap cycle for the measured wings

In figure 6.6 the average thrust per flapping cycle is plotted versus flapping frequency. It can be seen that the thrust shows a linear increase with flapping frequency. This is the case for all tested wings. The high aspect ratio wing shows a 17% thrust reduction at a flapping frequency of 11 Hz compared to the original wing. The improved wing shows an 8.2% lower thrust compared to the original wing at a flapping frequency of 11 Hz. This seems inconsistent with the research of Bruggeman^[2], conducted in order to find an improved wing, see paragraph 3.3. Results from the research of Bruggeman and from extra thrust measurements performed at a later stage suggested the original and improved wing to have approximately the same thrust production, at the level of the original wing in figure 6.6. It is therefore assumed that the thrust generation for both wings is approximately equal because the driving parameters (wing area, flapping frequency and stroke angle) are kept constant. The cause of the fact that the results of measurements performed on the same wing can vary is because the DelFly is handmade, which makes it difficult to reproduce wing properties exactly. There are small variations in wing construction, wing mounting on the body and different levels of degradation of the wings and driving mechanism. After few hours of operation, the DelFly wings loose elasticity, this may cause a thrust reduction of about 5%. The influence of foil tension on thrust and power consumption is also significant. Measurements performed at a later stage show a 5% thrust reduction for wings at high foil tension due to differences in wing mounting. However, foil tension has not been measured during the tests described in this paragraph. Altogether these differences could easily add up to a relative large variation in thrust measurements, even when

performed on the same wing types. This therefore could account for the difference of 8.2% in thrust production, found between the original and improved wing in the current research.

The driving parameter for the wing performance research, as performed by Bruggeman, was the ratio of the thrust and power consumption (thrust-to-power ratio). It was found that, although the improved wing shows a comparable thrust generation, the improved wing does show a significant reduction in power consumption. Even for a given required thrust the improved wing has a smaller power consumption than the original wing does. In figure 6.7 the thrust-to-power ratio is plotted versus the flapping frequency. It can be seen that for these measurements the improved wing has a 30% increase in thrust-to-power ratio. This is significantly more than the 5% increase in thrust-to-power ratio found by Bruggeman and is due to an extreme lower power consumption of the improved wing, related to the lower thrust generation. In figure 6.7 it can also be seen that the high aspect ratio wing has slightly lower thrust-to-power ratio than the improved wing. A result shared by the research of Bruggeman.

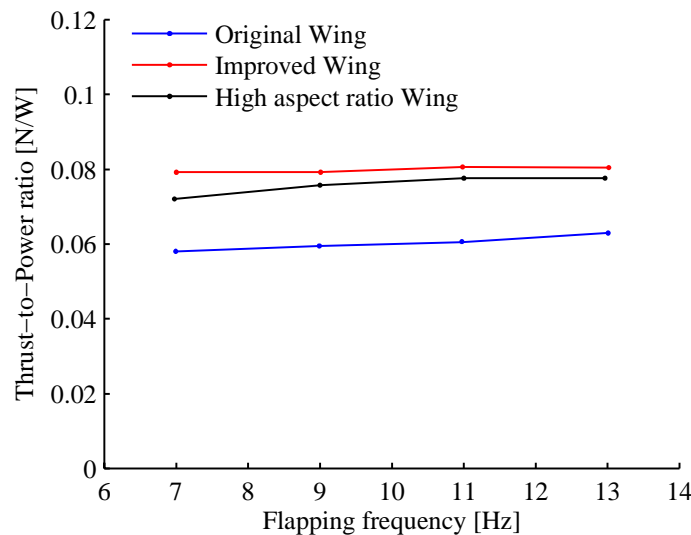


Figure 6.7. Thrust-to-Power ratio for the measured wings

6.3.2 Force generation during one flap cycle

To relate thrust and power consumption to the instantaneous flow field, examined by the PIV measurements, their development during a flap cycle should be studied. Unfortunately the thrust measurements suffered from severe mechanical resonance in the force measurement system. The high accuracy force sensors act as a relatively soft spring. Together with the DelFly model the natural frequency of the whole system lies within the measurement range. The severe resonance make it impossible to examine the thrust generation from the raw measurement data, since the thrust generation due to aerodynamic effects is obstructed by high frequency, high amplitude force fluctuations.

To be able to make an assessment about which force fluctuations are contributed to aerodynamic effects and which are due to mechanical resonance, extra measurements were performed under near-vacuum condition (60 to 70 Pa) to exclude the effect of the aerodynamic forces. For these experiments the DelFly set-up was mounted in the test section of the HTFD wind tunnel at the high speed lab of TU Delft. To compare the measurements in vacuum and air the frequency spectra are studied. The frequency spectra of the thrust measurements of the original wing at 12 Hz in air and vacuum are plotted in figure 6.8.

From the vacuum tests it became obvious that besides the DelFly model and sensors, the complete construction as well as the mass of the surrounding air contributes to the resonance. Because of the complex nature and high amplitude of the vibrations it is not possible to extract the specific vibrations caused by the resonance. Only the first two modes of force oscillations (twice the forcing frequency) can be ascribed with certainty to aerodynamic forces, as is illustrated by the peaks at 12 Hz and 24 Hz in figure 6.8.

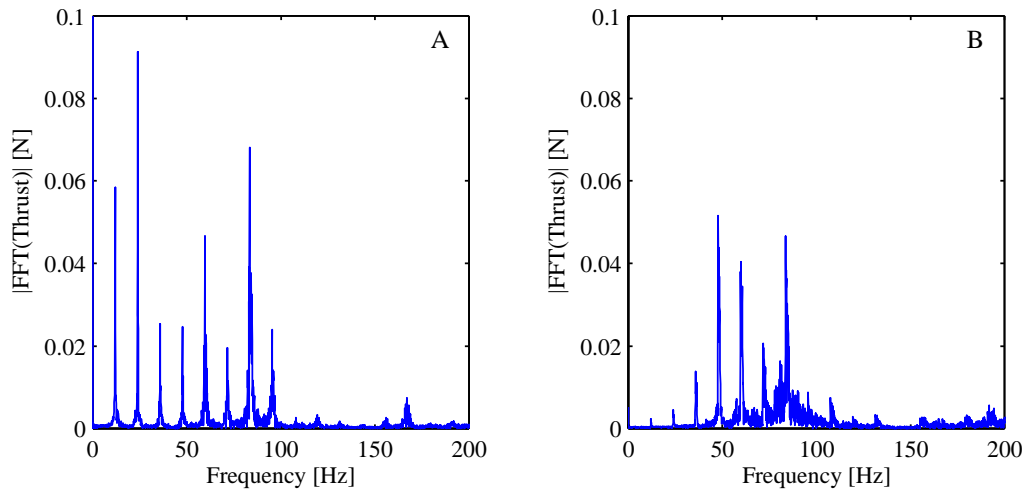


Figure 6.8. Frequency spectra (based on Fast Fourier Transforms) of the thrust measurements for the original wing at 12 Hz in air (A) and in vacuum conditions (B)

To eliminate the high frequency resonance, a low pass filter has been constructed. The passive low pass filter, based on a Fourier transformation, has a cut-off frequency of twice the forcing frequency. A disadvantage of using this filter is that all aerodynamically related thrust fluctuations with a small characteristic time are also filtered out.

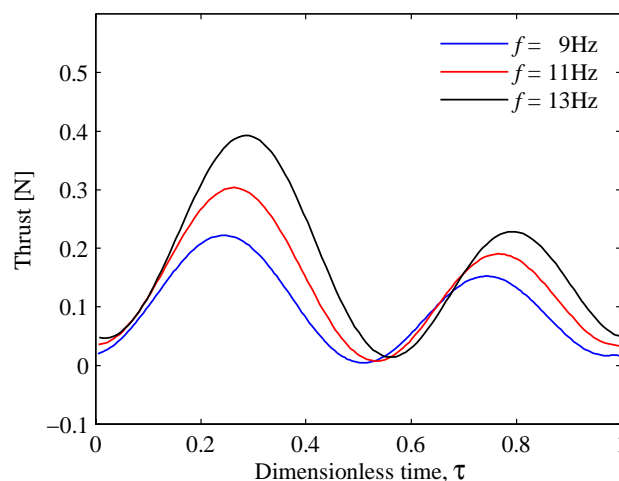


Figure 6.9. Average filtered thrust generated by the improved wing during one flap cycle for various frequencies

In figure 6.9 the average filtered thrust for one flap cycle is shown for the improved wing at various frequencies. It can be seen that the thrust has two peaks during the translation. The thrust peak during the out-stroke is higher than the one for the in-stroke. This is due to the clap-and-peel effect which takes place during the first 30% of the flap cycle, as is shown in figure 6.3. These results correspond to findings during previous research^[1]. Measurements performed by Bruggeman^[2] confirm an increase in thrust due to clap-and-peel. These measurements show that this aero-elastic effect generates on average 8% more thrust. The measurements were performed by comparing the average thrust per flap cycle for the improved wing in normal (biplane) wing configuration with that of a single wing configuration.

In figure 6.10 the thrust during a flap cycle is plotted for the original wing and improved wing. When comparing the thrust generated by the original wing with that of the improved wing little differences are found. Figure 6.9 shows a slightly higher thrust for the original wing during the out-stroke. In section 6.3.1 it was already found that the original wing generates on average 8.2% extra thrust. Since the low pass filter also filtered the small thrust fluctuations, the difference seen in figure 6.10 cannot be said to be generated by just the out-stroke with certainty.

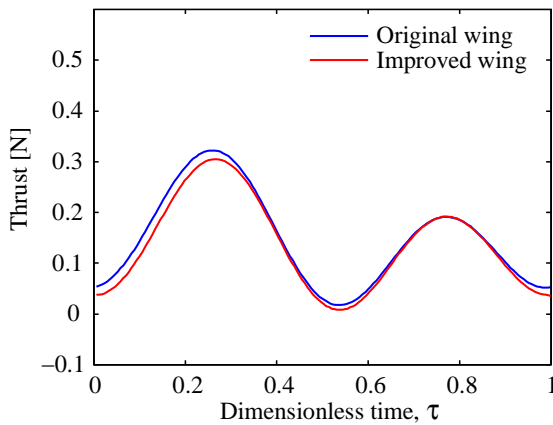


Figure 6.10. Average filtered thrust for the improved wing and original wing during one flap cycle at $f = 11$ Hz

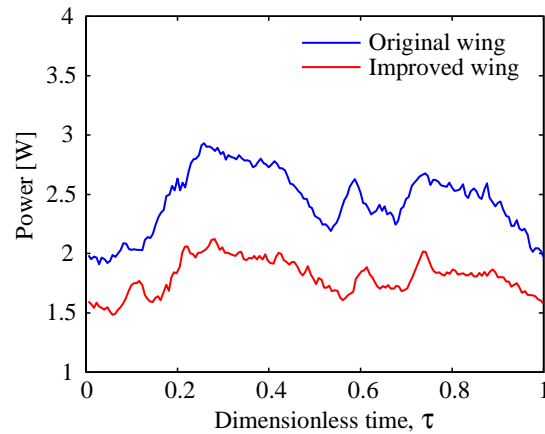


Figure 6.11. Average power consumption for the improved wing and original wing during one flap cycle at $f = 11$ Hz

As shown in section 6.3.1, the main difference between the original wing and improved wing is found in the power consumption. For the measurements of the power consumption it was not necessary to use a filter, so fluctuations with a small characteristic time are preserved. The power consumption is a measure for the forces that need to be overcome, like the losses in the driving mechanism, the elastic-inertial forces and the aerodynamic forces, lift (thrust) and drag. The aerodynamic drag for each wing cannot be measured in the set-up, because of symmetry the drag of both wings cancel each other, so the resulting force in normal direction is approximately zero.

In figure 6.11 the power consumption is plotted for the original wing and the improved wing. The power consumption during a flap cycle resembles the thrust generation, with peaks during the translation of the wing (in- and out-stroke). In the power consumption also small peaks are shown at the beginning of the translation. These are also shown in the thrust generation when the low pass filter is set to a higher cut-off frequency. These could therefore be due to aerodynamic effects, like the effect seen in rigid wing rotation (see paragraph 2.3). But the peaks could also be an elastic-inertial effect of the wing rotation or a mechanical effect due to

slip in the push rods of the driving mechanism. In figure 6.11 it can also be seen that the improved wing has a consistently lower power consumption over the whole flap cycle. This could mean an overall improvement in drag, but since the power consumption is also improved during the rotation of the wing the improvement is also found in an overall increase in elastic and mechanical efficiency.

6.4 PIV measurements on the hovering DelFly

The flow field around the DelFly wings is studied using stereoscopic PIV, which provides all three velocity components in the plane of the laser sheet. The in-plane velocity components are used to investigate the vortex dynamics in the cross-sectional plane normal to the wing leading edge. The out-of-plane velocity component represents the velocity component parallel to the leading edge and is discussed in section 6.4.6. In this paragraph the flow field and vortex dynamics are studied for various wings, at various flapping frequencies and at various spanwise locations.

6.4.1 Flow field during one flap cycle

The average flapping frequency needed to generate sufficient lift (thrust) to sustain hovering flight is approximately 13 Hz. The vortex development at spanwise locations $0.71R$ and $0.86R$ is monitored at 34 moments during the flap cycle. In this section, therefore, the choice is made to describe the flow field and vortex development for the improved wing flapping at 13 Hz and at spanwise location $0.71R$. Vortex development for the other measurements are shown in appendix C.

In figure 6.12 the velocity vector field at three moments during the flap cycle is shown. Velocity field A is at the half way during the in-stroke, velocity field B is at the end of in-stroke and velocity field C is halfway during the out-stroke. Note that in the first case the second wing is not in view. For this and for all other figures the left wing is studied, this is the wing placed perpendicular to the measurement plane, see figure 5.2. As a result, the right wing (dashed) disappears from the field of view at certain moments during the flap cycle. For the out-stroke the wing moves to the left and for the in-stroke the wing moves to the right. The vectors show the local velocity direction and magnitude and the background colour shows the absolute velocity (absolute length the of the in-plane velocity components). Masks are applied at regions where the PIV image was obscured by reflections or the image of the wings, which makes the velocity measurement unreliable. In figure 6.12 leading and trailing edge vortices are shown as a high velocity swirling motion around a low velocity core. The vortices are characterized by a circular streamline pattern. In figure 6.13 the streamlines corresponding to the velocity field images in figure 6.12 are plotted. Looking at the streamlines the vortices are now more clearly recognized as circular patterns.

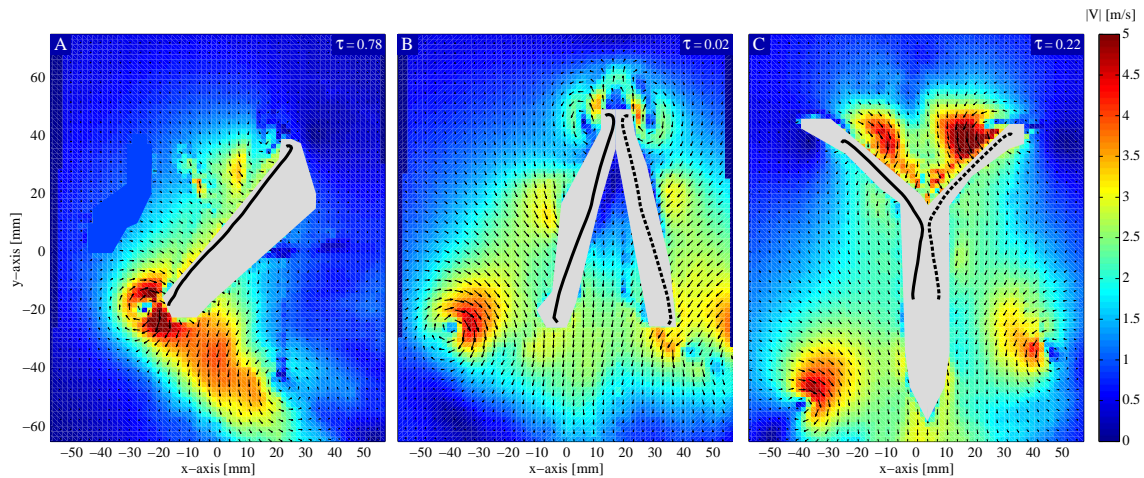


Figure 6.12. Velocity vector field at three moments during the flap cycle: halfway during the in-stroke (A), at the end of the in-stroke (B) and halfway during the out-stroke (C). Background shows absolute in plane velocity, with $|V| = \sqrt{u^2 + v^2}$. The measurement plane is oriented perpendicular to the left wing at spanwise location $0.71R$. Cross-sections of the wing at the measurement plane are shown for the left wing chord (continuous line) and right wing (dashed line)

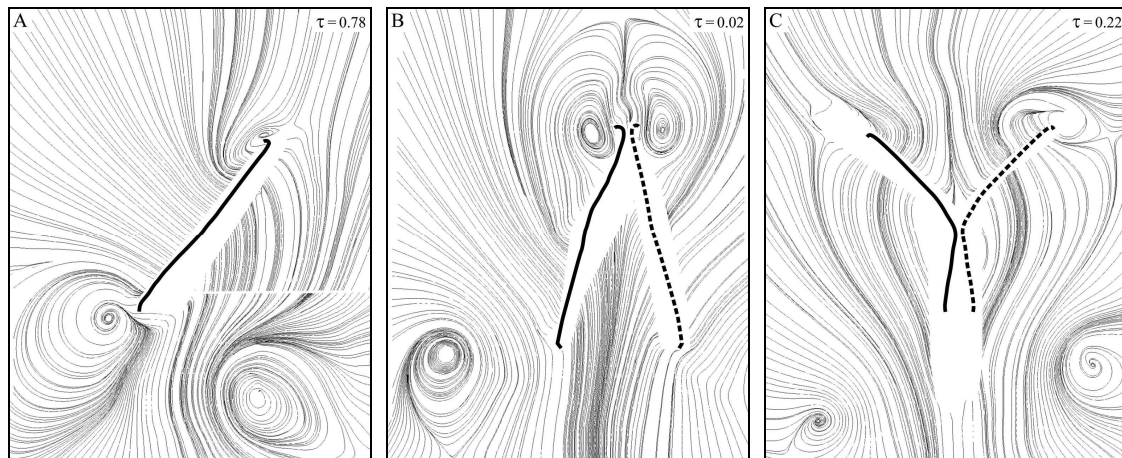


Figure 6.13. Streamlines corresponding to the velocity vector fields as shown in figure 6.12

For the investigation of the vortex development, the vortices need to be identified and quantified. Vortex strength can be quantified by calculation of the vorticity (curl of the velocity vector field). The vorticity however, does not only identify vortex cores but also shearing motion within the flow. The location of vortex cores and vortex strength are therefore determined from the swirling strength, which is calculated according to the method of R.J. Adrian *et al.*^[41] (see appendix B). The swirling strength of a local swirling motion is quantified by λ_{ci} , the positive imaginary part of the eigenvalue of the local velocity gradient tensor.

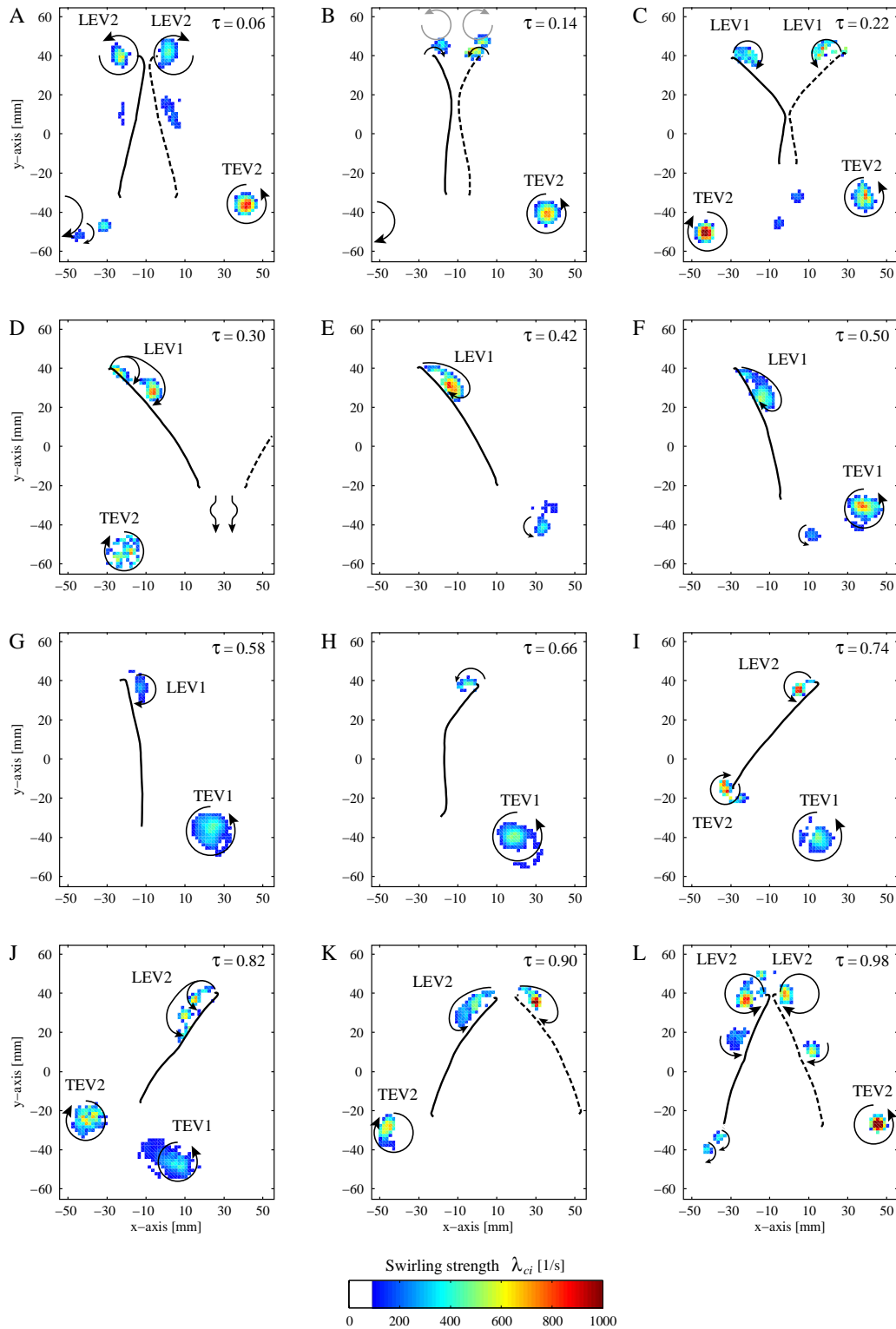


Figure 6.14. Swirling strength at various moments during the flap cycle for the improved wing flapping at 13 Hz and at spanwise location $0.71R$. Showing leading edge vortices (LEV) and trailing edge vortices (TEV), generated during the out-stroke (1) and in-stroke (2). Swirling direction as indicated in the figure is distracted from the velocity vector field images

In figure 6.14 the swirling strength at various moments during the flap cycle is shown, for the improved wing. The two cameras provide two flow fields. Since these two flow fields provide complementary information, the swirling strength in figure 6.14 is composed from PIV data from both flow fields. In figure 6.14 the leading edge vortex (LEV) and trailing edge vortex (TEV) development is shown. It can be seen that halfway during the out-stroke an LEV is generated (C). This vortex grows larger along the chord towards the trailing edge and another LEV starts to grow from the leading edge (D). The latter LEV grows while the vorticity of the first LEV is dissipated (E). At the end of the out-stroke (F) when the wing decelerates for rotation the LEV decreases in strength. At the beginning of the in-stroke (G) the LEV from the out-stroke appears to be dissipated. Also approximately halfway during the in-stroke an LEV is generated (I). Again the LEV grows larger and is shed towards the trailing edge, while a new LEV starts to grow (J). This LEV grows (K) until the leading edges touch (L). At the beginning of the out-stroke the vortices move above the leading edge (A), interact and dissipate when the leading edges start moving apart again (B).

The LEV development seems approximately the same for both in-stroke and out-stroke. The LEV during the out-stroke appears more close to the wing surface. This could be due to the downward velocity generated by the peel, which lowers the angle of attack. Furthermore it can be seen that while the LEVs from the out-stroke remain approximately at the same place and are dissipated during rotation, the LEVs from the in-stroke travel above the wing where they interact with each other. The LEVs start halfway during the translation, so not during the rotation as was theorized in previous the research^[1] of the DelFly (see paragraph 3.3).

During both in-stroke and out-stroke also a trailing edge vortex (or starting vortex) is generated. These strong TEVs dissipate more slowly and are slowly shed into the wake. During the out-stroke the development of the TEV is postponed due to the clap-and-peel. When the trailing edges separate the TEV appears to start from a complex fluid structure (D). This vortex appears to grow larger by merging with shed vorticity from the trailing edge as long as the wing is translating (E-F). During the in-stroke the TEV does start at the trailing edge (I) and grows larger and is shed from the trailing edge during translation (J).

The LEV development does not appear to be completely consistent with that described for insect flight^{[3][7]}. This could be due to the relative high Reynolds number. DelFly operates at a Reynolds number of 15,000 (see section 3.1.1) while insects fly at Reynolds numbers varying from 10 to 10,000. The higher Reynolds number could be the cause that the initial vortex has given enough time to grow relatively large, partly shed and another LEV is grown.

6.4.2 Flow field for clap-and-peel

In paragraph 6.3 it was shown that the clap-and-peel effect generates extra thrust during the out-stroke. The clap-and-peel also affects the vortex development. As can be seen in figure 6.14, the LEVs at the end of the in-stroke move above the wings and the LEVs during the out-stroke appear closer to the wing surface due to the extra downward flow during the peel. The generation of a TEV is postponed during the clap-and-peel phase of the out-stroke, but is visible at the end of the out-stroke. Previous research^[1] on the DelFly reports no TEV during the out-stroke. This could be due to the angle of the measurement plane. During the previous research the measurement plane was fixed with respect to the model (see figure 5.1). For the current investigation the plane of view remains perpendicular to the leading edge, which makes the angle at the end of the out-stroke the angle with respect to the referred previous research 45 degrees. The TEV is, therefore, suggested to be formed from a complex 3-dimensional flow, which is further investigated in section 6.4.5.

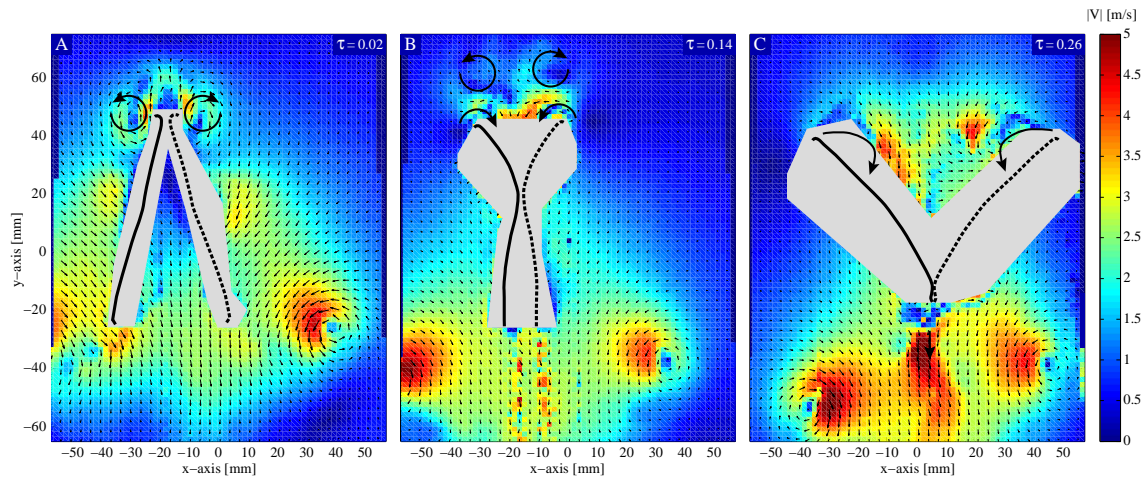


Figure 6.15. Velocity vector field at three moments during the clap-and-peel for the improved wing flapping at 13 Hz and at spanwise location $0.71R$

In figure 6.15 the velocity vector field during the clap-and-peel is shown. In figure 6.15A it can be seen that the upward flow at the end of the in-stroke, previously^[1] ascribed to the clapping of the leading edges, may be (completely) due the interaction of the two opposing LEVs from the in-stroke. The flow field during the clap-and-peel in figure 6.15 is comparable with the flow field results from Lehmann^[23] for clap-and-fling in figure 2.9, performed with rigid wings at lower Reynolds numbers. The LEVs from the in-stroke behave in the same manner, for both mechanisms the LEVs are moving above the leading edges. The flow field at the leading edge at the start of the peel (figure 6.15B) shows the same interaction between the LEVs from the in-stroke and air moving into the gap created by the peeling/flinging motion.

The flow field during the clap of the trailing edges is different. In figure 2.9 during the clap of the rigid wings little downward velocity is shown, while at the end of the fling an upward flow into the low pressure region between the wings through the gap at the trailing edges is shown. For the clap-and-peel, the flexible wings close the gap between the wings, so no upward velocity is shown. The clap of the trailing edges is postponed to a later stage and in figure 6.15C, a clear downward momentum jet is shown. The peak velocity of the downward momentum jet is found to be $5.0 \text{ m/s} \pm 0.5 \text{ m/s}$ for the improved wing at a span of $0.71R$. At a spanwise location of $0.86R$ the momentum jet due to the clap, is also visible in the velocity vector field images (although slightly earlier in the flap cycle) with approximately the same downward velocity.

6.4.3 Flow field for different wings

The flow field has been studied for three different wings, as described in figure 6.1. The flow field for the improved wing has been discussed in the previous sections. In this section the flow field around the improved wing is compared with the flow field around the original DelFly wing and the high aspect ratio wing.

The original DelFly wing has the same surface area and wing shape, but different stiffener layout. In paragraph 6.2 it could be seen that the in-flight wing deformation during translation is comparable with that of the improved wing, only during rotation the improved wing appeared more rigid, due to the more out-board stiffener location. In paragraph 6.3 the thrust generation also appeared similar for both wings. The main difference between the original and improved wing is found in the power consumption which is higher for the original wing. To investigate

the difference in flow field and vortex development, the velocity vector field and swirling strength during the complete flap cycle has been studied. The velocity vector field and the vortex development during the in-stroke appear to be similar for both wings. For the flow field during the out-stroke some differences are found.

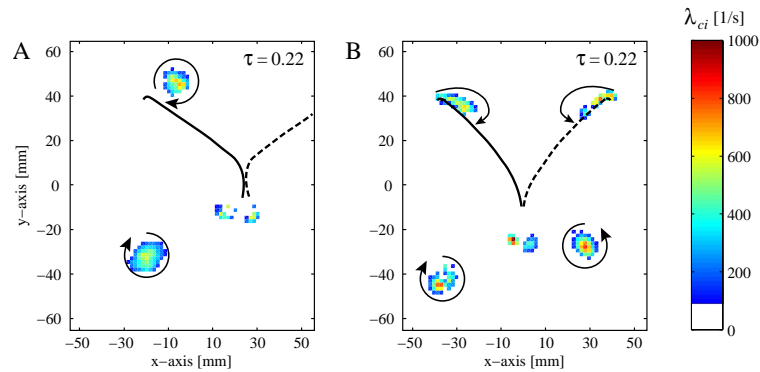


Figure 6.16. Swirling strength halfway during the out-stroke for the original wing (A) and the improved wing (B) flapping at 11 Hz at spanwise location $0.86R$

In figure 6.16 the swirling strength at the end of the peel (halfway during the out-stroke) is compared for the original and improved wing, for a flapping frequency of 11 Hz and at spanwise location $0.86R$. It can be seen that the LEV is closer to the wing surface for the improved wing. When the velocity vector fields for the same moment are compared, it can be seen that the vacuum effect between the peeling wings seems to create a stronger downward velocity for the improved wing, see figure 6.17. This lowers the angle of attack and is thought to create a more attached LEV. The found difference in the flow field could explain the slight increase in thrust during the out-stroke as seen in figure 6.10. The increased peel effect may be ascribed to the more rigid wing rotation of the improved wing. But, as explained in paragraph 6.3, a difference in foil tension between the wings could also be of influence, as this also affects thrust generation. For the difference in power consumption between the original and improved wing over the whole flap cycle, as shown in figure 6.10, no satisfactory aerodynamic explanation could be found from the flow field investigation.

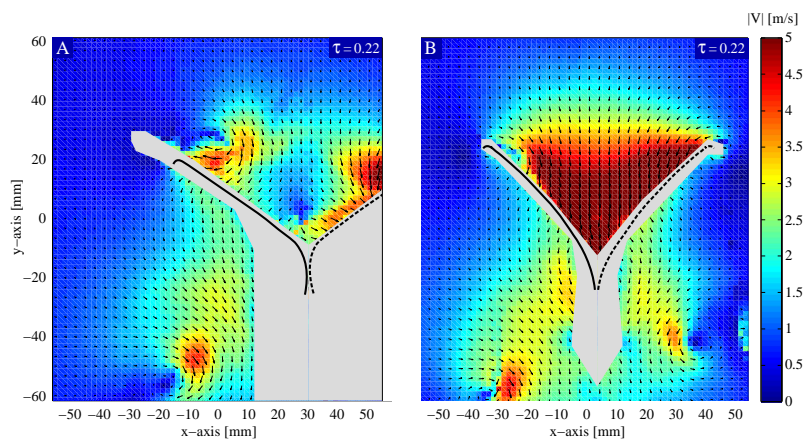


Figure 6.17. Velocity vector field halfway during the out-stroke for the original wing (A) and the improved wing (B) flapping at 11 Hz at spanwise location $0.86R$

The high aspect ratio wing has the same stiffener layout as the improved wing, but has a reduced chord length of 20 mm over the whole span. Because of its smaller chord length the high aspect ratio wing will operate at a lower Reynolds number, for a given flapping frequency. Considering hovering flight at a flapping frequency of 13 Hz, the Reynolds number for the improved DelFly wing is of order 15,000, while the Reynolds number for the high aspect ratio wing is of order 11,000. The differences in air flow around the wings are not considered to be only due to a Reynolds effect (which is an indication of inertial forces versus viscous forces). Other similarity parameters like the Strouhal number and Rossby number will also play a role, but an important effect is the aero-elastic effect. Changing the wing size will change the in-flight wing deformation and hence create a different air flow.

When looking at the in-flight wing motion of the high aspect ratio wing, it can be seen that the clap-and-peel is finished at an earlier moment due to the shorter chord length. When looking at the vortex development, it can be seen that for both the in-stroke and out-stroke the LEV appears to be stronger. This is illustrated in figure 6.18. In figure 6.18 the swirling strength is shown for the high aspect ratio wing flapping at 13 Hz at spanwise location $0.71R$. When comparing the LEV at the end of the out-stroke in figure 6.18A with figure 6.14E, it can be seen that the LEV is larger and stronger. The same can be said for the LEV at the end of the in-stroke (figure 6.18C versus figure 6.14L). The TEV seems to be equal in strength but this is more difficult to compare, since for the high aspect ratio wing the TEV is shed at an earlier moment. For the in-stroke this is shown in figure 6.18B. The TEV is shown to be shed at $\tau = 0.74$, while the TEV for the improved wing is shed 4% later, at $\tau = 0.78$. After the large TEV is shed, more small pockets of vorticity are shed from the trailing edge and combine with the large TEV.

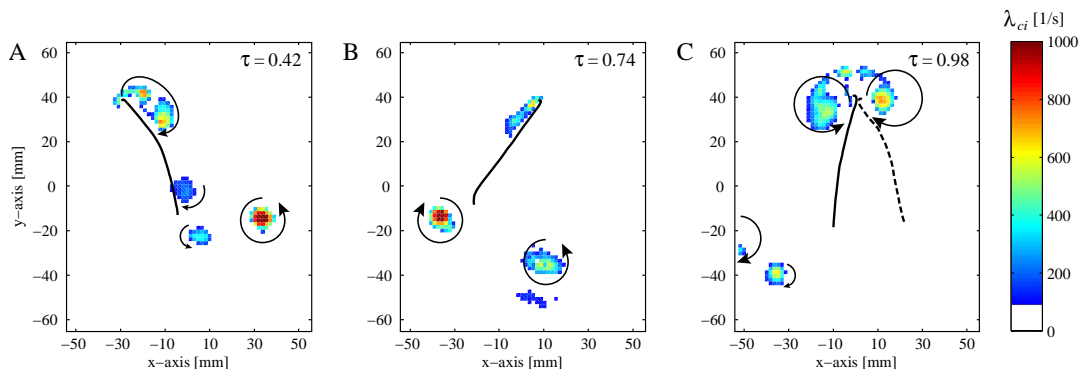


Figure 6.18. Swirling strength at the end of the out-stroke (A), halfway during the in-stroke (B) and at the end of the in-stroke (C) for the high aspect ratio wing flapping at 13 Hz at spanwise location $0.71R$

To get an indication of the complete vortex strength, the circulation is calculated for the LEVs at the end of the translation, since at this point the LEV is considered to be completely developed and is most clearly visible. The calculation of the circulation is not very accurate. The value found for the circulation is affected by the chosen vortex region, the presence of the counter rotating vortex and shear layer near the wing surface. The average velocity vector field found also has a rather large standard deviation at the vortex region and is obscured by reflections at the wing surface. The calculation of the circulation within the presented work should therefore be considered not an accurate value, but it can serve as an indication useful for comparison. For the calculation of the circulation is referred to appendix B.

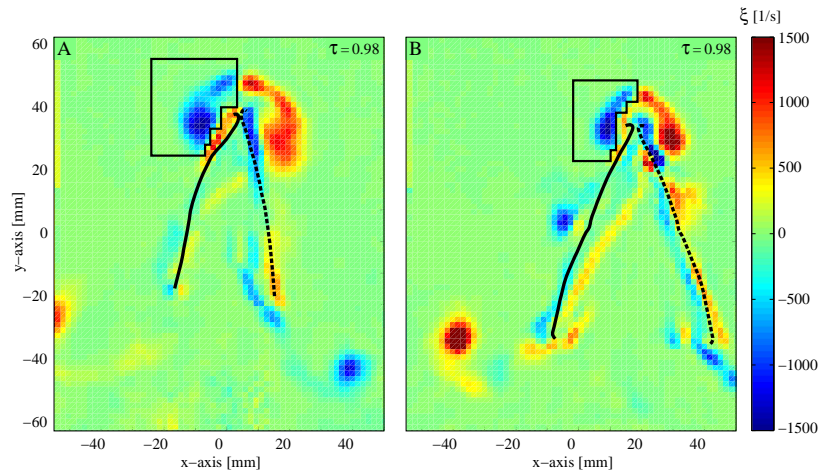


Figure 6.19. Vorticity plot at the end of the in-stroke for the high aspect ratio wing (A) and the improved wing (B) flapping at 13 Hz at spanwise location $0.71R$, with indicated the vortex region over which the circulation is calculated

In figure 6.18 it could be seen that the LEVs at the end of the translation are larger for the high aspect ratio wing compared with the improved wing. The circulation is calculated at the end of the translation. In figure 6.19 the vortex region is indicated for the calculation of the circulation at the end of the in-stroke. For the improved wing, the LEV circulation at the end of the in-stroke is $260 \text{ cm}^2/\text{s}$ while for the high aspect ratio wing the circulation found for the investigated region is $452 \text{ cm}^2/\text{s}$. This is a clear increase in circulation (of about 70%). For the LEV at the end of the out-stroke the circulation is calculated in the same manner. The value found for the circulation is overall higher, but still there is a clear increase in circulation for the high aspect ratio wing: $546 \text{ cm}^2/\text{s}$ for the improved wing and $754 \text{ cm}^2/\text{s}$ for the high aspect ratio wing (an increase of about 40%).

6.4.4 Effect of flapping frequency

The flow field is studied for the improved wing at three different flapping frequencies. For the same reasons as explained in section 6.4.3, changing the flapping frequency does not only change aerodynamic conditions, but changes the whole aero-elastic system. When considering the in-flight wing deformation it can be said that at high flapping frequencies the geometric angle of attack during translation is decreased. While at higher flapping frequency also extra heaving motion is observed.

The development of the LEV at the lower flapping frequencies is comparable with the LEV development at 13 Hz, shown in figure 6.14. Again during translation the LEV grows, is (partially) shed and another LEV is grown. In figure 6.20 the swirling strength is shown for the different frequencies, halfway during the out-stroke (A-C) and halfway during the in-stroke (D-F). During the in-stroke, the LEV at reduced frequencies appears stronger and more detached from the wing surface. Since this is also the case for the high aspect ratio wing with reduced chord length, this therefore may be considered a possible effect of the reduced Reynolds number. The stronger LEVs also move above the leading edges at the end of the in-stroke. For reduced frequencies, however, there is increased interaction between the LEVs and air flowing into the gap between the wings at the start of the out-stroke.

For the out-stroke the LEV development is affected by an increased clap-and-peel effect for higher flapping frequency. At reduced frequency the LEV again appears larger, but the local velocity is smaller. An increased downward airflow and smaller geometric angle of attack during the peel at higher frequency seems to cause the LEV to be closer to the wing surface, figure 6.20 (A-C).

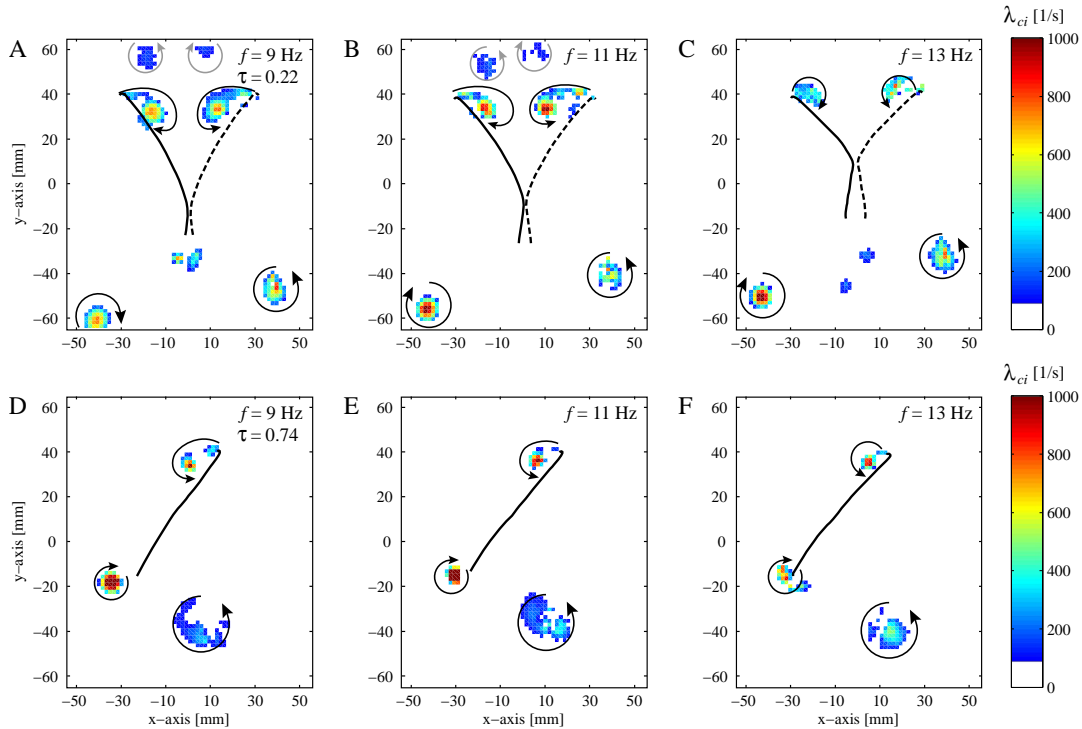


Figure 6.20. Swirling strength half-way during the out-stroke (A-C) and half-way during the in-stroke (D-F) for the improved wing at spanwise location $0.71R$, flapping at 9 Hz, at 11 Hz and at 13 Hz

The TEV development is also altered at reduced frequency. In figure 6.20 (D-F) it can be seen that at 13 Hz the TEV is being formed, at 11 Hz the TEV is being shed and at 9 Hz the TEV is already shed. Contrary to what is found for the LEV, the TEV appears weaker at reduced flapping frequencies. To get an impression of the vortex strength, again the circulation is calculated at the end of the in-stroke. In figure 6.21 the vortex region is indicated where the circulation is calculated. The circulation of the LEV at the end of the in-stroke is indeed increased for reduced flapping frequencies: $260 \text{ cm}^2/\text{s}$ for 13 Hz, $362 \text{ cm}^2/\text{s}$ for 11 Hz and $419 \text{ cm}^2/\text{s}$ for 9 Hz. The circulation of the TEV is decreased for reduced frequencies: $506 \text{ cm}^2/\text{s}$ for 13 Hz, $426 \text{ cm}^2/\text{s}$ for 11 Hz and $389 \text{ cm}^2/\text{s}$ for 9 Hz. As can be seen in figure 6.21 the circulation at the trailing edge is calculated for the main vortex. Since the TEV at reduced frequency is released at an earlier stage of the translation, extra pockets of vorticity are shed during the remainder of the translation. When these are taken into account the differences in TEV circulation are somewhat reduced.

For the out-stroke, the increase in vortex size at 9 Hz seems to be compensated by the increase in vortex velocity. The circulation of the LEV at the end of the out-stroke seems approximately equal at all three flapping frequencies: about $540 \text{ cm}^2/\text{s}$.

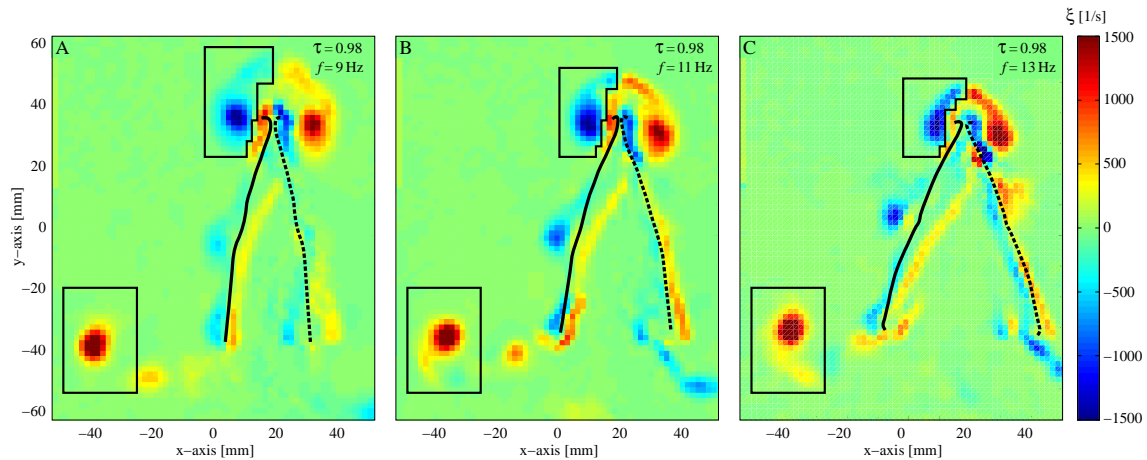


Figure 6.21. Vorticity plot at the end of the in-stroke for the improved wing at spanwise location $0.71R$, flapping at 9 Hz (A), at 11 Hz (B) and at 13 Hz (C), with indicated the vortex region over which the circulation is calculated

6.4.5 Flow field for varying spanwise location

The flow field has been studied at five spanwise locations, see figure 6.2. The measurements in this section are performed on the improved wing flapping at 13 Hz. The wing is tapered, so the chord length varies for the various measurements. Also the character of the flapping motion give the more out-board locations a higher velocity during translation. Furthermore the wing deformation is more severe for out-board locations; since the wing surface is fixed at the root it deforms more under aerodynamic loads at the more out-board locations.

Examination of the spanwise variation of the vortex development shows a conical growth from spanwise locations near the root to the tip. At the wing tip, however, all vortices are no longer present in the investigated flow region. During the in-stroke the LEV starts to develop at the out-board locations as soon as the translation starts. The same can be said for the TEV. In figure 6.22, the swirling strength is shown halfway during the in-stroke.

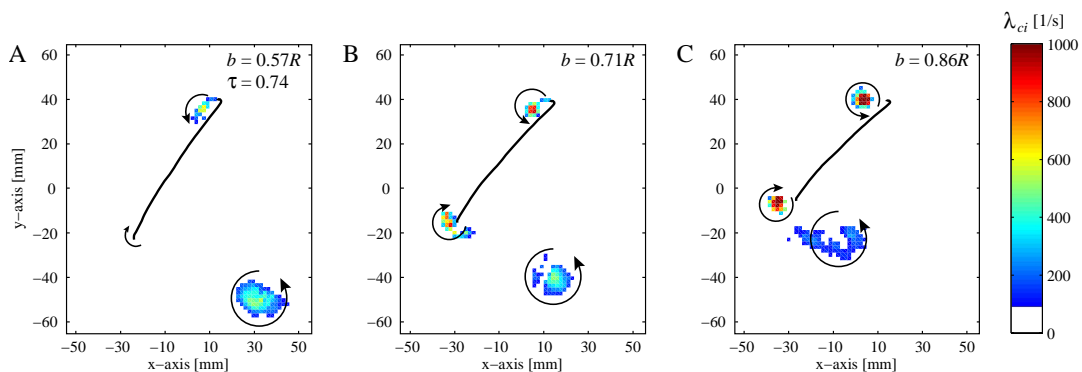


Figure 6.22. The swirling strength halfway during the in-stroke ($\tau = 0.74$) for the improved wing flapping at 13 Hz at three spanwise locations: $0.57R$ (A), $0.71R$ (B) and $0.86R$ (C)

In figure 6.22 it can be seen the LEV is already present at $0.86R$, while it is still developing at $0.71R$ and is not visible at $0.57R$. The TEV shows the same behaviour. Since the LEV is formed at an earlier stage it also grows large sooner at out-board locations and shows the partial

shedding and growth of a second LEV more clearly. The TEV is shed sooner at the more out-board locations, but while the TEV cannot follow the trailing edge at $0.55R$ and $0.71R$, it does seem to remain close to the trailing edge at $0.86R$. In figure 6.23 the spanwise vortex development is sketched for three moments during the in-stroke.

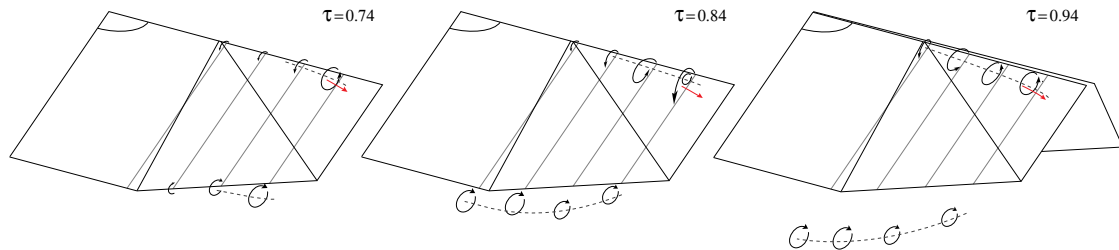


Figure 6.23. Sketch of the spanwise vortex development during in-stroke for the improved wing flapping at 13 Hz, where the dashed line is an indication of the vortex tube and the red arrow an indication of the spanwise flow in the vortex tube

During the out-stroke the vortices also start to develop at the out-board locations, since the local translational velocity is larger. The clap-and-peel, however, affects the remainder of the vortex development. The LEV seems more suppressed due to the down flow, see figure 6.24. At the end of the translation, the downward velocity combined with the wing deformation gives the wing such a reduced angle of attack, that no flow separation is visible at spanwise location $0.86R$.

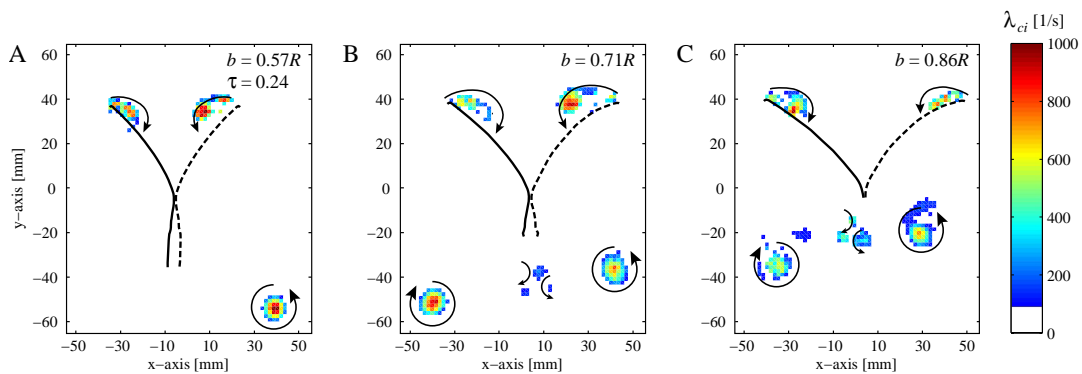


Figure 6.24. The swirling strength half-way during the out-stroke ($\tau = 0.24$) for the improved wing flapping at 13 Hz at three spanwise locations: $0.57R$ (A), $0.71R$ (B) and $0.86R$ (C)

The development of the TEV is postponed during the clap-and-peel. After the clap-and-peel, when the wings are physically separated, the TEV does not start at the wing trailing edge. The TEV seems to start from a wake region in between the wings and appears in the field of view at some distance from the trailing edge at the end of the out-stroke. The TEV appears at a later stage for in-board locations and does not seem to appear at spanwise position $0.41R$. The TEV development is therefore theorized to be forked (resembling a Y-shape) when viewed from the top (looking down on the hovering DelFly). Possible future flow field measurements in a plane parallel to the leading edge could reveal more about the TEV development during the out-stroke. In figure 6.25 the spanwise vortex development is sketched for three moments during the out-stroke.

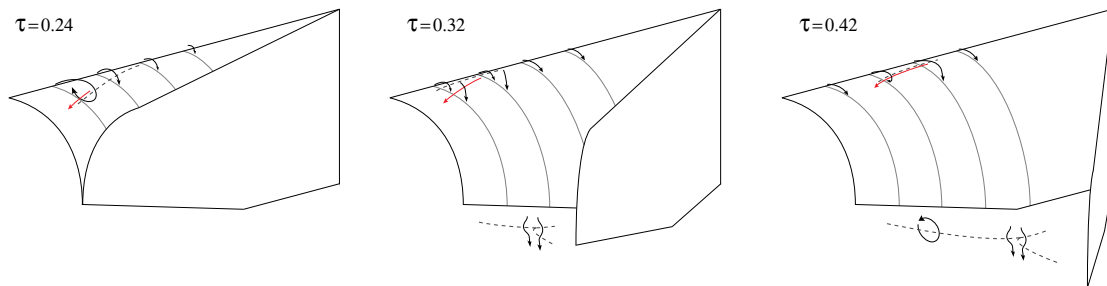


Figure 6.25. Sketch of the spanwise vortex development during out-stroke for the improved wing flapping at 13 Hz, where the dashed line is an indication of the vortex tube and the red arrow an indication of the spanwise flow in the vortex tube

6.4.6 Spanwise flow

The results from the stereoscopic PIV make it possible to investigate the out-of-plane velocity component in the measurement plane. Investigation of the out-of-plane velocity for the improved wing flapping at 13 Hz during the clap-and-peel phase shows the vacuum region created during the peel, to create not only a down flow but also an air flow in-board between the wings. At spanwise location $0.71R$ the minimum spanwise velocity, $V_{z,min} = -2.5 \text{ m/s} \pm 0.2 \text{ m/s}$. This air flow between the wings remains in in-board direction during the in-stroke up until the end of the in-stroke, when the leading edges nearly touch at $\tau = 0.84$. During the last part of the flap cycle an out-board air flow is created between the wings when the wings clap together, with $V_{z,max} = 1.0 \text{ m/s} \pm 0.2 \text{ m/s}$.

Investigations into the out-of-plane velocity in insect flight^[7] show an axial flow present within the LEV core for models of insect wings with Reynolds numbers in the order of 1400. The current research also shows the presence of axial flow in the vortex cores. The axial flow within the core of an LEV is more clearly visible at reduced frequencies where the LEV is larger.

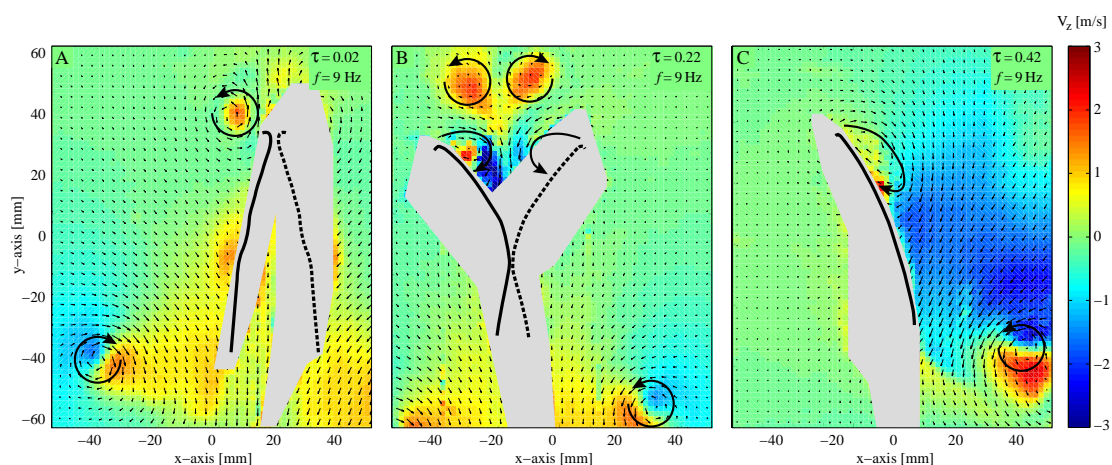


Figure 6.26. Velocity vector field at three moments during the out-stroke; at the start (A), halfway (B) and at the end (C) of the out-stroke at spanwise location $0.71R$. The background colour shows the magnitude of the out-of-plane velocity component, where a positive velocity is an out-board flow

In figure 6.26 the velocity vector field during the out-stroke is shown for a flapping frequency of 9 Hz, with the magnitude of the spanwise flow as background colour. The positive axial flow in the LEV core is visible. The magnitude of the axial flow as shown in the LEV at the end of the in-stroke (figure 6.26A) is $1.5 \text{ m/s} \pm 0.7 \text{ m/s}$, which is of the same order as the maximum translational velocity at that spanwise location. During the start of the out-stroke (figure 6.26B) the LEV cores from the in-stroke are clearly visible as they move above the leading edges.

In figure 6.27 the spanwise flow is shown for the in-stroke for a flapping frequency of 11 Hz. Again the LEV appears to hold an axial flow in its core. For the TEV an axial flow in its core is not clearly visible. The vortex tube appears to have an angle with respect to the measurement plane. This gives the vortex tube for one half a positive spanwise flow and for the other half a negative spanwise flow, but the spanwise flow in the TEV core seems to be negative, hence an in-board flow. The skew TEV vortex tube could already be seen in the previous section, when investigating the vortex development at various spanwise locations.

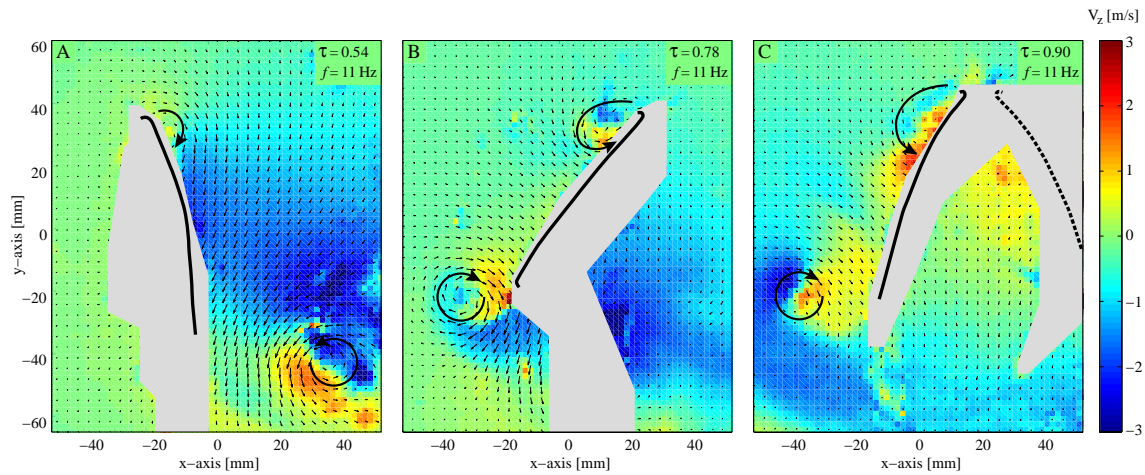


Figure 6.27. Velocity vector field at three moments during the in-stroke; at the start (A), halfway (B) and at the end (C) of the in-stroke at spanwise location $0.71R$. The background colour shows the magnitude of the out-of-plane velocity component, where a positive velocity is an out-board flow

Conclusions and recommendations

In chapter 6 the in-flight wing deformation, as well as the results from the experimental force and flow field measurements were discussed. This chapter summarizes the findings from chapter 6 and gives recommendations for further research on the DelFly.

7.1 Conclusions

The goal of the thesis is stated in the introduction as:

Gain a better understanding of the aerodynamic mechanisms generating forces on a hovering flapping-wing MAV. With the purpose to further improve it.

In this paragraph the two most important aerodynamic mechanisms for the DelFly are discussed. To further improve the DelFly, the effect of changing wing parameters was investigated, in order to determine how this influences the aerodynamic mechanisms and how this may affect the DelFly's overall performance. This is done by comparison of the three wings investigated in chapter 6.

7.1.1 Leading edge vortex development

An important aerodynamic mechanism generating lift for flapping wing flight is the *leading edge vortex* (LEV). The LEV originates from a dynamic stall effect where the flow separates from the leading edge for thin airfoils at high angle of attack, but instead of resulting in a complete stall, the flow reattaches further down the airfoil to form a vortex that remains more or less steady with respect to the wing. The vortex development is studied for the DelFly wing during hovering flight by investigation of the swirling strength of the flow field as measured in the PIV experiments. For the DelFly wing an LEV is generated approximately halfway during the translation. This LEV grows larger and is shed along the chord and at this time a new LEV starts to grow at the leading edge. This second LEV is dissipated at the end of the out-stroke during wing rotation, but at the end of the in-stroke this LEV moves above the wings and interacts with the counter-rotating LEV from the mirror wing. This LEV development is not completely consistent with that described for insect flight^{[3][7]}. The fact that the DelFly operates at a higher Reynolds number than insects, could be the cause of the shedding of the initial vortex and start of a second.

The LEV for the DelFly wing develops conically along the leading edge. The LEV is first visible at out-board positions, where the translational velocity is higher, and at a later stage of the flap cycle at more in-board locations. Since the vortices at out-board positions start at an earlier stage, they grow larger and are also shed at an earlier stage, where it is interesting to note that the TEV is completely shed into the wake at more in-board positions whereas it is able to follow the trailing edge more out-board. The vortex tube does not extend all the way to the wing tip. While the LEV is still clearly visible at $0.86R$, it has disappeared at the wing tip. Here the LEV vortex tube has probably become connected to the tip vortex and bent towards the trailing edge. Inside the vortex tube a spanwise velocity component out-board is present, which is approximately of the same magnitude of the maximum translational velocity at that spanwise location.

The force measurements showed a linear increase in thrust with flapping frequency. The thrust-to-power ratio is approximately constant for the operational frequency range. The flow field investigations showed the same trend in vortex development for all the flapping frequencies where flow measurements were carried out (9 Hz, 11 Hz and 13 Hz). The vortex size and strength, however, does vary at different frequencies. The LEV strength (circulation) is decreased for higher flapping frequencies, while the TEV strength increases for higher flapping frequencies.

7.1.2 Clap-and-peel mechanism

Another important aerodynamic mechanism for the DelFly, as identified in previous research^[1], is the *clap-and-peel* mechanism. From the recorded in-flight wing deformation it could be seen that during the start of the out-stroke the wings peel apart at the leading edge, while they clap together at the trailing edge. The thrust measurements showed a higher translational peak during the out-stroke, which is probably due to this clap-and-peel. Measurements performed by Bruggeman^[2] showed an average increase in thrust of 8% for wings that use clap-and-peel, with respect to isolated wings.

The flow field measurements showed that the peeling of the wings creates a down flow as well as a spanwise flow in-board. In contrast to the clap-and-fling experienced by rigid wings^[23], no upward flow is shown towards the suction area, since the flexibility of the DelFly wings closes the gap in between them. The clap of the wings creates a downward momentum jet, which is also thought to increase thrust generation.

Vortex development is also affected by the clap-and-peel. The LEV appears closer to the wing surface due to the strong down flow, reducing the effective angle of attack. At certain moments during the out-stroke, this completely prevents flow separation at the out-board spanwise position. The TEV development is postponed during the start of the out-stroke as long as the clap of the trailing edges is not completed. A TEV is visible later during the out-stroke, but this appears suddenly at some distance from the trailing edge, as the measurement plane is rotated to remain perpendicular to the wing surface. The TEV, therefore, might have a forked appearance, starting from the wake region that exists in between the wings after the clap.

7.1.3 Wing comparison

The improved wing from the wing geometry study, performed by Bruggeman^[2], has the same wing layout as the original DelFly II wing. The difference is found in the stiffener location and orientation. From the in-flight wing deformation it could be seen, that the more out-board placed stiffeners give the improved wing more rigidity at these positions during wing rotation. While

the research of Bruggeman showed the improved wing to have the same thrust production as the original wing, the presented research showed a decrease in thrust, which could be due to various causes, like small variations in wing mounting, foil tension and/or deterioration of the driving mechanism. The improved wing does show a clear decrease in power consumption, increasing efficiency (thrust-to-power ratio). The cause of the consistently lower power consumption over the whole flap cycle remains unclear, however.

The flow field measurements show a difference in the flow fields of both wings during the clap-and-peel. The LEV during the out-stroke appears larger for the original wing. The improved wing shows a stronger down flow, decreasing LEV size, which might be due to the more rigid wing rotation.

The improved wing was also compared to a high aspect ratio wing (33% increased AR), which has the same stiffener orientation, but a reduced wing chord. The high aspect ratio wing shows a significant increase in LEV size and strength (circulation) at equal flapping frequency. Although in-flight wing deformation is also altered, this is probably an effect of the decreased Reynolds number.

7.2 Recommendations

Although a lot of new knowledge is gained during the investigations described in this report, the actual application of this knowledge in terms of realizing a significant improved wing is not yet attained. The design of an optimal flapping wing is very complex, since many design parameters can be altered. It is therefore recommended to perform additional research. Experimental research on more different wings could help establish a more clear connection between the aerodynamic effects and wing performance. Also numerical research may be used to perform a parametric wing geometry study. The in-flight wing deformation shown in this report could be used as input for numerical flow simulations of flapping flight or as a benchmark for future full fluid-structure interaction simulations.

For future force measurements a more rigid experimental set-up should be used with stiffer force sensors, to prevent mechanical resonance falling within the measurement range, which is necessary to significantly reduce the vibrations that hampered the current research. Without mechanical resonance, small thrust variations during the flap cycle can be investigated, such as force peaks during wing rotation (rotational effects). The measurements of the present research also suffered from problems with repeatability, associated to the DelFly's construction. Future measurements should therefore be done on a DelFly model with the new driving mechanism resulting from the research of Bruggeman ^[2], and foil tension should be considered as this proved to be of significant influence.

Future flow field investigations could focus on vortex development for forward flight. Combined with lift and drag measurements an optimized wing for this flight condition might prove to be different from a wing optimized for hovering. Since Reynolds effects were shown to exist, investigations for the smaller DelFly Micro could lead to an optimization for its specific Reynolds regime. As final recommendation, an investigation of tail effects is advised. The tail has been omitted in the presented research, but the tail is known to affect flight performance and flight control. The presence of a tail could influence the whole flow field and measurements might help to optimize tail geometry, location and orientation with respect to the flapping wings.

Bibliography

- [1] De Clercq, K.M.E. “Flow visualization and force measurements on a hovering flapping wing MAV DelFly II”, *Delft University of Technology M.Sc. thesis*, (2009)
- [2] Bruggeman, B. “Improving flight performance of DelFly II in hover by improving wing design and driving mechanism”, *Delft University of Technology M.Sc. thesis*, (2010)
- [3] Ellington, C.P.; Van den Berg, C.; Willmott, A.P.; Thomas, A.L.R. “Leading-Edge Vortices in Insect Flight”, *Nature*, Vol. 384, pp. 626-630, (1996)
- [4] Sane, S.P. “Review: The aerodynamics of insect flight”, *The journal of Experimental Biology*, vol. 206, pp. 4191-4208, (2003)
- [5] Ellington, C.P. “The aerodynamics of hovering insect flight III Kinematics”, *Phil. Trans. R. Soc. Lond. B*, vol. 305, pp. 41-78, (1984)
- [6] Ellington, C.P. “The novel aerodynamics of insect flight: Applications to micro-air vehicles”, *The journal of Experimental Biology*, vol. 202, pp. 3439-3448, (1999)
- [7] Birch, J.M.; Dickson, W.B.; Dickinson, M.H. “Force production and flow structure of the leading edge vortex on flapping wings at high and low Reynolds numbers”, *The journal of Experimental Biology*, vol. 207, pp. 1063-1072, (2004)
- [8] Singh, B.; Inderjit, C.; Manikandan R.; Leishman, J.G. “Experimental Studies on Insect-Based Flapping Wings for Micro Hovering Air Vehicles”, *46th AIAA Structures, Structural Dynamics & Materials Conference, Austin, Texas*, AIAA 2005-2293, (2005)
- [9] Lehmann, F.O. “The mechanisms of lift enhancement in insect flight”, *Naturwissenschaften*, vol. 91, pp. 101-122, (2004)
- [10] Lehmann, F.O. “Review: When wings touch wakes: understanding locomotor force control by wake-wing interference in insect wings”, *The journal of Experimental Biology*, vol. 211, pp. 224-233, (2008)
- [11] Ansari, S.A.; Phillips, N.; Stabler, G.; Wilkins, P.C.; Zbikowski, R.; Knowles, K. “Experimental investigation of some aspects of insect-like flapping flight aerodynamics for application to micro air vehicles”, *Exp Fluids*, vol. 46, pp. 777-798 (2009)

- [12] Wilkins, P.; Knowles, K. "Investigation of aerodynamics relevant to flapping-wing micro air vehicles" *37th AIAA Fluid Dynamics conference and Exhibit, Miami, Florida, AIAA 2007-4338*, (2007)
- [13] Ansari, S.A.; Knowles, K.; Zbikowski, R. "Insectlike Flapping Wings in the Hover Part 1: Effect of Wing Kinematics" *Journal of Aircraft*, vol. 45, pp. 1945-1954, (2008)
- [14] Lehmann, F.O.; Pick, S. "The aerodynamic benefit of wing-wing interaction depends on stroke trajectory in flapping insect wings", *The journal of Experimental Biology*, vol. 210, pp. 1362-1377, (2007)
- [15] Dickinson, M.H.; Lehmann, F.O.; Sane, S.P. "Wing Rotation and the Aerodynamic Basis of Insect Flight", *Science*, vol. 284, pp. 1954-1960, (1999)
- [16] Lighthill, M.J. "On the Weis-Fogh mechanism of lift generation", *J. Fluid Mech.*, vol. 60, pp. 1-17, (1973)
- [17] Anderson, J.D. "Fundamentals of Aerodynamics", 3rd edition, McGraw-Hill, New York, (2001)
- [18] Wu, J.Z.; Vakili, A.D.; Wu, J.M. "Review of the physics of enhancing vortex lift by unsteady excitation", *Prog. Aerospace Sci.*, vol. 28, pp. 73-131 (1991)
- [19] Willmott, P.W.; Ellington, C.P.; Tomas, A.L.R. "Flow visualization and unsteady aerodynamics in the flight of the hawkmoth, *Manduca sexta*", *Phil. Trans. R. Soc. Lond. B*, vol. 352, pp. 303-316, (1997)
- [20] Van den Berg, C.; Ellington, C.P. "The three-dimensional leading edge vortex of a 'hovering' model hawkmoth", *Phil. Trans. R. Soc. Lond. B*, vol. 352, pp. 329-340, (1997)
- [21] Bomphrey, R.J.; Lawson, N.J.; Harding, N.J.; Taylor, G.K.; Thomas, A.L.R. "The aerodynamics of *Manduca sexta*: digital particle image velocimetry analysis of the leading-edge vortex", *The journal of Experimental Biology*, vol. 208, pp. 1079-1094, (2005)
- [22] Sane, S.P.; Dickinson, M.H. "The aerodynamic effects of wing rotation and a revised quasi-steady model of flapping flight", *The Journal of Experimental Biology*, vol. 205, pp. 1087-1096, (2002)
- [23] Lehmann, F.O.; Sane, S.P.; Dickinson, M. "The aerodynamic effect of wing-wing interaction in flapping insect wings", *Journal of Experimental Biology*, Vol. 208, pp. 3075-3092, (2005)
- [24] Miller, L.A.; Peskin, C.S. "Flexible clap and fling in tiny insect flight", *Journal of Experimental Biology*, Vol. 212, pp. 3076-3090, (2009)
- [25] Combes, S.A.; Daniel, T.L. "Into thin air: contributions of aerodynamic and inertial-elastic forces to wing bending in the hawkmoth *Manduca sexta*" , *Journal of Experimental Biology*, Vol. 206, pp. 2999-3006, (2003)

- [26] Heathcote, S.; Wang, Z.; Gursul, I. "Effect of spanwise flexibility on flapping wing propulsion", *Journal of Fluids and Structures*, Vol. 24, pp. 183-199, (2008)
- [27] Gopalakrishnan, P.; Tafti, D.K. "Effect of Wing Flexibility on Lift and Thrust Production in Flapping Flight", *AIAA Journal*, Vol. 48, pp. 865-877, (2010)
- [28] Eldredge, J.D.; Toomey, J.; Medina, A. "On the roles of chord-wise flexibility in a flapping wing with hovering kinematics", *J. Fluid Mech.*, vol. 659, pp. 94-115, (2010)
- [29] Mountcastle, A.M.; Daniel, T.L. "Aerodynamic and functional consequences of wing compliance", *Exp Fluids*, Vol. 46, pp. 873-882, (2009)
- [30] Zhao, L.; Huang, Q.; Deng, X.; Sane, S.P. "Aerodynamic effects of flexibility in flapping wings", *J. R. Soc. Interface*, Vol. 7, pp. 485-497, (2010)
- [31] Groen, M.A.; Bruggeman, B.; Remes, B.; Ruijsink, R.; Van Oudheusden, B.W.; Bijl, H.; "Improving flight performance of the flapping wing MAV DelFly II", *International Micro Air Vehicle Conference and Flight Competition, Braunschweig, Germany*, (2010)
- [32] De Croon, G.C.H.E.; De Clercq, K.M.E.; Ruijsink, R.; Remes, B.; De Wagter C. "Design, aerodynamics, and vision-based control of the DelFly", *International Journal of MAV*, Vol. 1, pp. 71-97, (2009)
- [33] Bradshaw, N.L.; Lentink, D. "Aerodynamic and Structural Dynamic Identification of a flapping wing Micro Air Vehicle", *26th AIAA Applied Aerodynamics Conference, Honolulu, Hawaii*, AIAA 2008-6248, (2008)
- [34] Lentink, D.; Dickinson, M.H. "Biofluiddynamic scaling of flapping, spinning and translating fins and wings", *Journal of Experimental Biology*, Vol. 212, pp. 2691-2704, (2009)
- [35] Lewin, G.C.; Haj-Hariri, H. "Modelling thrust generation of a two-dimensional heaving airfoil in a viscous flow", *J. Fluid Mech.*, Vol. 492, pp. 339-362, (2003)
- [36] Taylor, G.K.; Nudds, R.L.; Thomas, A.L.R. "Flying and swimming animals cruise at a Strouhal number tuned for high power efficiency", *Nature*, Vol. 425, pp. 707-711, (2003)
- [37] www.DelFly.nl, last visit November 2010
- [38] Raffel, M.; Willert, C.E.; Wereley, S.T.; Kompenhans, J. "Particle Image Velocimetry: A Practical Guide", 2nd edition, Springer-Verlag, Berlin Heidelberg, (2007)
- [39] Scarano, F. "AE4-180 Experimental Aerodynamics", *Delft University of Technology course notes*, chapter 9 PIV, pp.107-130, (2008)
- [40] Lawson, N.J.; Wu, J. "Three-dimensional particle image velocimetry: experimental error analysis of a digital angular stereoscopic system", *Measurement Science and Technology*, Vol. 8, pp. 1455-1464, (1997)

- [41] Adrian, R.J.; Christensen, K.T.; Liu, Z.C. "Analysis and interpretation of instantaneous turbulent velocity fields", *Experiments in Fluids*, Vol. 29, pp. 275-290, (2000)
- [42] Dubief, Y.; Delcayre, F. "On coherent-vortex identification in turbulence" *Journal of Turbulence*, Vol. 1, Art. No. N11, (2000)

Appendix A

DeIFly II Specifications

Parameter	Formula	Value	Unit
mass (including camera)	m	17 ± 1	g
flapping frequency range	f	11-14	Hz
wing dihedral angle	ψ	12	deg
wing maximum stroke angle	ϕ	44	deg
wing stroke amplitude	$A = 2R \sin(\phi/2)$	105	mm
wing span	b	280	mm
semi wing span	R	140	mm
semi wing area	S	11,195	mm ²
mean chord length	$\bar{c} = S/R$	79.96	mm
aspect ratio	$AR = b^2/2S$	3.50	-
wing loading	$m \cdot g / 4S$	3.72	N/m ²
mean wingtip velocity (at 13Hz hovering)	$\bar{V}_t = 2\phi f R$	2.80	m/s
maximum flight velocity (at 11 Hz)	V_{\max}	7.00	m/s
Reynolds number at \bar{V}_t	$Re = \bar{c} \bar{V}_t / \nu$	15,305	-
Reynolds number at V_{\max}	$Re = \bar{c} V_{\max} / \nu$	38,326	-
Strouhal number at \bar{V}_t *	$St = f A / \bar{V}_t$	0.49	-
Strouhal number at V_{\max}	$St = f A / V_{\max}$	0.16	-

* For hovering conditions it would be better to use the mean down wash velocity to calculate the Strouhal number, but an exact velocity cannot be obtained from the experimental data and a theoretical value from for example actuator disk theory^[1] is also not very accurate for biplane flapping wings.

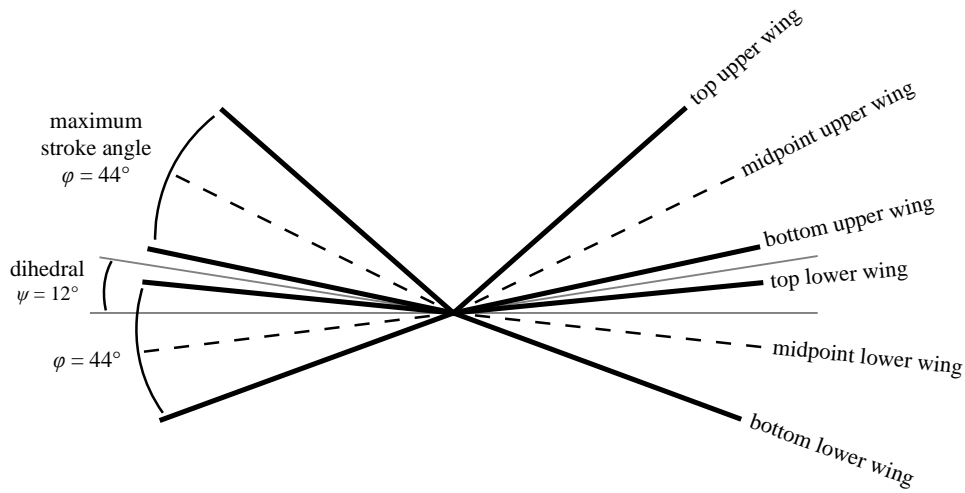


Figure A.1. Front view showing the wing leading edges and relevant angles. Adapted from Bruggeman^[2] / De Clercq^[1]

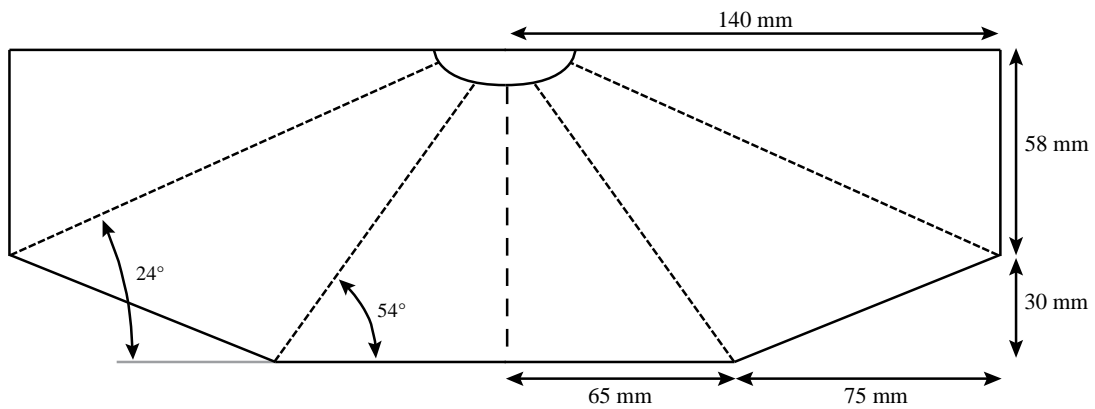


Figure A.2. Wing dimensions and stiffener location and orientation of the original DelFly II wing. Adapted from Bruggeman^[2]

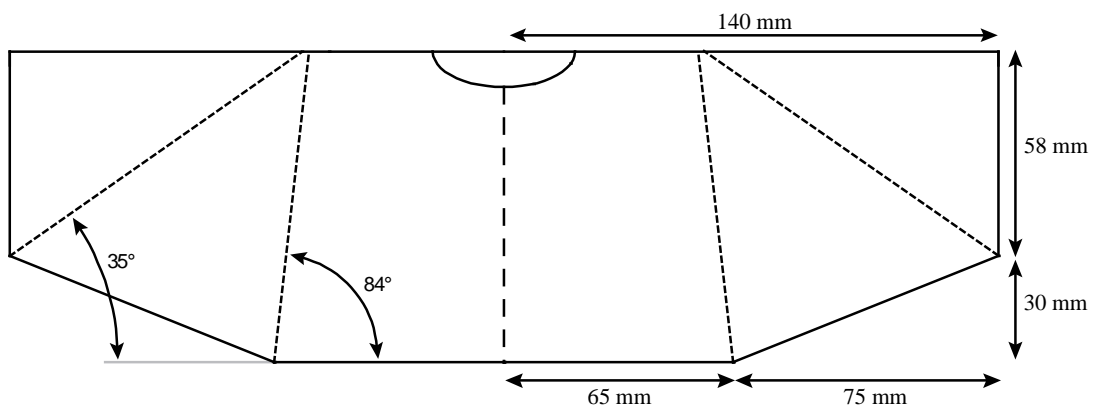


Figure A.3. Wing dimensions and stiffener location and orientation of the improved wing. Adapted from Bruggeman^[2]

Appendix B

Vorticity and swirling strength calculations

Vortices or eddies of various size and strength may be present within random fluid flows. These structures are well known for years, but there is no general consensus about how to define and indentify them. One definition of a vortex proposed by Kline and Robinson in 1989 is: “A vortex exists when instantaneous streamlines mapped onto a plane normal to the core exhibit a roughly circular pattern, when viewed in a reference frame moving with the center of the vortex core”^[41]. In order to investigate vortex development, vortices must be indentified and quantified within a given flow field. The straight forward method of using the out-of-plane component of the vorticity vector does not provide a satisfying result, since vorticity does not only identifies vortex cores but also shearing motion within the flow. There exist many other methods that are used in vortex identification. Most of them involve an analysis of the local velocity gradient tensor and its corresponding eigenvalues or the Hessian of pressure^[41]. Two examples of these methods are discussed in the report of De Clercq^[1]. The first is the Q-method which uses the second invariant of the velocity tensor to distinguish between the shear and the rotation in a flow. The second method uses the Hessian of pressure to provide information on local pressure minima, which are found in vortex cores^[42].

The current research uses the swirling strength for the identification and quantification of vortices, which is calculated according to the method of Adrian *et al.*^[41]. This method is readily applied in the PIV software and performs well. This method makes use of the eigenvalues of the velocity gradient tensor. When the discriminant of the characteristic equation is positive, the three-dimensional velocity gradient has one real eigenvalue (λ_r) and a pair of complex conjugate eigenvalues ($\lambda_r \pm i\lambda_{ci}$). When this is true, the particle exhibits a swirling, spiral motion about the eigenvector corresponding to λ_r . The reciprocal of λ_{ci} represents the period required for a particle to swirl once about the λ_r -axis. If the flow is a pure shear flow, the particle orbits are infinitely-long ellipses and the orbit period is also infinite, corresponding to $\lambda_{ci} = 0$. Thus, $\lambda_{ci} > 0$ corresponds to shorter more circular ellipses, i.e. vortices or eddies. Vortex identification based on swirling strength is frame independent, and does not reveal regions which contain significant vorticity but are absent of any local swirling motion (i.e. shear layers).

For two-dimensional flow fields the velocity gradient tensor has either two real eigenvalues or one pair of complex conjugate eigenvalues. In this case an equivalent two-dimensional form is used, which identifies vortices as iso-regions of $\lambda_{ci} > 0$.

According to its definition the swirling strength is calculated from the eigenvalue of the velocity gradient tensor:

$$\nabla \mathbf{V} = \begin{bmatrix} \frac{\partial u}{\partial x} & \frac{\partial u}{\partial y} \\ \frac{\partial v}{\partial x} & \frac{\partial v}{\partial y} \end{bmatrix} \quad (\text{B.1})$$

The eigenvalue is calculated from the characteristic equation:

$$\left(\frac{\partial u}{\partial x} - \lambda \right) \left(\frac{\partial v}{\partial y} - \lambda \right) - \frac{\partial u}{\partial y} \frac{\partial v}{\partial x} = 0 \quad (\text{B.2})$$

$$\lambda^2 - \left(\frac{\partial u}{\partial x} + \frac{\partial v}{\partial y} \right) \lambda + \frac{\partial u}{\partial x} \frac{\partial v}{\partial y} - \frac{\partial u}{\partial y} \frac{\partial v}{\partial x} = 0 \quad (\text{B.3})$$

$$\lambda = \frac{1}{2} \left(\frac{\partial u}{\partial x} + \frac{\partial v}{\partial y} \right) \pm \sqrt{\frac{1}{4} \left(\frac{\partial u}{\partial x} + \frac{\partial v}{\partial y} \right)^2 - \frac{\partial u}{\partial x} \frac{\partial v}{\partial y} + \frac{\partial u}{\partial y} \frac{\partial v}{\partial x}} \quad (\text{B.4})$$

Writing the eigenvalue as: $\lambda = \lambda_{cr} \pm i\lambda_{ci}$, yields:

$$\lambda_{ci} = \sqrt{-\frac{1}{4} \left(\frac{\partial u}{\partial x} + \frac{\partial v}{\partial y} \right)^2 + \frac{\partial u}{\partial x} \frac{\partial v}{\partial y} - \frac{\partial u}{\partial y} \frac{\partial v}{\partial x}} \quad (\text{B.5})$$

$$\lambda_{ci} = \sqrt{-\frac{1}{4} \left(\frac{\partial u^2}{\partial x} + \frac{\partial v^2}{\partial y} \right) + \frac{1}{2} \frac{\partial u}{\partial x} \frac{\partial v}{\partial y} - \frac{\partial u}{\partial y} \frac{\partial v}{\partial x}} \quad (\text{B.6})$$

To implement the swirling strength on the velocity field the velocity gradient terms are discretized according to a central difference scheme, see figure B.1.

$$\frac{\partial u}{\partial x} \approx \frac{u_{i+1,j} - u_{i-1,j}}{x_{i+1,j} - x_{i-1,j}} \quad (\text{B.7})$$

$$\frac{\partial u}{\partial y} \approx \frac{u_{i,j+1} - u_{i,j-1}}{y_{i,j+1} - y_{i,j-1}} \quad (\text{B.8})$$

$$\frac{\partial v}{\partial x} \approx \frac{v_{i+1,j} - v_{i-1,j}}{x_{i+1,j} - x_{i-1,j}} \quad (\text{B.9})$$

$$\frac{\partial v}{\partial y} \approx \frac{v_{i,j+1} - v_{i,j-1}}{y_{i,j+1} - y_{i,j-1}} \quad (\text{B.10})$$

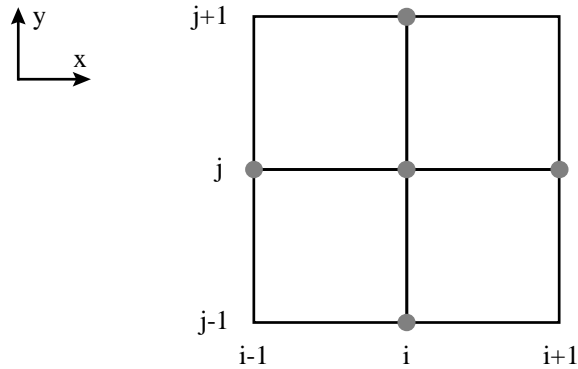


Figure B.1. The swirling strength and vorticity are calculated on location i,j from the velocity components on the other points, which are known from the PIV analysis

B.1 Circulation of a vortex

Circulation is related to vorticity via ^[17]:

$$\Gamma = -\iint \xi dS \quad (\text{B.11})$$

For the in-plane circulation the out-of-plane vorticity component is used, where:

$$\xi_z = \frac{\partial u}{\partial y} - \frac{\partial v}{\partial x} \quad (\text{B.12})$$

The vorticity is again discretized according to a central difference scheme (see figure B.1). For the calculation of the circulation of a vortex, an integral area around the vortex core is taken. This area is increased until the circulation reaches a peak value.

Appendix C

Swirling strength measurements

In appendix C the swirling strength of the flow field is shown for some of the relevant PIV measurements. The moment of the measurement within the flap cycle is depicted with the dimensionless time τ , where $0 < \tau < 0.5$ is the out-stroke and $0.5 < \tau < 1$ the in-stroke. The figures show leading edge vortices (LEV) and trailing edge vortices (TEV), generated during the out-stroke (1) and in-stroke (2). Velocity vectors and swirling directions are distracted from flow field images.

C.1 Improved wing at 9 Hz at $0.71R$

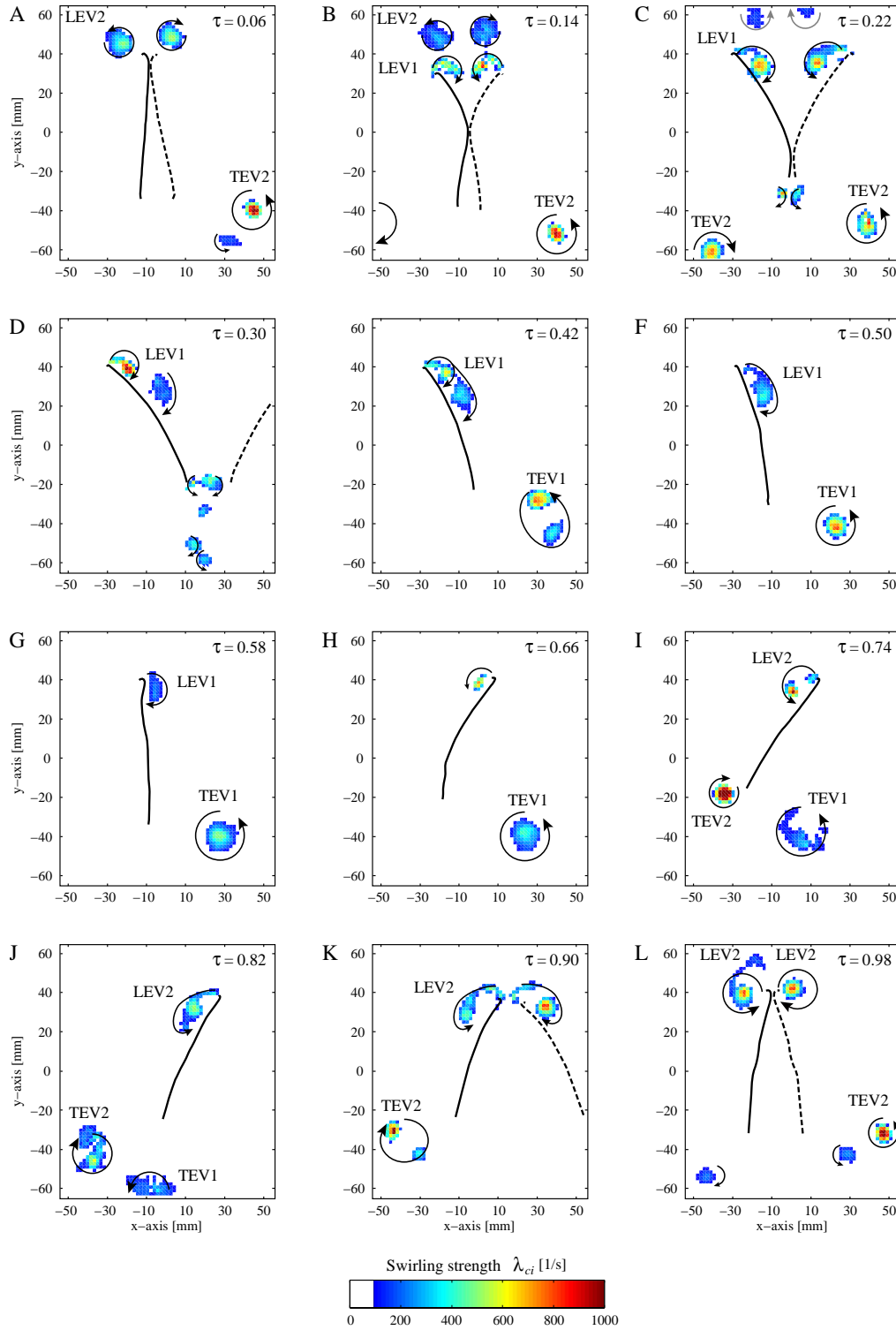


Figure C.1. Swirling strength at various moments during the flap cycle for the improved wing flapping at 9 Hz and at spanwise location $0.71R$

C.2 Improved wing at 11 Hz at 0.71R

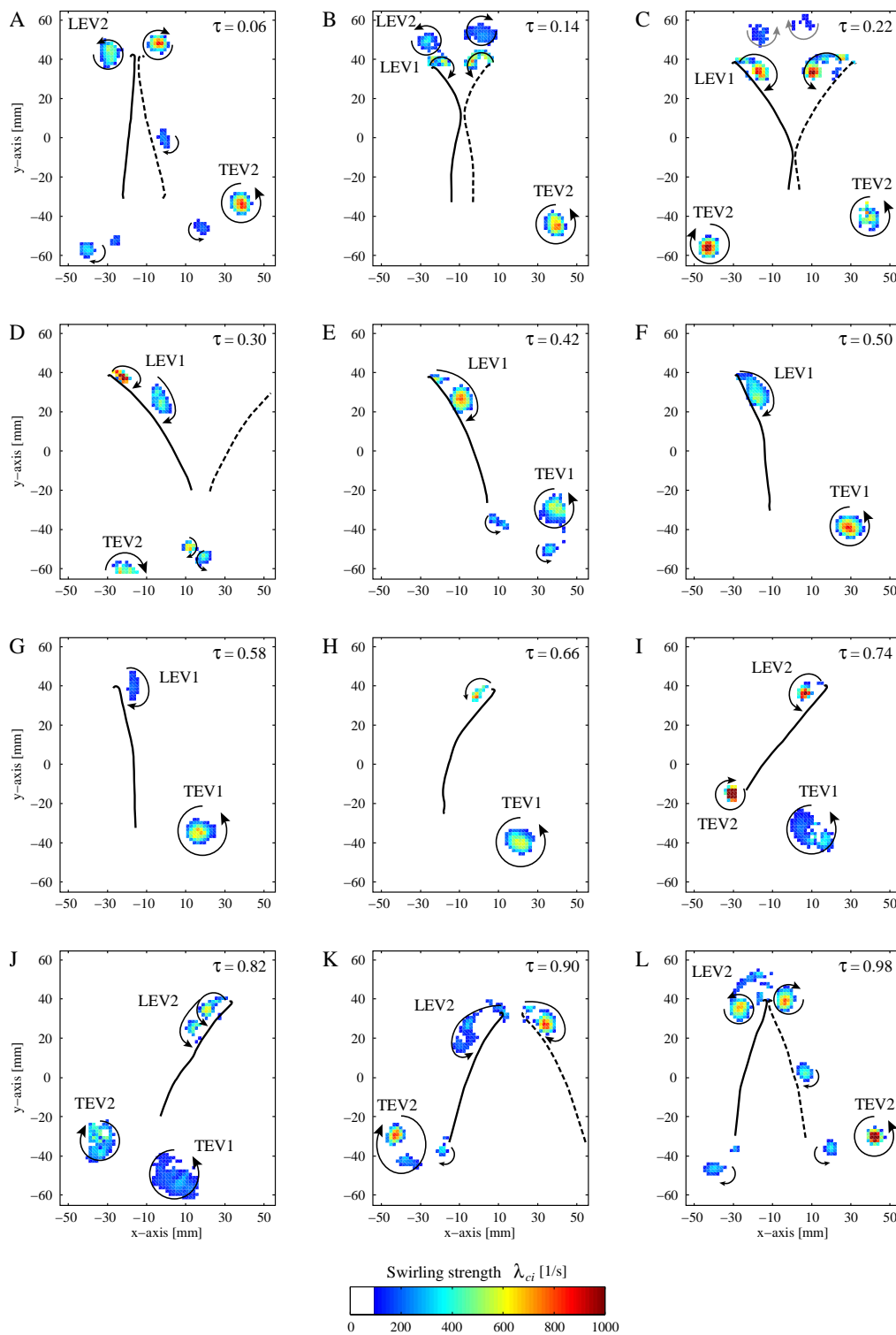


Figure C.2. Swirling strength at various moments during the flap cycle for the improved wing flapping at 11 Hz and at spanwise location 0.71R

C.3 Improved wing at 11 Hz at $0.86R$

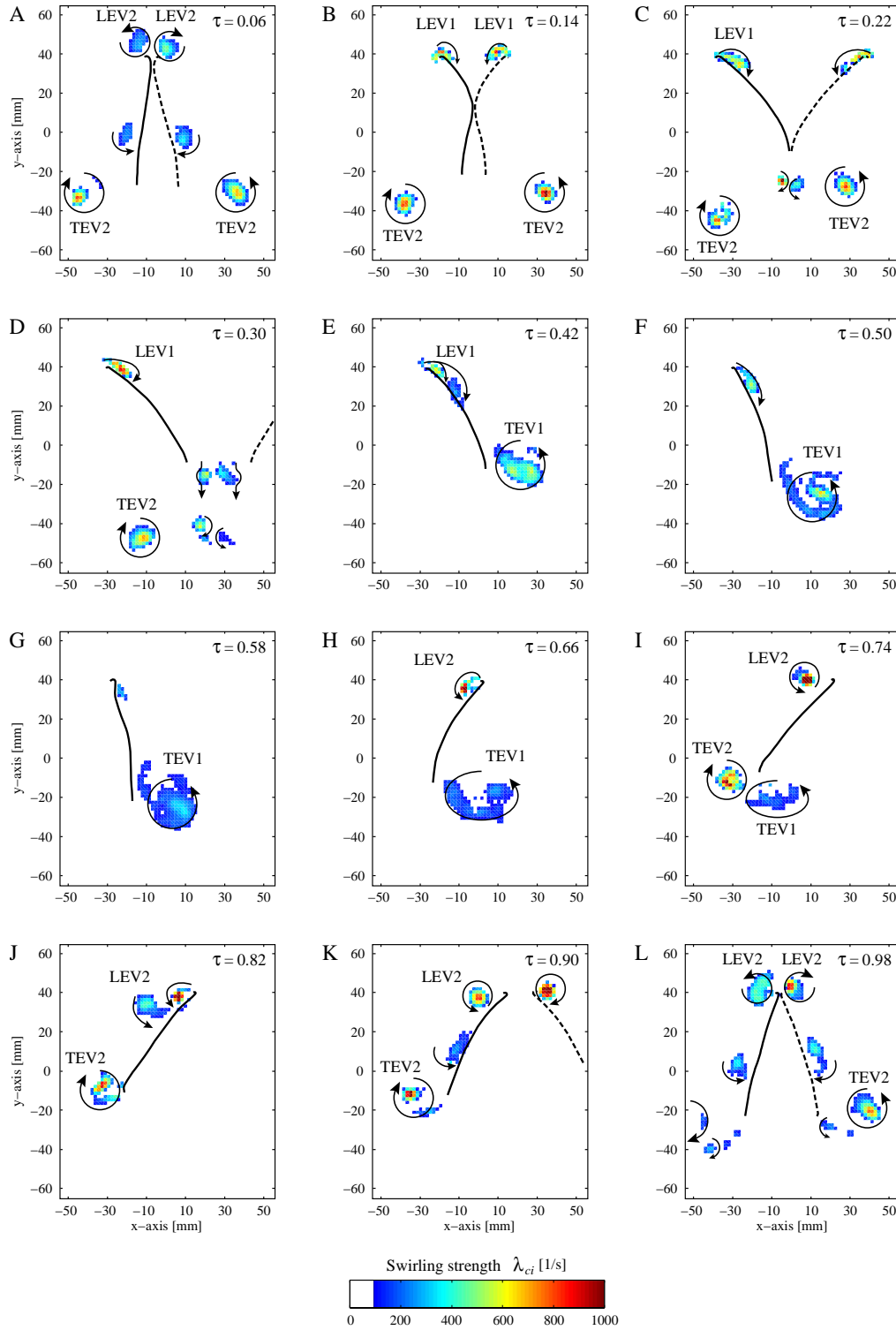


Figure C.3. Swirling strength at various moments during the flap cycle for the improved wing flapping at 11 Hz and at spanwise location $0.86R$

C.4 Improved wing at 13 Hz at $0.43R$

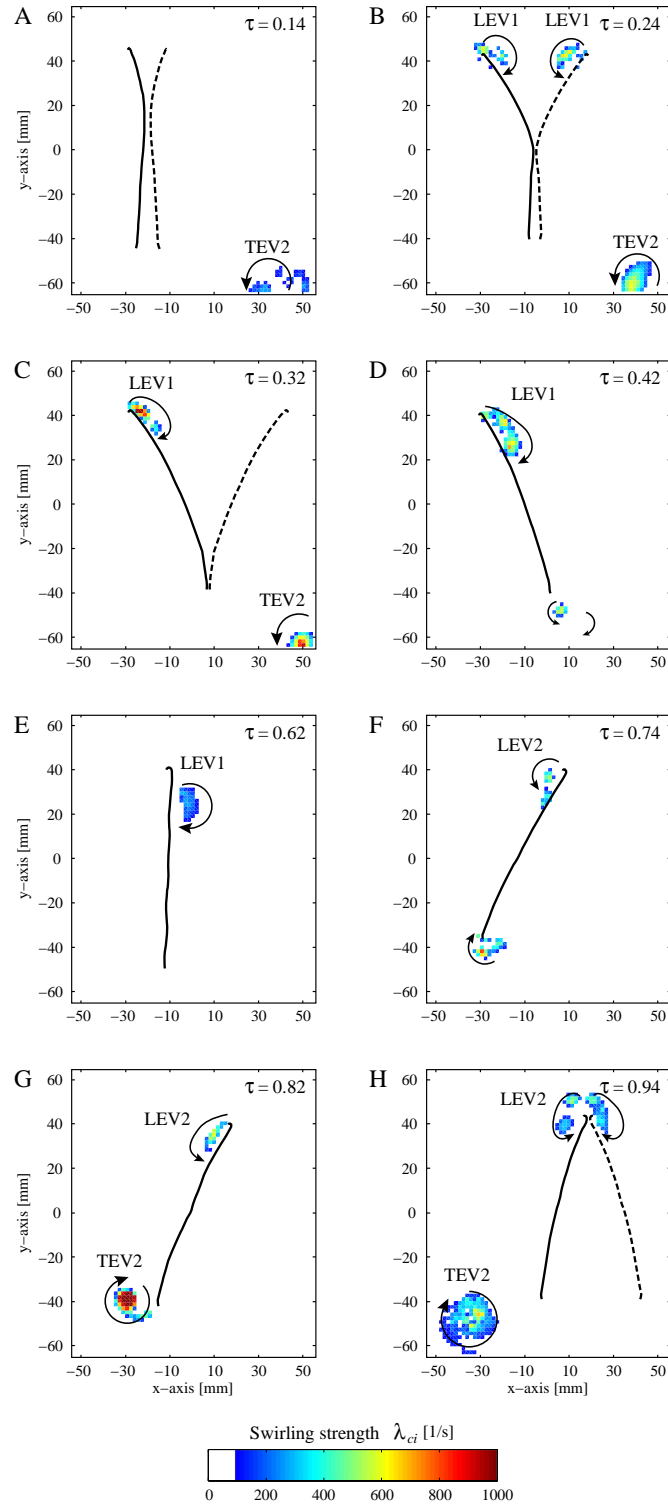


Figure C.4. Swirling strength at various moments during the flap cycle for the improved wing flapping at 13 Hz and at spanwise location $0.43R$

C.5 Improved wing at 13 Hz at $0.57R$

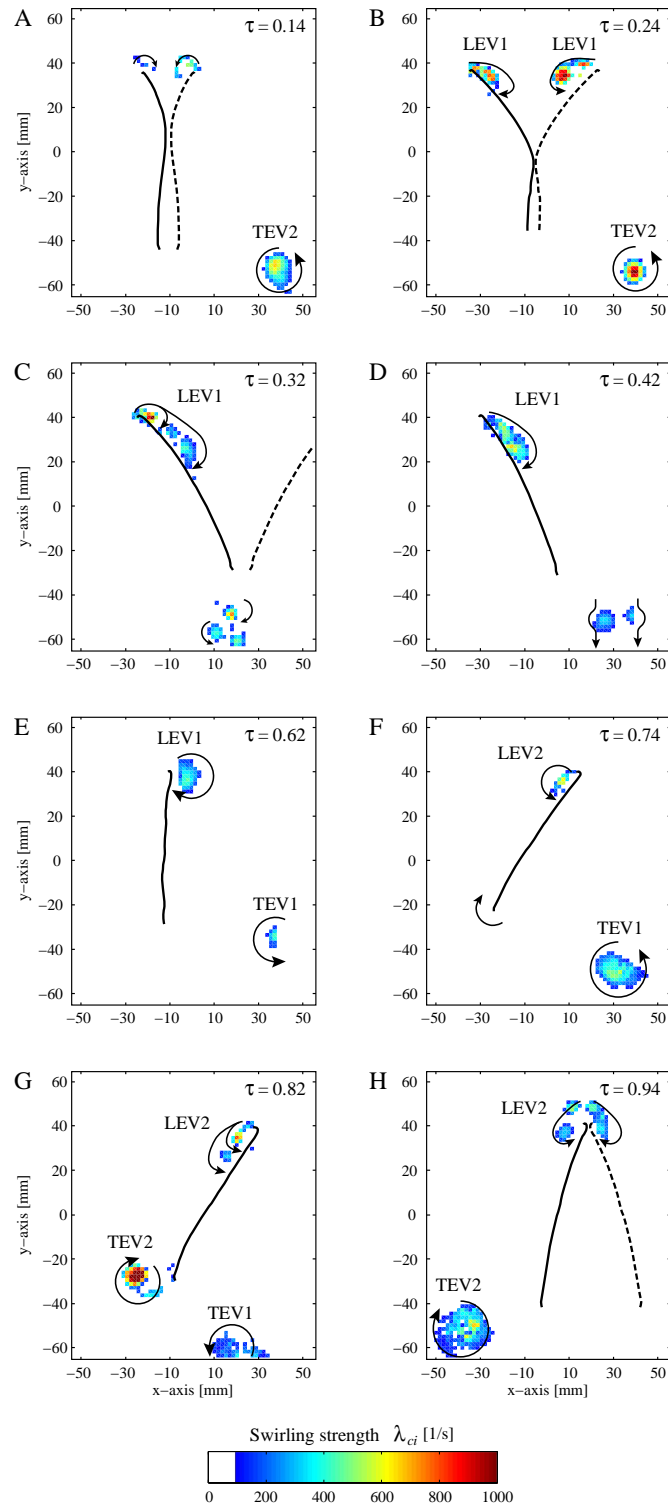


Figure C.5. Swirling strength at various moments during the flap cycle for the improved wing flapping at 13 Hz and at spanwise location $0.57R$

C.6 Improved wing at 13 Hz at $0.71R$

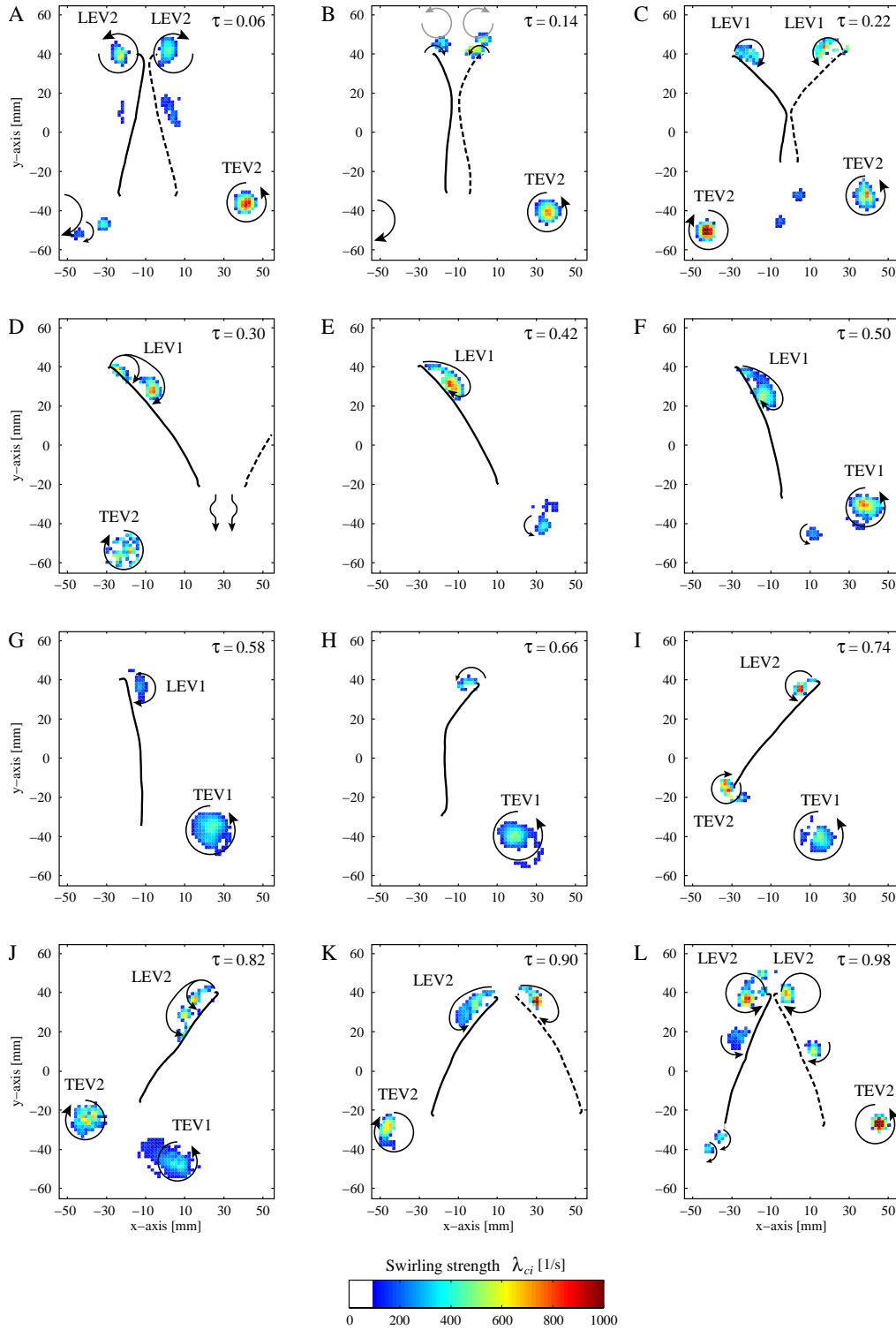


Figure C.6. Swirling strength at various moments during the flap cycle for the improved wing flapping at 13 Hz and at spanwise location $0.71R$

C.7 Improved wing at 13 Hz at $0.86R$

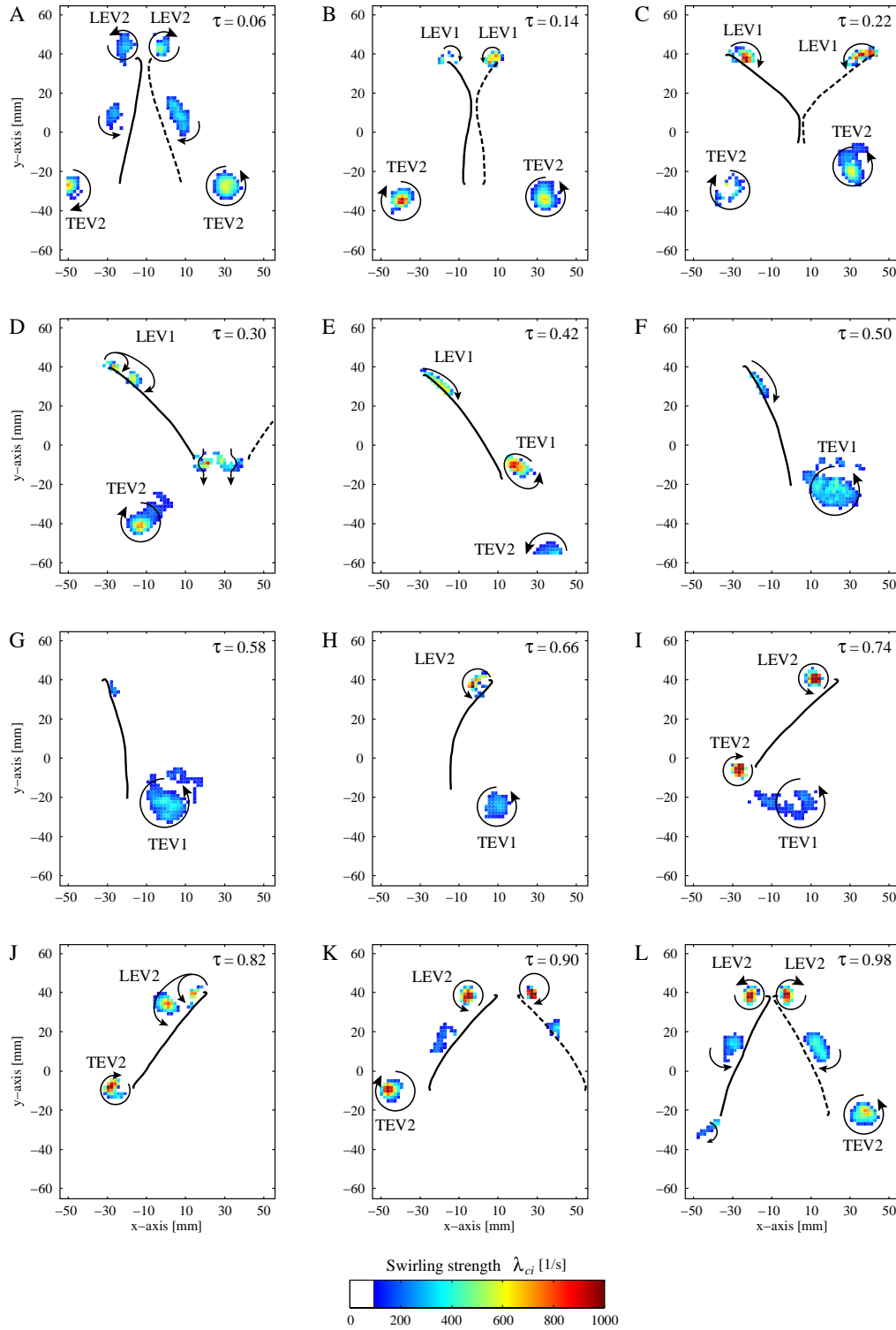


Figure C.7. Swirling strength at various moments during the flap cycle for the improved wing flapping at 13 Hz and at spanwise location $0.86R$

C.8 Original wing at 11 Hz at $0.86R$

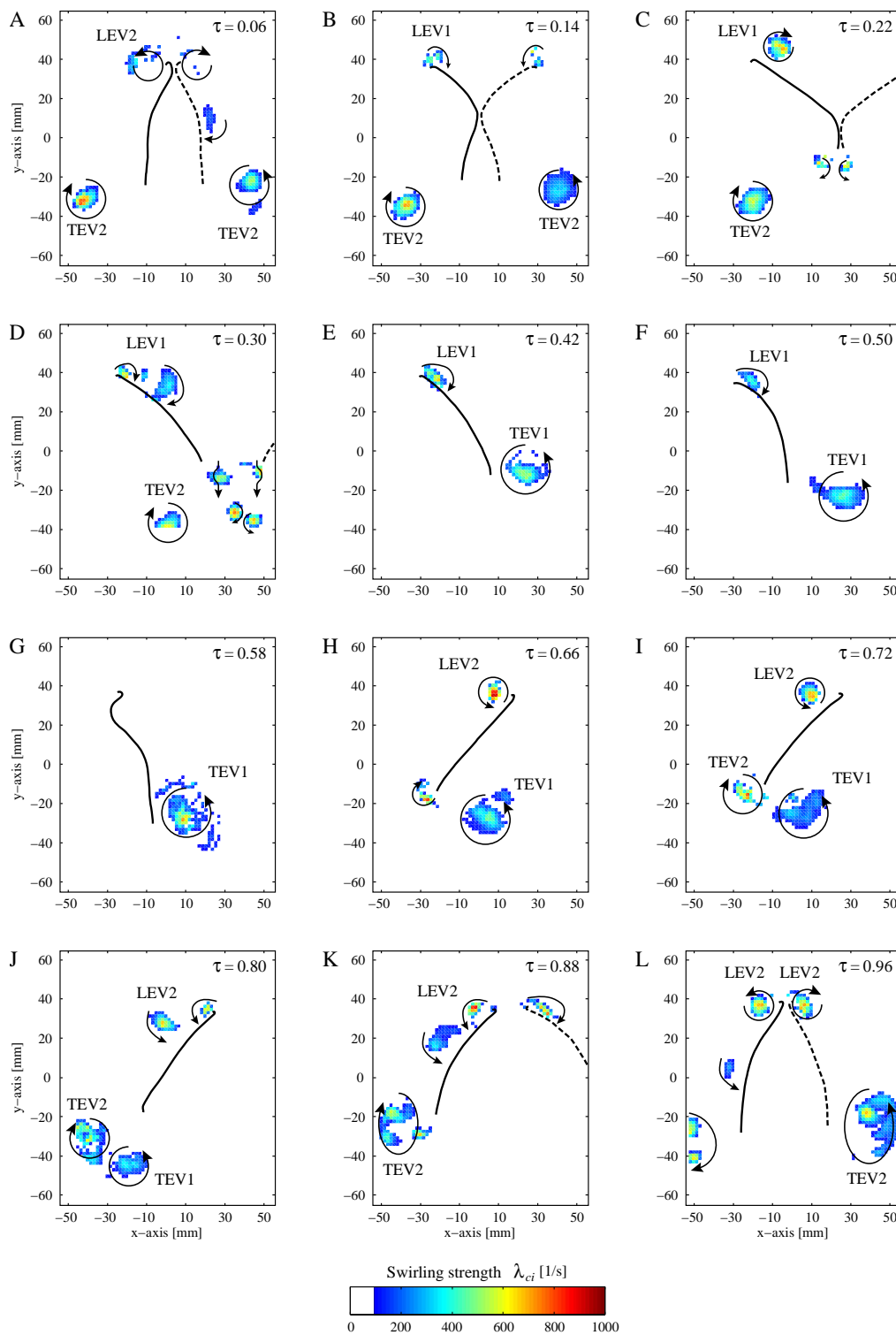


Figure C.8. Swirling strength at various moments during the flap cycle for the original wing flapping at 11 Hz and at spanwise location $0.86R$

C.9 High aspect ratio wing at 11 Hz at $0.71R$

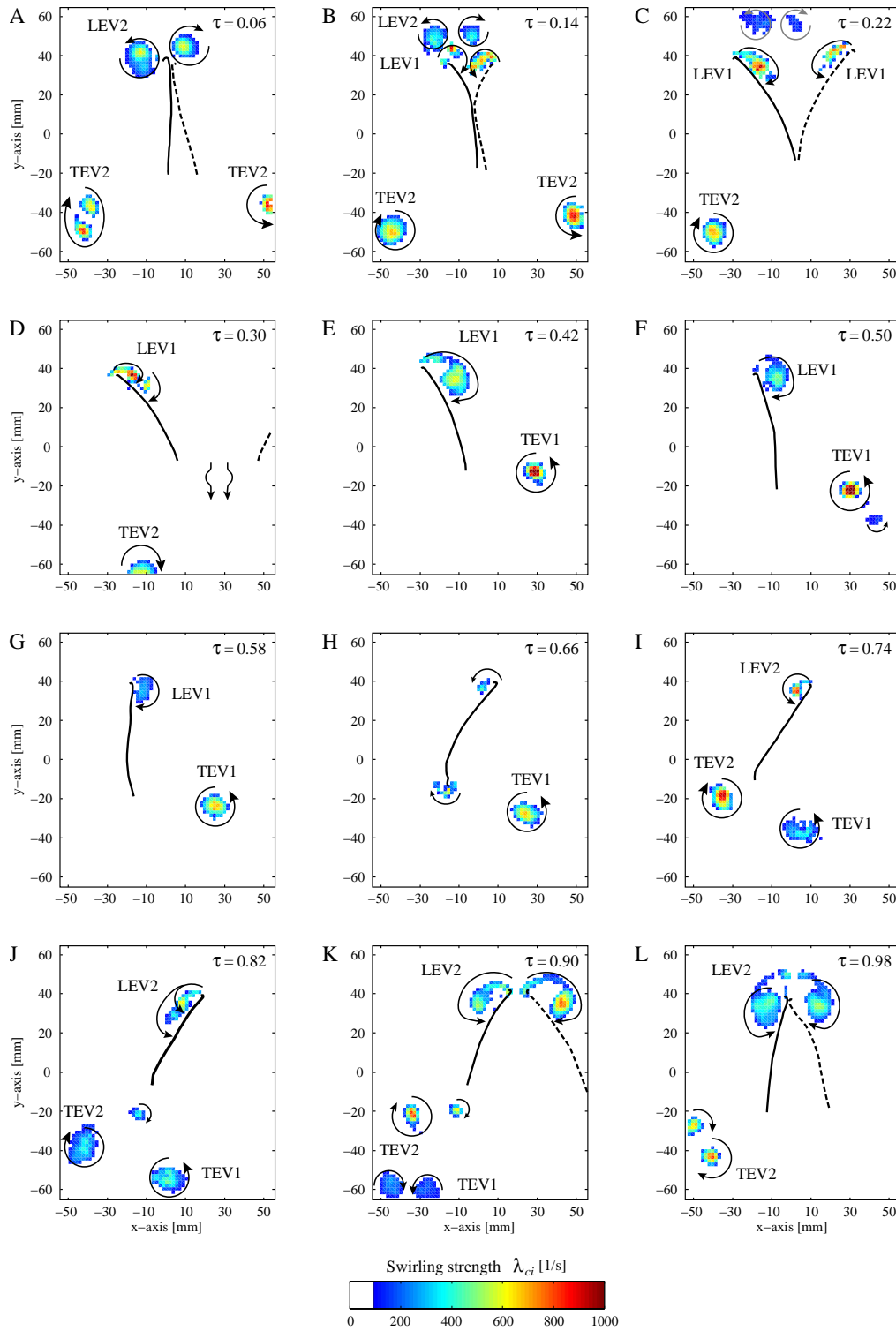


Figure C.9. Swirling strength at various moments during the flap cycle for the high aspect ratio wing flapping at 11 Hz and at spanwise location $0.71R$

C.10 High aspect ratio wing at 13 Hz at $0.71R$

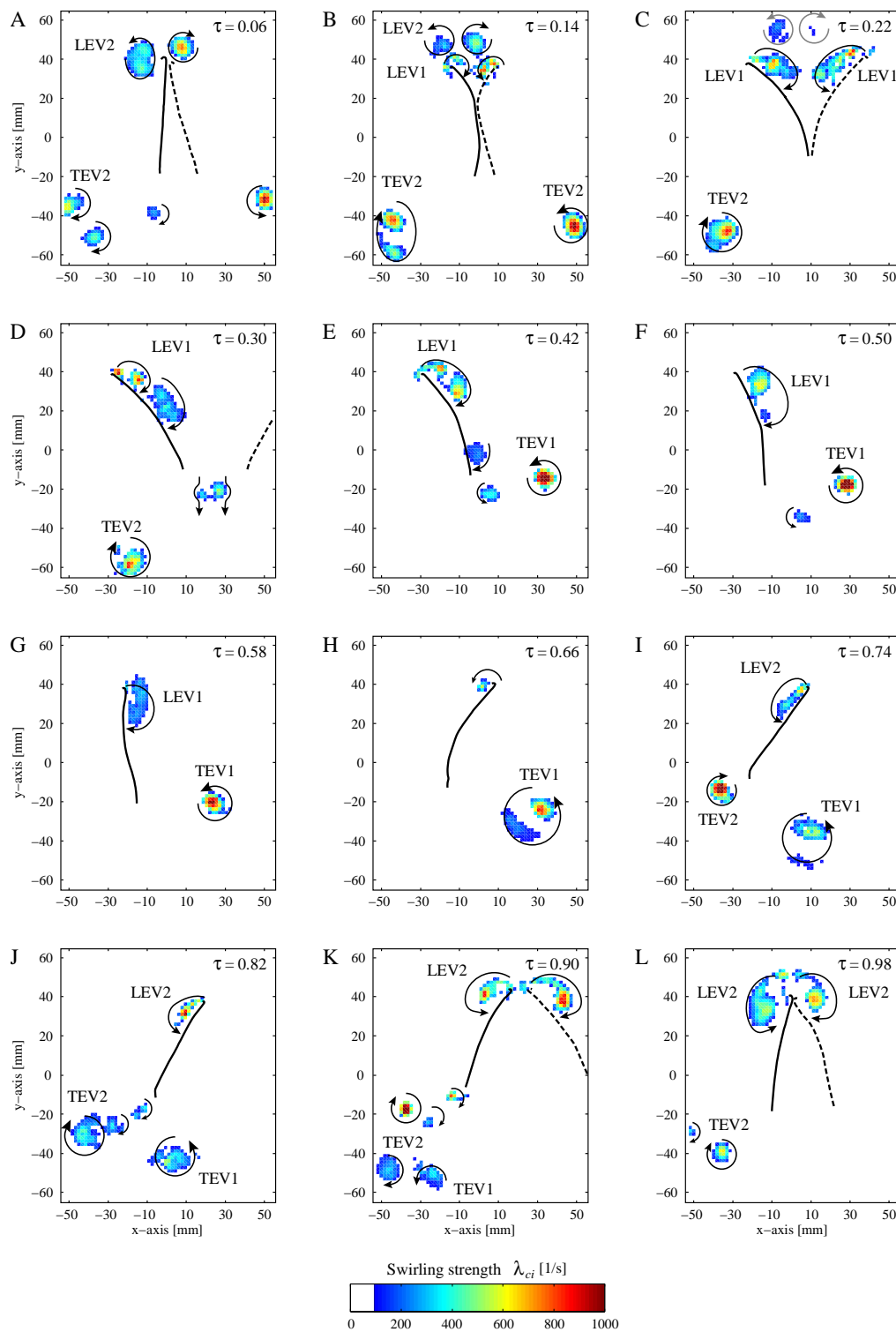


Figure C.10. Swirling strength at various moments during the flap cycle for the high aspect ratio wing flapping at 13 Hz and at spanwise location $0.71R$

